Title

Mapping spatial organization and genetic cell-state regulators to target immune evasion in ovarian cancer

Journal

Nature Immunology, 25(10)

ISSN

1529-2908

Authors

Yeh, Christine Yiwen
Aguirre, Karmen
Laveroni, Olivia
et al.

Publication Date

2024-10-01

DOI

10.1038/s41590-024-01943-5

Peer reviewed

nature immunology

Resource

https://doi.org/10.1038/s41590-024-01943-5

Mapping spatial organization and genetic cell-state regulators to target immune evasion in ovarian cancer

Received: 4 October 2023

Accepted: 25 July 2024

Published online: 23 August 2024

Check for updates

Christine Yiwen Yeh[1,2,3,10], Karmen Aguirre[1,4,5,10], Olivia Laveroni[1,10], Subin Kim[1], Aihui Wang[6], Brooke Liang[6], Xiaoming Zhang[6], Lucy M. Han[7], Raeline Valbuena[1], Michael C. Bassik[1], Young-Min Kim[1], Sylvia K. Plevritis[2,8], Michael P. Snyder[1], Brooke E. Howitt[6] ✉ & Livnat Jerby[1,5,9] ✉

The drivers of immune evasion are not entirely clear, limiting the success of cancer immunotherapies. Here we applied single-cell spatial and perturbational transcriptomics to delineate immune evasion in high-grade serous tubo-ovarian cancer. To this end, we first mapped the spatial organization of high-grade serous tubo-ovarian cancer by profiling more than 2.5 million cells in situ in 130 tumors from 94 patients. This revealed a malignant cell state that reflects tumor genetics and is predictive of T cell and natural killer cell infiltration levels and response to immune checkpoint blockade. We then performed Perturb-seq screens and identified genetic perturbations—including knockout of *PTPN1* and *ACTR8*—that trigger this malignant cell state. Finally, we show that these perturbations, as well as a PTPN1/PTPN2 inhibitor, sensitize ovarian cancer cells to T cell and natural killer cell cytotoxicity, as predicted. This study thus identifies ways to study and target immune evasion by linking genetic variation, cell-state regulators and spatial biology.

Multicellular dysregulation has an important function in the initiation and progression of a wide range of diseases, including cancer, where tumor development and accompanying immune responses depend on (and shape) the location of different cell-type populations, tissue properties and organization[1–3]. Cellular and animal models have been instrumental in identifying central immune suppressors[4–6] and have resulted in major breakthroughs in cancer treatment. However, many patients with cancer do not respond to current immunotherapies[7–9], resulting, at least in part, from two central gaps. First, in contrast to the study of cancer genetics, in which genome sequencing of tumors across large and diverse patient populations has provided a foundation to study the genetic basis of cancer and develop targeted therapies, we still lack equivalent maps for tumor tissue organization to study the inherently spatial processes of multicellular dynamics and immune exclusion in patients. Second, identifying the regulators of cell states and reciprocal intercellular interactions poses additional challenges and requires functional interrogation across a larger search space of combinatorial gene–environment perturbations.

In tubo-ovarian high-grade serous carcinoma (HGSC)—the most common and aggressive form of ovarian cancer[10]—these gaps are

[1]Department of Genetics, Stanford University School of Medicine, Stanford, CA, USA. [2]Department of Biomedical Data Science, Stanford University School of Medicine, Stanford, CA, USA. [3]Department of Medicine, Stanford University School of Medicine, Stanford, CA, USA. [4]Cancer Biology Program, Stanford University, Stanford, CA, USA. [5]Stanford Cancer Institute, Stanford University School of Medicine, Stanford, CA, USA. [6]Department of Pathology, Stanford University School of Medicine, Stanford, CA, USA. [7]Department of Pathology, California Pacific Medical Center, San Francisco, CA, USA. [8]Department of Radiology, Stanford University School of Medicine, Stanford, CA, USA. [9]Chan Zuckerberg Biohub, San Francisco, CA, USA. [10]These authors contributed equally: Christine Yiwen Yeh, Karmen Aguirre, Olivia Laveroni. ✉e-mail: bhowitt@stanford.edu; ljerby@stanford.edu

pronounced. HGSC is often diagnosed at advanced stages, and is prone to chemoresistance, resulting in a 5-year survival rate below 50%[10]. HGSC genetics has been thoroughly characterized[11–14], demonstrating nearly ubiquitous *TP53* mutations and massive copy number alterations (CNAs), with some tumors also presenting with *BRCA1/BRCA2* mutations and homologous recombination deficiency. Abundant tumor-infiltrating lymphocytes (TILs) are a robust prognostic marker of positive clinical outcomes in patients with HGSC[15,16]. Yet, while single-cell studies have provided important resources and insight into HGSC cell biology[17,18], the molecular and cellular modalities that promote or suppress immune recruitment and infiltration in HGSC are unclear, and existing immunotherapies continue to have limited success in treating HGSC[19,20].

Here, we provide a molecular map of HGSC spatial organization, that, in conjunction with data-driven experimental design and high-content CRISPR screens, enabled us to systematically uncover molecular and cellular regulators of HGSC tumor immunity, as well as genetic and pharmacological perturbations that affect it.

Results

Single-cell spatial transcriptomic mapping of HGSC

To spatially map HGSC in the setting of metastatic disease, we applied in situ imaging with high-plex RNA detection at single-cell resolution to 130 HGSC tumors from a total of 94 patients to generate 202 tissue profiles, yielding a total of 2,598,277 high-quality single-cell spatial transcriptomes (Fig. 1a and Supplementary Table 1a,b). Tumor tissues were obtained from the adnexa (ovaries/fallopian tube, $n = 84$), and/or omentum ($n = 46$), with 36 patient-matched pairs of adnexal and omental tumors. All tumor tissue profiles were obtained from debulking surgeries in either the treatment-naive or the neoadjuvant chemotherapy-treated setting (Fig. 1b and Supplementary Table 2a,b). Associated patient clinical data including treatment history (for example, PARP inhibitor, bevacizumab and immune checkpoint blockade (ICB)) and survival outcomes are also available (Fig. 1a,b, Supplementary Table 2a,b and Methods). Eight patients in this cohort received ICB treatment, but in all cases ICB treatment was after sample collection. For 40 patients, we also obtained DNA sequencing data spanning a 648-gene panel (Fig. 1b, Supplementary Table 1b and Methods), focused on actionable single-nucleotide variations, somatic CNAs, chromosomal rearrangements and tumor mutational burden (TMB), providing a basis to link tissue structure and somatic genetic aberrations.

The spatial data were collected using three spatial transcriptomics (ST) platforms, allowing rigorous cross-platform validation of these recently developed technologies (Fig. 1a, Supplementary Fig. 1a–c and Supplementary Table 1b). All three ST platforms used here provide detection of RNA molecules at subcellular resolution. As the spatial molecular imaging (SMI, also known as CosMx)[21] platform had the largest gene panels, we used SMI to generate most of the data in this study. Data were generated with the SMI platform in two rounds (Discovery and Test; Fig. 1a). In the first round, we applied SMI to formalin-fixed and paraffin-embedded (FFPE) tissue microarrays (TMAs) to generate a Discovery dataset that spans 960 genes measured across 491,792 cells from 94 tumors. The discovery phase of the study was performed exclusively based on analyses of the Discovery dataset; all the spatiomolecular transcriptional programs identified in this study were derived from this dataset. In the second round, we applied SMI to another TMA from 34 additional (unseen) patients as well 4 whole-tissue sections (from patients included in the Discovery set), spanning 6,175 and 1,000 genes (Supplementary Table 1b and Supplementary Fig. 1a), respectively, and a total number of 1,233,033 cells. The Test datasets were used only in the testing phase of the study to test if the key spatiomolecular findings generalize to unseen patients and larger fields of view (FOVs) within a tumor. For technical comparison and validation, in situ sequencing (ISS; via Xenium[22]) was applied to profile 280 genes in an FFPE TMA of 32 tissue cores, and MERFISH[23] (multiplexed error-robust fluorescence in situ hybridization (ISH)) was applied to profile 140 genes in four fresh-frozen tissue sections (Methods and Supplementary Table 1b).

For robust data processing, we developed an analytical procedure that mitigates segmentation inaccuracies (Extended Data Fig. 1a–f and Methods) and results in robust cell-type annotation through recursive clustering of the spatial single-cell gene expression profiles (Extended Data Fig. 2a,b and Methods). Applying our pipeline to the Discovery dataset identified malignant cells ($n = 314,191$), T cells and natural killer (NK) cells ($n = 28,676$), B cells ($n = 16,373$), monocytes ($n = 45,549$), mast cells ($n = 606$), fibroblasts/stromal cells ($n = 72,861$) and endothelial cells ($n = 13,536$; Fig. 1c,d and Extended Data Fig. 2a,b). The same procedure resulted in similar annotations of the Validation and Test datasets (Fig. 1c,d). T/NK cells were then further stratified to NK ($n = 6,897$), $CD4^+$ T ($n = 6,040$), $CD8^+$ T ($n = 8,439$) and regulatory T cells (T_{reg} cells; $n = 1,905$) in the Discovery dataset (Extended Data Fig. 2c–g and Methods), with similar T/NK stratification results obtained in the Test and Validation 1 datasets (Extended Data Fig. 2h,i and Methods).

Cell-type annotations were validated in five ways. First, de novo cell-type signatures identified based on the annotated cells recapitulate well known cell-type markers (Methods, Supplementary Table 3a,b and Extended Data Fig. 2a). Second, cell-type annotations are aligned with matching hematoxylin and eosin (H&E) and immunohistochemical markers (Extended Data Fig. 3a–d). Third, cell-type annotations were aligned both spatially (Extended Data Fig. 3e) and compositionally (Extended Data Fig. 3f) when examining biological and technical replicate-matched tissue samples profiled in the Discovery and Validation 1 datasets. Fourth, we generated a unified HGSC single-cell transcriptomic atlas by integrating the HGSC spatial data with six publicly available single-cell RNA-sequencing (scRNA-seq) datasets[17,24–29] (Fig. 1e,f and Supplementary Fig. 2a–c). The unified co-embedding corroborates the cell-type annotations obtained independently based on the ST data alone (Fig. 1e, Supplementary Fig. 2a,b and Methods). Fifth, using patient-matched CNA data, we examined for each gene in each cell type whether its expression is significantly associated with its copy number in the tumor (Benjamini–Hochberg false discovery rate (BH FDR) < 0.05, linear mixed-effects model (LMM); Methods). In malignant cells, gene expression is patient specific and the expression of 42% of

Fig. 1 | Single-cell ST mapping of HGSC. a, Cohort and data overview. Created with BioRender.com. **b**, Summary of clinical history, tumor genetics and ST profiles per patient. Each column represents 1 of 94 patients. NACT, neoadjuvant chemotherapy; Beva, bevacizumab; PARPi, PARP inhibitor. **c**, Uniform manifold approximation and projection (UMAP) embedding of high-confidence spatial single-cell transcriptomes from the different datasets. *n* denotes number of cells within each cell-type annotation in the Discovery dataset. **d**, Representative tumor tissue ST images (11 of 202) with cells plotted in situ and colored based on cell-type annotations. **e**, Co-embedding of spatial single-cell transcriptomes from this study with six publicly available HGSC scRNA-seq datasets[17,24–29]. **f**, Cell-type composition (*y* axis) per tissue profile (*x* axis) from this study and in six publicly available scRNA-seq HGSC datasets[17,24–29]. **g**, Pairwise colocalization analysis: the number of tissue profiles (*x* axis) where each pair of cell types (*y* axis) shows significantly (BH FDR < 0.05, hypergeometric test) higher (red), lower (blue) or expected (gray) colocalization frequencies compared to those expected by random. **h**, $\log_2$ colocalization quotient (CLQ) of T/NK cells with fibroblasts ($CLQ_{T/NK\ cell \to fibroblast}$, blue) and T/NK cells with malignant cells ($CLQ_{T/NK\ cell \to malignant}$, green, *x* axis) in ST tissue profiles from the Discovery dataset ($n = 87$ CLQ pairs, $P = 4.31 \times 10^{-10}$, paired Wilcoxon rank-sum test). Light gray lines connect paired values in each ST tissue core (black dots). In the box plots, the middle line denotes the median, box edges indicate the 25th and 75th percentiles, and whiskers extend to the most extreme points that do not exceed ±1.5 times the interquartile range (IQR); further outliers (minima and maxima) are marked individually as black points beyond the whiskers; $^{****}P < 1 \times 10^{-4}$, paired Wilcoxon rank-sum test. NS, not significant.

https://doi.org/10.1038/s41590-024-01943-5

the genes matches their CNAs (that is, 'in *cis*'), compared to only 0–2% in the nonmalignant cell types (Supplementary Fig. 4a). The genes that do not show in *cis* RNA-to-CNA associations in malignant cells are significantly more copy number stable (median = 2, range = 0–7) compared to those showing the association (median = 3, range = 0–20, $P = 5.04 \times 10^{-10}$, one-sided Wilcoxon rank-sum test). In contrast to CNAs, a relatively small number of genes (0–4%) are associated with clinical and other genetic covariates in malignant and nonmalignant cell types (that is, age at diagnosis, disease stage, pathogenic *BRCA1/BRCA2* mutational status and TMB; Supplementary Fig. 4a).

Initial analyses of the data reveal heterogeneous tumor tissue compositions across patients (Fig. 1f), yet a generalizable spatial organization at the macro level, where malignant cells and fibroblasts form spatially distinct compartments (which we refer to as the malignant and

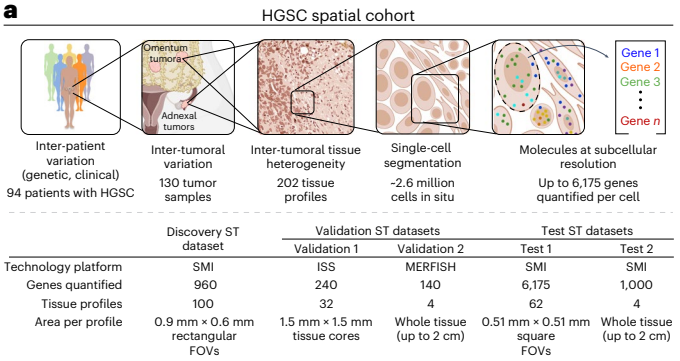

	Discovery ST dataset	Validation ST datasets		Test ST datasets	
		Validation 1	Validation 2	Test 1	Test 2
Technology platform	SMI	ISS	MERFISH	SMI	SMI
Genes quantified	960	240	140	6,175	1,000
Tissue profiles	100	32	4	62	4
Area per profile	0.9 mm × 0.6 mm rectangular FOVs	1.5 mm × 1.5 mm tissue cores	Whole tissue (up to 2 cm)	0.51 mm × 0.51 mm square FOVs	Whole tissue (up to 2 cm)

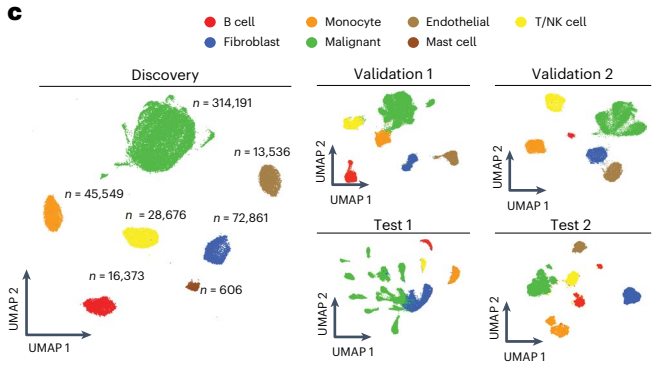

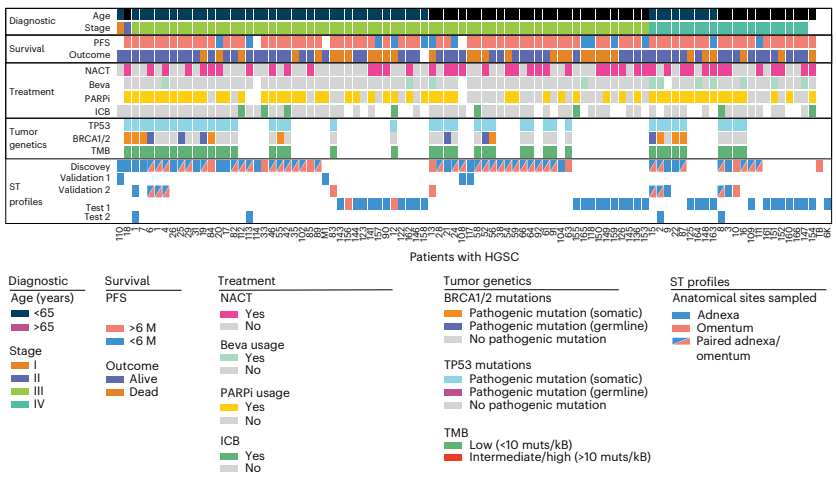

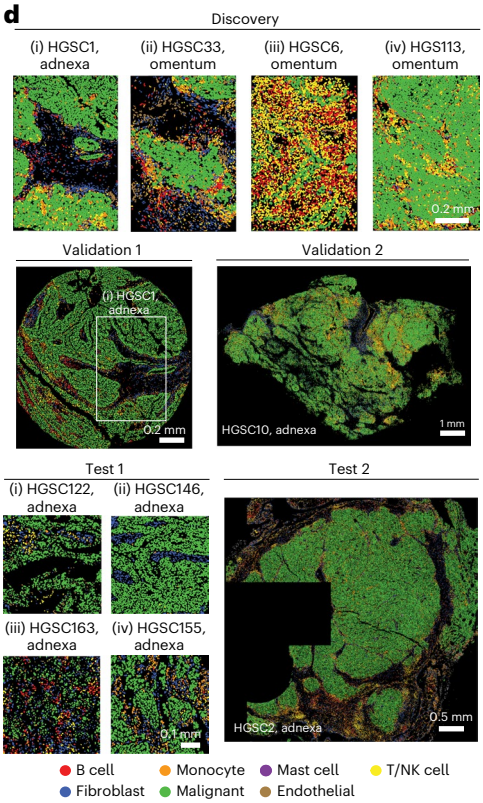

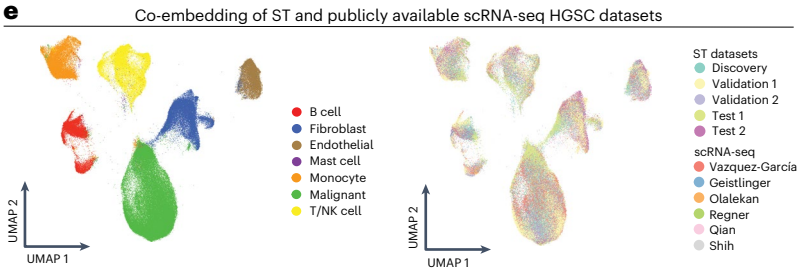

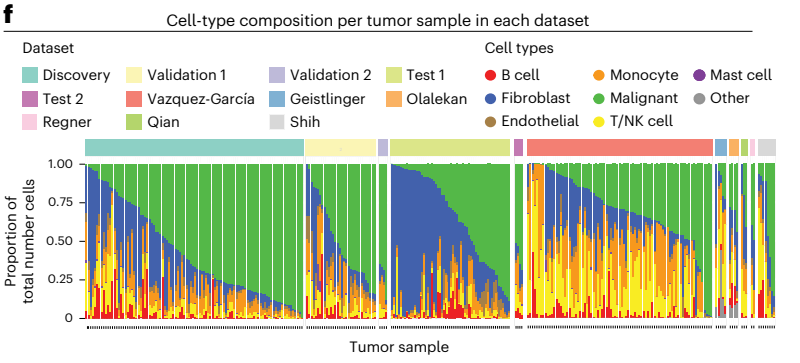

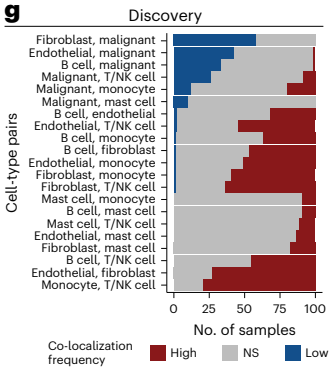

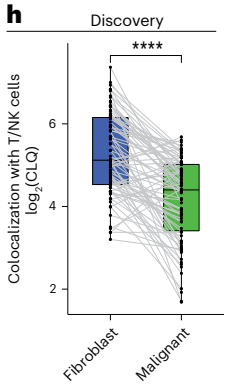

stromal compartments; Fig. 1g and Supplementary Fig. 3a,b), such that T/NK cells preferentially localized in the stromal rather than the malignant compartment ($P < 1 \times 10^{-4}$, paired Wilcoxon rank-sum test; Fig. 1h, Supplementary Fig. 3c–g and Methods). This macro-organization principle was first observed in the Discovery dataset (Fig. 1g,h and Supplementary Fig. 3c) and subsequently validated in the Validation and Test datasets (Supplementary Fig. 3a,b,d–g).

Patients with higher T/NK cell abundance had improved clinical outcomes ($P = 2.03 \times 10^{-2}$, univariate Cox regression, $P = 2.1 \times 10^{-4}$, log-rank test), demonstrating that even a relatively small area within the tumor (Supplementary Fig. 1a) is predictive of patient outcomes 5 years and even 8 years later.

T cell states reflect T cell tumor infiltration status

Using the Discovery dataset, we set out to map the immune cell-intrinsic and cell-extrinsic factors that mark immune infiltration and exclusion. First, taking an unbiased data-driven approach, we used unsupervised methods to embed and cluster the transcriptomes of cells from each immune cell type without any spatial information. The resulting embedding and clustering shows that immune cells residing in the malignant compartment are transcriptionally distinct from those that reside outside of it (Fig. 2a). Next, we took a spatially supervised approach and identified for each of the five immune cell subtypes robustly represented in the data a tumor infiltration program (TIP), consisting of genes that are significantly (BH FDR < 0.05, LMM; Methods) overexpressed or underexpressed in the pertaining immune cell subtype as a function of proximity to malignant cells (Fig. 2b,c, Extended Data Fig. 4a and Supplementary Table 4a).

$CD8^+$ T cell TIP (CD8 TIP) demonstrates that effector and exhausted $CD8^+$ T cells more frequently colocalize with malignant cells ($P = 3.24 \times 10^{-53}$, LMM; Fig. 2b,c), as also confirmed by annotating $CD8^+$ T cells based on predefined signatures[30] (Fig. 2d and Extended Data Fig. 4b–e). CD8 TIP upregulated genes include effector cytotoxicity genes as granzymes (*GZMA*, *GZMB* and *GZMH*) and perforin (*PRF1*), chemokines (*CCL3*, *CCL4*, *CCL4L2* and *CCL5*), interferon gamma (IFN-γ; encoded by *IFNG*), interferon signaling genes (for example, *IFITM1*, *IFNG*, *JAK1* and *STAT1*) and immune checkpoints (*CTLA4*, *HAVCR2*, *PDCD1*, *TIGIT* and *LAG3*), as well as *KLRB1* (that is, *CD161*) and *CXCR6*, which have been previously reported to suppress[31] or sustain[32–34] the cytotoxic function of exhausted $CD8^+$ T cells, respectively. CD8 TIP downregulated genes include naive and memory T cell markers (*SELL*, *IL7R* and *CD44*), the co-stimulatory gene *CD28*, the granzyme encoded by *GZMK* and the chemokine receptor encoded by *CXCR4* (Fig. 2b). Extending CD8 TIP to the whole-transcriptome level based on scRNA-seq data[17] (Methods and Supplementary Table 4b,c) revealed the upregulation of other exhaustion-associated genes[30,35] (that is, *ENTPD1*, *BST2*, *CD63*, *MIR155HG*, *MYO7A* and *NDFIP2*), and downregulation of additional naive T cell markers (for example, *CCR7*, *TCF7*, *SATB1* and *KLF2*), with *MALAT1*, *KLF2*, *CCR7*, *GPR183* and *TCF7* being the topmost downregulated genes in the extended CD8 TIP ($P < 1 \times 10^{-16}$, $r_s > 0.23$, Spearman correlation).

Testing these findings in the Test datasets, the CD8 TIP identified in the Discovery dataset was validated as an infiltration marker both in unseen patients and in whole-tissue sections ($P = 4.22 \times 10^{-3}$ and $P < 1 \times 10^{-17}$, LMM, Test datasets 1 and 2, respectively; Extended Data Fig. 4f,g), and exhausted and effector $CD8^+$ T cell subsets were enriched in proximity to malignant cells ($P = 1.09 \times 10^{-5}$ and $P < 1 \times 10^{-17}$, hypergeometric tests, for Test datasets 1 and 2, respectively; Extended Data Fig. 4h).

CD8 TIP is not associated with age at diagnosis, disease stage (III or IV), pathogenic *BRCA1/BRCA2* mutations, or TMB, but does show lower expression levels in samples after neoadjuvant treatment ($P < 4.42 \times 10^{-3}$, LMM, also when controlling for malignant cell abundance).

To investigate the role of the stroma in preferentially colocalizing with naive and memory T cells compared to effector and exhausted T cells, we integrated the ST data with sample-matched H&E stains independently annotated by a gynecologic pathologist (Supplementary Fig. 5a–e), revealing two fibroblast subsets, one marking normal stroma and the other marking desmoplasia (that is, a neoplasia-associated alteration in fibroblasts and extracellular matrix with distinct tissue morphology[36–40]; Fig. 2e,f, Supplementary Fig. 5a–g and Supplementary Table 5a). As expected[41,42], desmoplastic fibroblasts not only overexpress collagen fibril organization and extracellular matrix genes ($P < 1 \times 10^{-2}$, permutation test; Supplementary Fig. 5b and Supplementary Table 5b), but also upregulate *CXCL12* (the cognate ligand of *CXCR4*; Fig. 2e) and were associated with niches enriched with T/NK cells ($P < 1 \times 10^{-4}$, LMM).

To link these findings to paracrine signaling, we compiled 2,678 ligand–receptor pairs based on three public resources[43–45] (Supplementary Table 5c and Methods). Focusing on $CD8^+$ T cells, we identified 24 ligand–receptor pairs that mark the interactions of $CD8^+$ T cells with other cells in the malignant or stromal compartment (Methods). The resulting network (Fig. 2g and Supplementary Table 5d) manifests suppressive ligand–receptor interactions in the malignant compartment (for example, CD80/CD86–CTLA4, $CD8^+$ T cell–monocyte; TIM3–LAGLS9, $CD8^+$ T cell–malignant cell) and $CD8^+$ T cell-mediated chemoattraction of other immune cells via *CCL2* and *CCL5*. Colocalization of *CXCR6–CXCL16* ($CD8^+$ T cell–malignant cell) and *CXCR4–CXCL12* ($CD8^+$ T cell–fibroblasts) mark chemoattraction of infiltrating and stroma-residing $CD8^+$ T cells, respectively (Fig. 2g; BH FDR $< 1 \times 10^{-10}$, LMM; Supplementary Fig. 5j–l). Of note, TCF1 (encoded by *TCF7* and downregulated in the extended CD8 TIP) has been shown to directly repress *CXCR6* expression[34] (upregulated in the CD8 TIP), suggesting that this central regulator of naive and resting T cells[46] represses $CD8^+$ T cell chemoattraction to *CXCL16* expressed by the malignant cells.

A malignant cell state marks and predicts T/NK cell abundance

Mapping the spatial distributions of T/NK cells within the malignant compartment revealed that TILs preferentially colocalize with a subset of malignant cells (Methods, Fig. 3a–c, Extended Data Fig. 5a and Supplementary Table 6a). Although malignant cell states are highly patient specific (Supplementary Fig. 4b) and vary also within patients (Supplementary Fig. 4c–f), we found that the connection between TIL location and malignant cell gene expression appeared repeatedly

Fig. 2 | Immune cell states mark immune cell tumor infiltration status. **a**, UMAP embedding of $CD8^+$ T cells (Discovery dataset) derived from gene expression of all genes (top) or only T cell-specific genes (bottom). **b**, The association (*P* value and effect size, LMM) of each gene (row) from the CD8 TIP with immune cell infiltration status, when considering $CD8^+$ T cells and other immune cell types in the Discovery dataset (columns). **c**, Representative ST images from the Validation 1 dataset depicting the CD8 TIP identified in the Discovery dataset. *P* values denote per tissue core if the expression of the CD8 TIP is significantly higher in $CD8^+$ T cells with a high (above median) versus low (below median) abundance of malignant cells within a radius of 30 µm (one-sided *t*-test). **d**, UMAP embedding of $CD8^+$ T cells (Validation 1 dataset) from gene expression alone. **e**, Average gene expression (*z* score) in fibroblasts (Discovery dataset) of the top 50 desmoplasia-associated genes (columns) in each tissue profile (rows, $n = 87$). **f**, Representative tissue section (HGSC24, adnexa, Discovery dataset, 1 of 100), wherein the desmoplasia-associated genes capture stromal morphology on the per-cell level ($n = 1{,}968$ fibroblasts, *P* value $= 7.23 \times 10^{-80}$, one-sided Wilcoxon rank-sum test). These results were observed repeatedly across samples, as shown in **e**. **g**, Ligand–receptor interactions (lines) consisting of genes from the CD8 TIP and their respective ligand/receptor in the malignant compartment and stromal compartment. The arrows connect each gene to the cell type where it was found to mark the malignant or stromal compartment.

https://doi.org/10.1038/s41590-024-01943-5

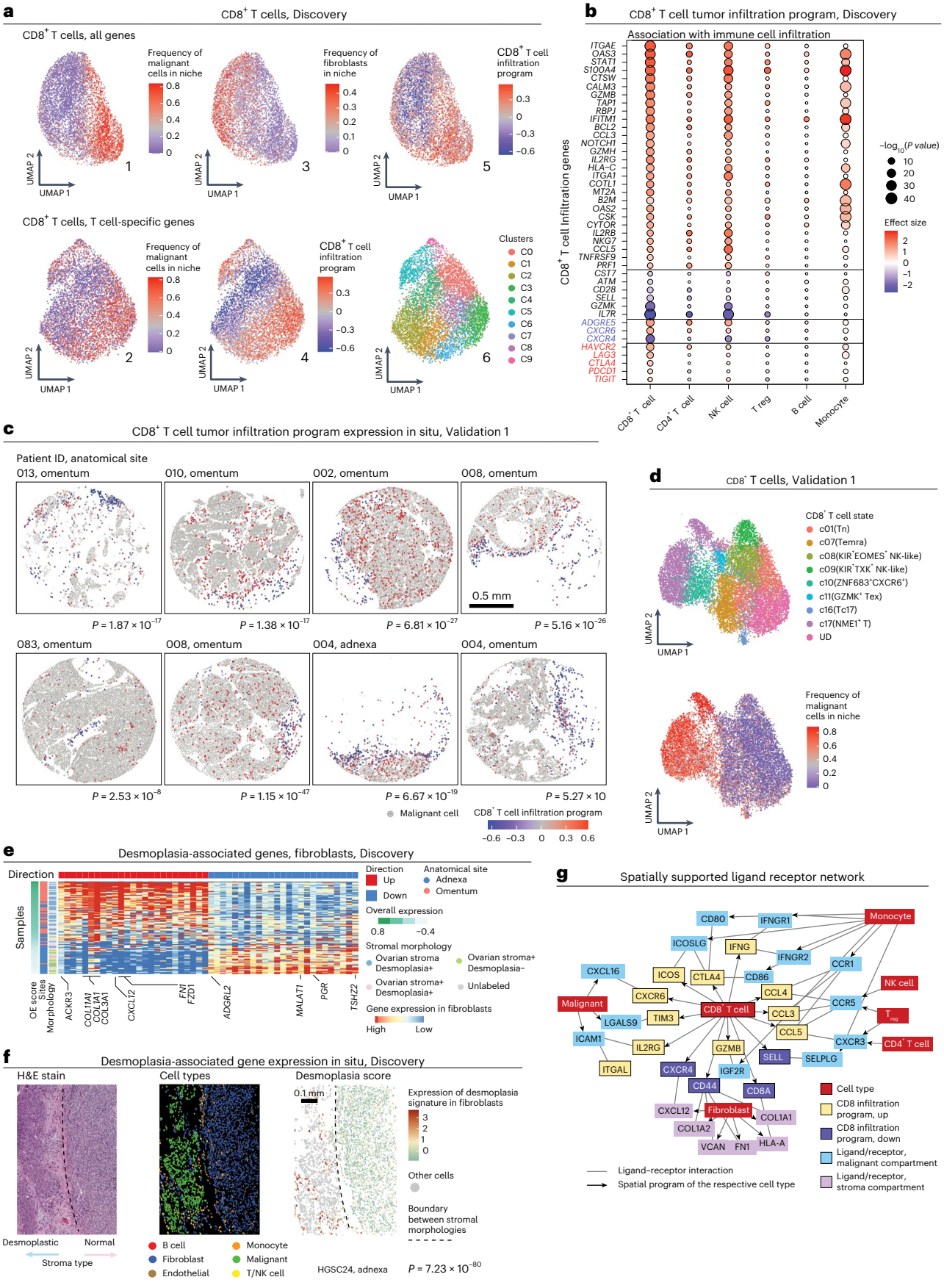

https://doi.org/10.1038/s41590-024-01943-5

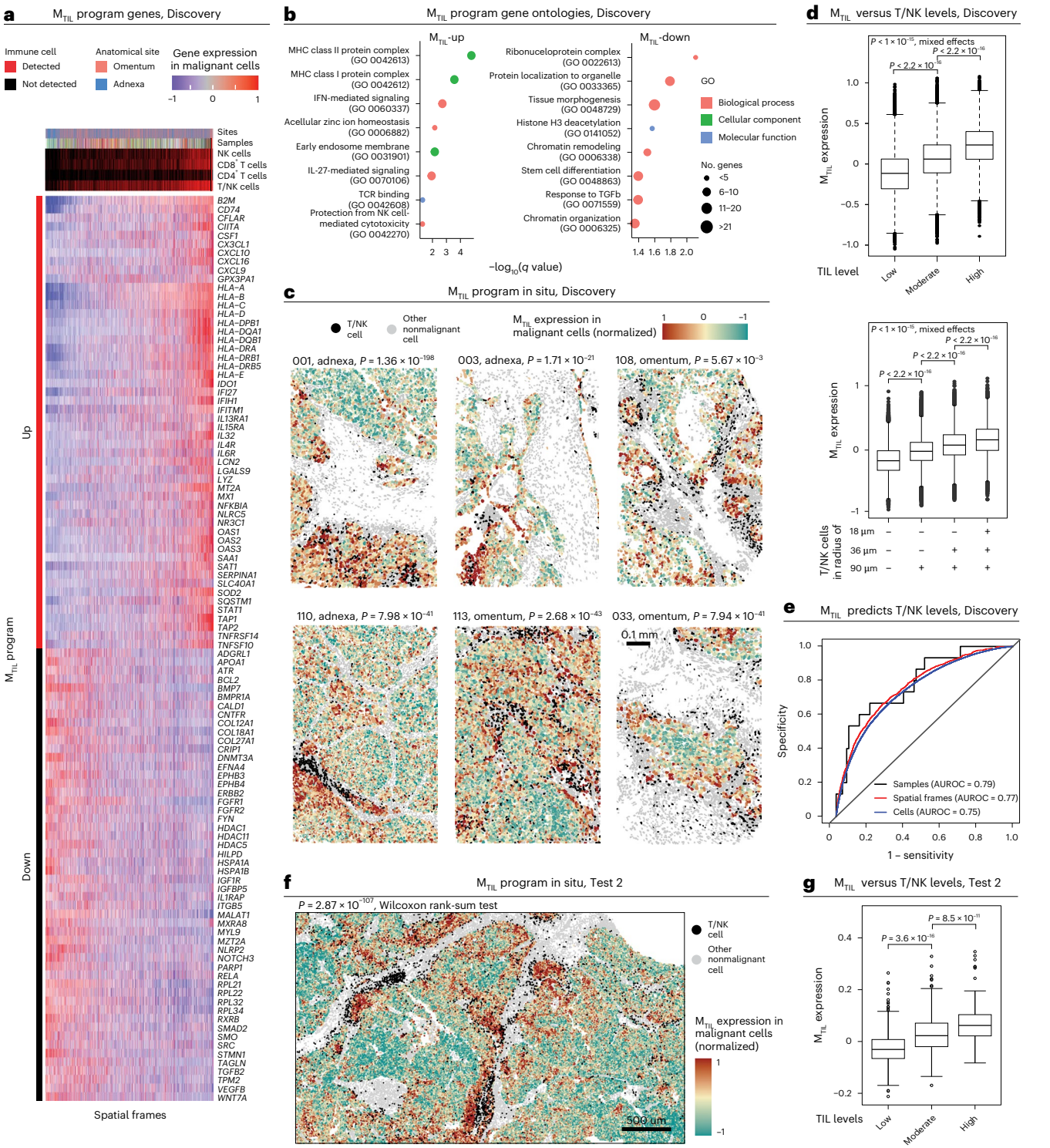

Fig. 3 | Malignant cell transcriptional program marks and predicts T/NK cell infiltration. a, Heat map of genes in the M_{TIL} (malignant transcriptional program that robustly marks the presence of TILs) program (Discovery dataset). Average expression of the top 104 M_{TIL} genes (rows) across spatial frames (columns). **b**, Top gene sets enriched in M_{TIL} based on Gene Ontology (GO) enrichment analysis. **c**, M_{TIL} spatial distributions in six representative tumor tissue profiles (6 of 100, Discovery dataset). *P* values denote if M_{TIL} expression is significantly (one-sided *t*-test) higher in frames with high-versus-low T/NK abundance, defined based on the median level in the respective tissue section. Matching cumulative analysis is provided in Extended Data Fig. 5e. **d**, M_{TIL} expression in each malignant cell (Discovery dataset, $n = 297{,}960$ cells), stratified based on the relative abundance of T/NK cells in their surroundings (top) and the presence of T/NK cells at different distances (bottom). **e**, ROC curves obtained for cross-validated SVM classifier using M_{TIL} expression in malignant cells (Discovery dataset) to predict T/NK cell levels, at the sample, spatial frame and single-cell levels. **f**, M_{TIL} spatial distributions in a representative region from one (of four) whole-tissue section (HGSC1, adnexa, Test 2 dataset; M_{TIL} expression in TIL-high versus TIL-low niches, $P = 2.87 \times 10^{-107}$, one-sided Wilcoxon rank-sum test). A full view of the whole-tissue section is provided in Extended Data Fig. 6g. **g**, Mean M_{TIL} expression in malignant cells in each FOV (Test 2 dataset, $n = 878$ FOVs), stratified based on the relative abundance of T/NK cells in each FOV. In **d** and **g**, in the box plots, the middle line denotes the median, box edges indicate the 25th and 75th percentiles, and whiskers extend to the most extreme points that do not exceed ±1.5 times the IQR; further outliers are marked individually with circles (minima/maxima). *P* values of group comparisons are derived from a one-sided Student's *t*-test.

across the heterogeneous tumors in our cohort and external cohorts (Fig. 3 and Extended Data Figs. 5 and 6).

Formulating these findings, we used the Discovery dataset to identify a malignant transcriptional program that robustly marks the presence of TILs, abbreviated as the malignant TIL (M_{TIL}) program (Fig. 3a, Extended Data Fig. 5a,b and Supplementary Table 6a). The program consists of 100 upregulated and 100 downregulated genes whose expression in malignant cells is significantly (BH FDR < 0.05, LMM) positively (M_{TIL}-up) and negatively (M_{TIL}-down) correlated with and predictive of T/NK cell infiltration (Fig. 3d,e). M_{TIL} overall expression in malignant cells (Methods) reflects both inter-sample and intra-sample variation in T/NK cell levels (Fig. 3d, e), irrespective of anatomical site ($P < 1 \times 10^{-30}$, LMM; Extended Data Fig. 5c). M_{TIL} continuously increases as a function of T/NK cell abundance and proximity, also when stratifying the T/NK population into its respective cell subtypes (Extended Data Fig. 5d,e). M_{TIL} is associated and predictive of T/NK cell levels both in the Validation (Extended Data Fig. 6a,b,f) and Test datasets, generalizing to unseen patients (Extended Data Fig. 6c,f) and whole-tissue sections (Fig. 3f,g, Extended Data Fig. 6d,f,g and Supplementary Fig. 6). Likewise, an independent scRNA-seq dataset[47] demonstrates that M_{TIL} expression in malignant cells is highest in tumors annotated as 'infiltrated', moderate in tumors annotated as 'excluded' and lowest in tumors annotated as 'immune desert' (Extended Data Fig. 6e).

Gene-set enrichment analyses demonstrate the connection between M_{TIL} and immune evasion[48–53]. M_{TIL}-up includes chemokines (for example, *CCL5*, *CXCL10*, *CXCL9* and *CXCL16* the cognate ligand to *CXCR6*), and oxidative stress genes (for example, *GPX3* and *SOD2*; Fig. 3a,b), and is enriched with multiple immune response genes, including antigen presentation (for example, *B2M*, *CIITA* and *HLA-A/HLA-B/HLA-C*), interferon gamma response genes (for example, *IDO1*, *IFI27*, *IFIH1*, *OAS1/OAS2/OAS3*, *JAK1* and *STAT1*) and cell adhesion molecules (for example, *ICAM1*, *ITGAV* and *ITGB2*; BH FDR = 1.91×10^{-9}, 2.86×10^{-10}, 4.59×10^{-2}, respectively, hypergeometric test; Fig. 3b and Supplementary Table 6b). M_{TIL}-up also includes immune suppression genes, most notable is *LGALS9*, encoding galectin 9—the ligand of the immune checkpoint TIM3 (that is, *HAVCR2*), which is upregulated in the infiltrating T/NK cells (Fig. 2g). However, there is no significant correlation between M_{TIL} and the expression of exhaustion signatures in the nearby T cells ($r_s < 0.046$, $P > 0.05$, Spearman correlation, Discovery dataset; Supplementary Table 6c). M_{TIL}-down reflects diverse processes including Wnt signaling (for example, *CTNNB1*, *FZD3/FZD4/FZD6*, *SMO*, *FGFR2* and *WNT7A*), epigenetic regulation (*DNMT3A* and *HDAC1/HDAC11/HDAC4/HDAC5*), insulin signaling (for example, *IGFR1* and *IGFBP5*) and cell differentiation (for example, *BMP7*, *BMPR1A*, *ETV4*, *FGFR1/FGFR2*, *FYN*, *S100A4*, *SMAD4* and *SMO*; BH FDR < 0.05, hypergeometric test; Fig. 3b and Supplementary Table 6b). Comparing the M_{TIL} program to 13 malignant signatures previously identified in a comprehensive HGSC scRNA-seq study[17], we found that 156 of the 200 genes in the M_{TIL} program were not included in any of these signatures (Supplementary Table 6d).

In our cohort, M_{TIL} expression is not associated with patient age at diagnosis, disease stage, neoadjuvant chemotherapy, TMB or sample anatomical site (Supplementary Fig. 7 and Supplementary Table 7a–c), but it is moderately positively associated with pathogenic *BRCA1/BRCA2* mutations ($P = 0.0423$, LMM). M_{TIL} expression is associated with improved overall survival, both in our cohort ($n = 54$, $P = 0.011$, Cox regression, based on mean expression of malignant cells in adnexal tumors, while controlling for age at diagnosis, disease stage and treatment history; Fig. 4a,b, Supplementary Table 8a–d and Methods), and in an external HGSC cohort ($n = 111$, $P = 0.024$, Cox regression, controlling for patient age and stage; Fig. 4c).

Testifying to its generalizability, M_{TIL} expression in malignant cells is predictive of T/NK cells in the vicinity of the malignant cells also in a previously published SMI dataset collected from five patients with non-small cell lung cancer (NSCLC)[21] (area under the receiver operating characteristic (AUROC) curve > 0.71; Extended Data Fig. 6h,i). Likewise, M_{TIL} expression was significantly correlated with the expression of a T/NK cell signature in external bulk gene expression datasets, both in HGSC ($n = 578$, $r_s = 0.72$, $P < 2.2 \times 10^{-16}$, Spearman correlation) and other cancer types ($r_s > 0.66$, $P < 1 \times 10^{-9}$, Spearman correlation; Supplementary Fig. 8a). However, although M_{TIL} is strongly supported by bulk gene expression data as a marker of T/NK cell levels, attempting to rediscover the M_{TIL} signature based on the covariation structure of HGSC bulk gene expression data across patients resulted in poor performances (area under the precision recall curve (AUPRC) of 0.202 and 0.306 for the prediction of M_{TIL}-up and M_{TIL}-down genes, respectively; Supplementary Fig. 8b), underscoring the need for single-cell ST studies.

To expand beyond the 960-gene panel in the Discovery dataset, we identified 200 additional genes that were significantly coexpressed with the M_{TIL} program based on the Test 1 dataset (Supplementary Table 6e and Methods), and among these are *RUNX1*, CCAAT/enhancer-binding protein-encoding genes (*CEBPB* and *CEBPD*, which encode for subunits of the RUNX1 co-activation complex[54,55]), and complement genes (*C1S* and *C3*) as a part of the extended M_{TIL}-up module, as well as the stem cell marker encoded by *LGR5*, and the BAF complex subunit encoded by *SMARCB4*, as a part of the extended M_{TIL}-down module.

M_{TIL} expression predicts clinical response to ICB

We hypothesized that higher M_{TIL} expression may represent more immunogenic malignant cell states and could thus be predictive of clinical responses to ICB in HGSC and potentially other cancer types. As genomic datasets from ICB trials are currently not available in HGSC and given the generalizability of the M_{TIL} program to other cancer types (Extended Data Fig. 6h,i and Supplementary Fig. 8a), we tested this hypothesis in five external bulk gene expression datasets obtained from tumor samples of other cancer types before ICB treatment.

The M_{TIL} program overall expression scores (Methods) were predictive of ICB response in four of the five cohorts that we tested. M_{TIL} scores were predictive of ICB responses in the melanoma cohort[56] ($n = 152$, $P = 1.35 \times 10^{-3}$, progression-free survival (PFS) Cox regression, controlling for patient sex, treatment status, TMB and anatomical site; patient age was not available, Fig. 4c), NSCLC cohort[57] ($n = 121$, $P = 0.027$, PFS Cox regression model, controlling for patient sex, age, smoking status and tumor histological type; Fig. 4c) and in two independent arms of the I-SPY2 trial in HER2-negative breast cancer[58,59] (durvalumab/olaparib, $n = 71$, $P = 2.52 \times 10^{-4}$, one-sided *t*-test, AUROC = 0.65, and pembrolizumab/paclitaxel: $n = 69$, $P = 6.37 \times 10^{-3}$, one-sided *t*-test; AUROC = 0.70; Fig. 4d). In the urothelial cancer cohort[60], M_{TIL} program scores and programmed death ligand 1 (PD-L1) levels were not predictive of clinical responses ($n = 205$, $P > 0.05$, one-sided *t*-test). Collectively, M_{TIL} predictive performances were comparable and, in several cases, superior to those of other ICB response biomarkers, including PD-L1 gene expression, TMB levels and estimates of TIL levels (Fig. 4e and Supplementary Fig. 8c).

Lastly, we note that M_{TIL} is not associated with TMB based on our data ($r_s = -0.077$, $P = 0.67$, Spearman correlation), as well as the melanoma and urothelial ICB cohorts, where TMB information was available ($r_s < 0.09$, $P > 0.32$, Spearman correlation). These findings suggest that M_{TIL} is an orthogonal property that is not directly linked to TMB but is predictive of ICB response in several cancer types.

M_{TIL} expression and T/NK cell abundance in the tumor as a function of CNAs

A key question is whether M_{TIL} is merely reflecting the response of malignant cells to the presence of TILs and is thus a surrogate marker of TILs, or whether M_{TIL} is regulated by other cell-intrinsic processes and is driving TIL infiltration and potentially also malignant cell susceptibility to TIL-mediated cytotoxicity, making it a causal predictive biomarker

https://doi.org/10.1038/s41590-024-01943-5

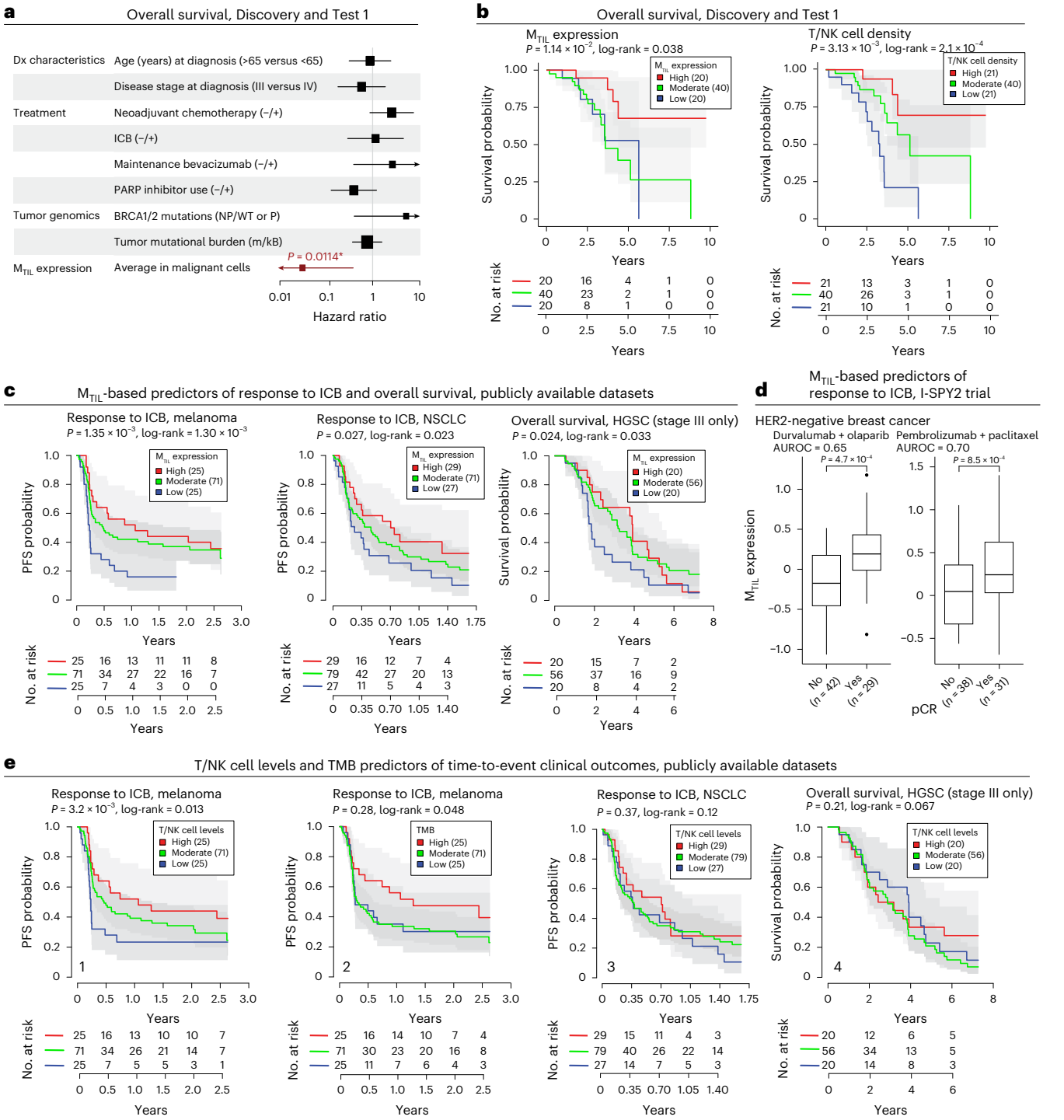

Fig. 4 | M_{TIL} predicts patient survival and ICB response. a, Hazard ratios (HRs) estimated for each predictor from multivariate Cox proportional hazards models of overall survival in the HGSC cohort of this study (Discovery and Test 1 datasets, $n = 30$ and 54 patients for genomic and non-genomic features, respectively). Bars indicate 95% confidence intervals (Methods). Arrowheads indicate that the 95% interval extends beyond the HR limits shown in the x axis. *P value < 0.05, multivariate Cox proportional hazards models. **b**, Kaplan–Meier curves and numbers-at-risk table of overall survival in patients with HGSC (Discovery and Test 1 datasets); patients stratified by average M_{TIL} expression (left), and T/NK cell density (right) in adnexal tumors. **c**, Kaplan–Meier curves and numbers-at-risk tables of ICB PFS probability (melanoma[56], left; NSCLC[57], middle) and overall survival (external HGSC cohort, right) with patients stratified by tumor M_{TIL} expression. **d**, M_{TIL} expression is significantly higher in patients with HER2-negative breast cancer with pCR (pathogenic clinical response) versus without pCR in two arms of the I-SPY2 clinical trial (durvalumab + olaparib ($n = 71$ patients)[58] and pembrolizumab + paclitaxel ($n = 67$ patients)[59]). In the box plots, the middle line denotes the median, box edges indicate the 25th and 75th percentiles, and whiskers extend to the most extreme points that do not exceed ±1.5 times the IQR; further outliers are marked individually (minima/maxima). P values derived from one-sided Student's t-test. **e**, T/NK cell levels estimated from bulk transcriptomics and TMB (mut/kB) as predictors of ICB responses in the datasets shown in **c**. Kaplan–Meier curves and numbers-at-risk tables of ICB PFS probability in patients with melanoma[56] stratified by T/NK cell levels (1) and TMB (2), and in patients with NSCLC[57] stratified by T/NK cell levels (3), and of overall survival in patients with HGSC stratified by T/NK cell levels (4). In **b**, **c** and **e**, P values were calculated from the Wald statistic of covariate-controlled Cox proportional hazards regression models. The log-rank P value was derived from comparing discretized predictors (high = top quartile versus low = bottom quartile).

https://doi.org/10.1038/s41590-024-01943-5

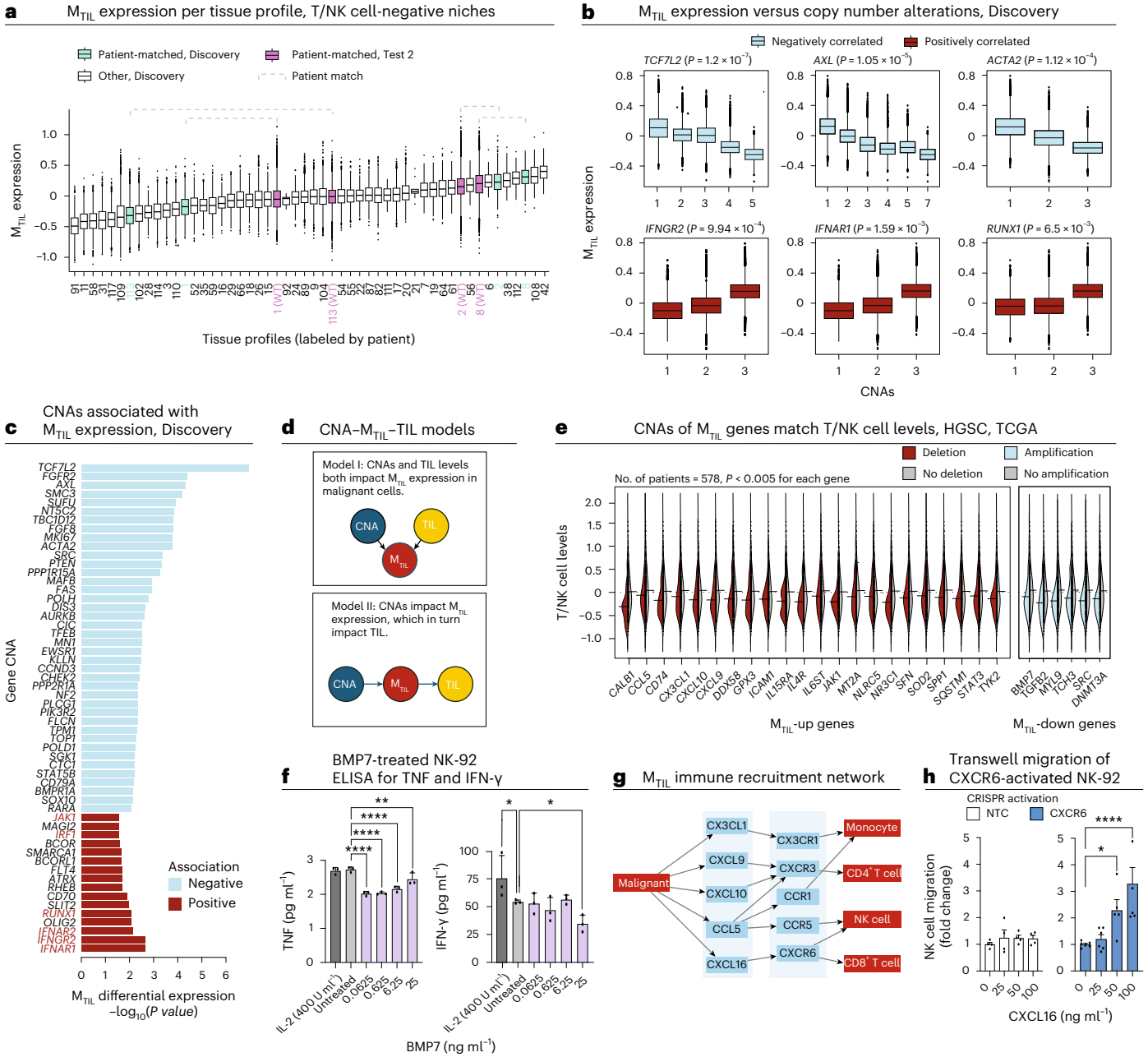

Fig. 5 | Genetic association with M_{TIL} and T/NK cell levels. a, M_{TIL} expression in adnexal malignant cells (Discovery and Test 2 datasets, $n = 264{,}825$ cells) residing in tissue niches where T/NK cells were not detected, stratified by tissue profiles labeled by patient and dataset. Dashed brackets indicate adnexal malignant cells from patient-matched tissue profiles from Discovery and Test 2. **b**, M_{TIL} expression in malignant cells (Discovery dataset), stratified by somatic copy number of six respective genes based on patient-matched bulk tumor genomic profile (LMM, $n = 40$ patients). **c**, Top CNAs showing a significant (BH FDR < 0.05, LMM; Methods) association with M_{TIL} expression in malignant cells in the Discovery dataset. **d**, CNA–M_{TIL}–TIL models. **e**, Deletion (red) of M_{TIL}-up genes and amplification (light blue) of M_{TIL}-down genes that are significantly (BH FDR < 0.05, one side *t*-test) associated with low T/NK cell levels (estimated based on gene expression of T/NK cell signatures; Methods) in an independent TCGA HGSC cohort of 578 patients[12]. Exact *P* values are provided in Supplementary Table 9a. **f**, ELISA quantification of IFN-γ (1:100) and TNF (undiluted) in NK-92 supernatant treated with various concentrations of recombinant human BMP7. **g**, M_{TIL} chemokines and the matching chemokine receptors in immune cell TIPs. **h**, Fold change of NK-92 cell migration of CXCR6$^+$ NK-92 cells derived via CRISPR activation (Supplementary Fig. 9) versus control NK-92 cells (transduced with non-targeting control CRISPR activation guides, left) at varying CXCL16 concentrations. In the box plots in **a** and **b**, the middle line denotes the median, box edges indicate the 25th and 75th percentiles, and whiskers extend to the most extreme points that do not exceed ±1.5 times the IQR; further outliers are marked individually with circles (minima/maxima). In **f** and **h**, error bars represent the mean ± s.d. for **f** and mean ± s.e.m. for **h**; comparisons are indicated via brackets; $^*P < 0.05$, $^{**}P < 0.01$, $^{***}P < 0.001$, $^{****}P < 0.0001$ (ordinary one-way ANOVA); brackets that are not shown denote nonsignificant ($P > 0.05$) comparisons. Data from $n = 3$ biological replicates were collected per condition in **f** and $n = 4$ technical replicates were collected per condition in **h**.

of ICB responses. Given the strong connection we observed between CNAs and malignant cell transcriptomes (Supplementary Fig. 4a), we turned to examine the connection between M_{TIL} expression and CNAs to probe at this question.

First, we note that M_{TIL} inter-patient variation supersedes its intra-tumoral variation, as observed also after regressing out the impact of the tumor microenvironment compositions, or when considering only malignant cells in TIL-deprived environments (Fig. 5a; $P < 1 \times 10^{-30}$,

https://doi.org/10.1038/s41590-024-01943-5

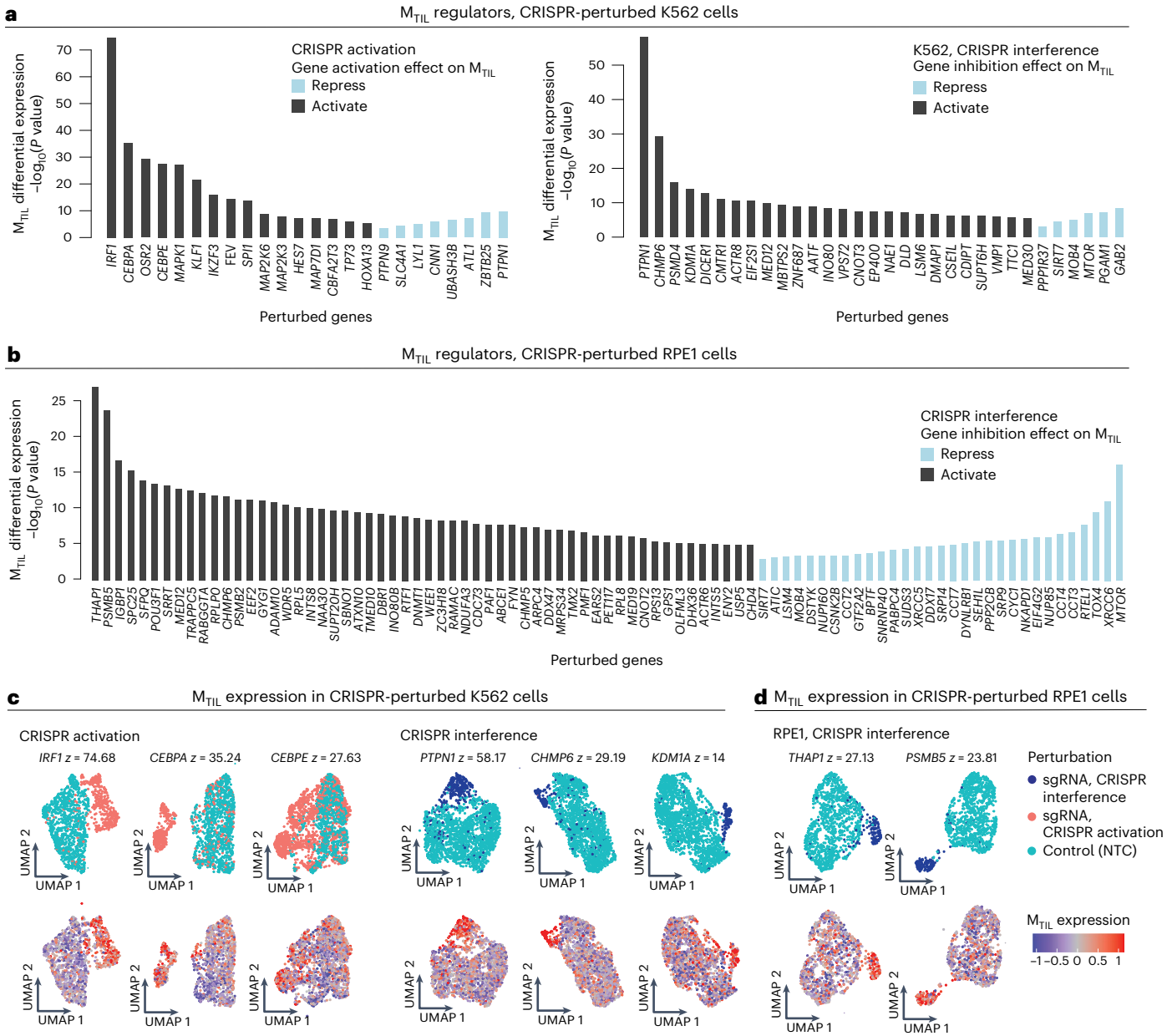

Fig. 6 | Meta-analyses of Perturb-seq datasets identify regulators of the M_{TIL} program. a,**b**, Differential M_{TIL} expression (two-sided *t*-test comparing cells with the respective perturbation to cells with control sgRNAs) for M_{TIL} altering perturbations identified in K562 (myelogenous leukemia) (**a**) and RPE1 (human retinal pigment epithelial) (**b**) cell lines Perturb-seq data[65,66]. **c**,**d**, Representative UMAP embeddings of M_{TIL} altering perturbation: cells were labeled based on the sgRNA detected (top) and based on M_{TIL} expression (bottom) in K562 (**c**) and RPE1 (**d**) cell lines. *z* denotes $-\log_{10}$(*P* value), two-sided *t*-test, comparing M_{TIL} expression in the perturbed versus control cells.

analysis of variance (ANOVA) test). Moreover, when considering only malignant cells that are in TIL-deprived niches in the tumor, the M_{TIL} score is still predictive of whether the entire tumor tissue core has high/low TIL levels (AUROC = 0.76, 0.89 and 0.83, when predicting which samples have TIL levels above the median, and 75th and 85th percentiles).

Second, in addition to RNA–CNA associations in *cis* (Supplementary Fig. 4a), M_{TIL} expression strongly correlated with the copy number of multiple genes in our cohort (Methods). Among the positively correlated ones are interferon receptors *IFNGR2*, *IFNAR1* and *IFNAR2*, as well as interferon regulatory factor 1 (*IRF1*) and *RUNX1*, and the top negatively correlated ones being *TCF7L2*, *FGFR2* and *AXL* ($P < 5 \times 10^{-3}$, LMM; Fig. 5b,c).

Third, CNAs of M_{TIL} genes are predictive of TIL abundance scores in an independent cohort from The Cancer Genome Atlas (TCGA) of 578 HGSC tumors[12] (AUROC = 0.82, on unseen test samples, support vector machine (SVM) model; Methods), such that tumors with amplification of M_{TIL}-down genes (for example, *BMP7*, *DNMT3A*, *FZD3*, *MYL9*, *SRC* and *TGFB2*) or deletion of M_{TIL}-up genes—including both chemokines (*CX3CL1*, *CXCL10*, *CXCL9*, *CXCL16* and *CCL5*) and other genes (for example, *ICAM1*, *GPX3* and *NR3C1*)—have significantly lower TIL abundance scores compared to tumors without these copy number changes (BH FDR < 5.0×10^{-3}, one-sided *t*-test; Fig. 5d,e and Supplementary Table 9a).

Mechanistically, the composite effect of CNAs (or other forms of genetic/epigenetic aberrations) in M_{TIL} genes and regulators can lead to immune evasion through diverse mechanisms. To demonstrate this, we show that *BMP7*—one of the topmost repressed genes in the M_{TIL} program (Extended Data Fig. 5a) that is amplified in TIL-deprived HGSC tumors (Fig. 5e)—suppresses IFN-γ and tumor necrosis factor (TNF) secretion in

NK-92 cells (Fig. 5f). Likewise, M_{TIL} chemokines whose deletion was associated with low TIL levels in the TCGA data (*CXCL9*, *CXCL10*, *CXCL16*, *CCL5* and *CX3CL1*; Fig. 5e) recruited different subsets of TILs and other immune cells based on ligand–receptor colocalization analyses in the HGSC spatial data (Fig. 5g). To functionally demonstrate this, we activated *CXCR6* in NK-92 cells via CRISPR–dCas9 activation (Methods and Supplementary Fig. 9a,b) and showed a dose-dependent and CXCR6-dependent NK cell directional migration toward CXCL16 (Fig. 5h).

M_{TIL} sensitizes cancer cells to T/NK cell cytotoxicity

Given our findings and previous studies where genes and pathways represented in the M_{TIL} program have been shown to have an important function in antitumor immune responses[61–64], we hypothesized that M_{TIL} reflects not only the response of malignant cells to TILs, but also an intrinsically regulated malignant cell state that impacts TIL-mediated tumor control. Supporting this hypothesis, a collection of previously published CRISPR screens[48–52] shows that M_{TIL}-up is enriched with genes that sensitize cancer cells to immune-mediated selection pressures (including *ICAM1*, *JAK1*, *NLRC5*, *SOD2* and *STAT1*; $P = 1.82 \times 10^{-4}$, hypergeometric test), while M_{TIL}-down includes genes with desensitizing effects (*BCL2*, *FGFR1*, *HDAC1*, *HDAC5*, *ITGB5* and *RELA*).

To functionally probe the M_{TIL} program genes and examine their effect on ovarian cancer cell response to lymphocyte cytotoxicity, we performed high-content CRISPR knockout (KO) screens in ovarian cancer cells in monoculture and two types of co-cultures with cytotoxic T lymphocytes (CTLs), including one co-culture with T cell antigen receptor (TCR)-engineered $CD8^+$ T cells and another co-culture with NK cells.

Instead of targeting only genes in the M_{TIL} program itself, we devised a meta-analysis pipeline to identify program regulators based on available Perturb-seq datasets (Methods). Using three previously published Perturb-seq datasets[65–67] (Supplementary Fig. 10a), we identified 43 and 104 perturbations that result in significantly higher and lower expression of the program, respectively (Fig. 6a–d, Supplementary Fig. 10b,c, Supplementary Table 10a and Methods). Demonstrating the value of this approach, it revealed a wider and more diverse set of regulators, most of which are not included in the M_{TIL} program itself or not included in the gene panel of the Discovery dataset (Supplementary Table 1b). The positive regulators are enriched (BH FDR < 0.05, hypergeometric test) for genes involved in telomere maintenance (for example, *CCT3/CCT4/CCT7*, *RTEL1*), transcriptional regulators (for example, *DDX17*, *IKZF3*, *KLF1*, *MTOR*, *SIRT7*, *TP73* and *XRCC6*), protein metabolism (for example, *CYC1*, *SRP14* and *SRP9*) and cytokine signaling (for example, *IRF1*, *NUP85* and *SEH1L*). The positive M_{TIL} regulators also include the RUNX1 complex genes (*CBFA2T3*, *CEBPA* and *CEBPE*), aligned with our findings that CNAs of *RUNX1* are positively associated with the M_{TIL} program (Fig. 5c) and that RUNX1 is a part of the extended M_{TIL} program. Negative M_{TIL} regulators are enriched for chromatin organization (for example, *DNMT1*, *INO80*, *TAF10* and *WDR5*), Wnt pathway, Myc targets and immune resistance genes[48–52,68] (BH FDR < 1×10^{-3}, hypergeometric test). The top negative regulator identified here is *PTPN1*, which is supported by both gene activation and inhibition screens (Fig. 6a,c).

Based on these findings, we designed a pooled knockout screen of 74 M_{TIL} genes and regulators (Supplementary Table 10a,b) to test their function in ovarian cancer cells (TYK-nu cell line; Fig. 7a and Extended Data Figs. 7 and 8). Mapping fitness upon genetic perturbations under both adaptive and innate immune selection pressures (Fig. 7a,b; BH FDR < 0.05, MAGeCK; Methods) along with Perturb-seq scRNA-seq readouts in monoculture and co-culture with NK cells (Fig. 7a,c), we identified perturbations that activate or repress the program and tracked subsequent effects of these perturbations on immune escape. In total, we profiled 18,585 high-quality single-cell transcriptomes, each assigned to an ovarian cancer cell with a single guide RNA (sgRNA) confidently identified, and a median of 4,251 genes detected per cell (Fig. 7c and Extended Data Fig. 9a). Differentially expressed genes were identified for each gene knockout across the three conditions (Fisher's method; Methods), resulting in 74 gene 'perturbation signatures' (Methods and Extended Data Fig. 9b,c) that were then used to identify gene knockouts that significantly repressed or activated the M_{TIL} program, denoted as 'activators' and 'repressors', respectively (Fig. 7d and Methods).

Validating our hypothesis and approach, the top perturbations activating the program—*PTPN1* and *ACTR8* KO—sensitize malignant cells to T/NK cell cytotoxicity (Fig. 7b,d,e and Extended Data Fig. 9b), while the top perturbations that repress the program, *IFNGR1*, *IRF1* and *STAT1* KOs, confer resistance to T cell-mediated killing (Fig. 7b,d,e and Extended Data Fig. 9b). This further supports the causal link between CNAs of interferon signaling genes and M_{TIL} expression (Fig. 5c). Knockout of M_{TIL} repressors *ACTR8*, *PTPN1*, *FGFR1*, *MAPK1* and *MED12* was found to sensitize cancer cells to immune elimination also in previous in vivo CRISPR screens[48–52]. Demonstrating that the transcriptional response to TILs can be genetically rewired, our data also show that knockout of M_{TIL} repressors (*ACTR8*, *DNMT1*, *FGFR1*, *PTPN1*, *MED12* and *MIF*) mimics and amplifies the transcriptional responses to NK cells, while knockout of M_{TIL} activators, as *STAT1*, *IFNGR1*, *INTS2*, *IRF1*, *PARP12* and others, represses and counteracts the transcriptional response to NK cells (Fig. 7f–h and Extended Data Fig. 9c).

To examine if the inhibition of M_{TIL} repressors substantially impacts immune-based cancer cell elimination, we generated syngeneic *PTPN1* and *ACTR8* KO TYK-nu ovarian cancer lines (Extended Data Fig. 10a,b). Both knockouts significantly sensitized the cancer cells to both NK cell-mediated cell death ($P = 6.29 \times 10^{-14}$ and $P = 8.79 \times 10^{-15}$ for *PTPN1* KO and *ACTR8* KO, respectively; time-controlled LMM in comparison to non-targeting control (NTC)) and T cell-mediated cell death ($P = 6.53 \times 10^{-34}$ and $P = 6.58 \times 10^{-25}$ for *PTPN1* KO and *ACTR8* KO, respectively; time-controlled LMM in comparison to NTC), as quantified over 16-h monitoring of caspase-3/caspase-7 activity in monoculture versus co-culture with NK-92 cells (Fig. 8a) and co-culture with TCR-engineered $CD8^+$ T cells (Fig. 8b). Although *ACTR8* is considered an essential gene (Supplementary Table 10c), its knockout did not impact ovarian cancer cell viability (Fig. 8a and Extended Data Fig. 10b). Focusing on NK cell-mediated killing, we tested the *PTPN1/PTPN2* inhibitor ABBV-CLS-484 (refs. 50,69) in both the TYK-nu and OVCAR3 cell lines. The drug had minimal effect on cell viability in monoculture (Fig. 8c) but led to a substantial increase in ovarian cancer cell killing by NK cells, as observed for both ovarian cancer cell lines across a range of doses ($P = 5.10 \times 10^{-17}$ and $P = 1.61 \times 10^{-30}$, for TYK-nu and OVCAR3, respectively; dose-controlled LMM; Fig. 8c).

Discussion

Here we provide a comprehensive spatial mapping of HGSC tumors, revealing generalizable principles of tissue organization and

Fig. 7 | High-content CRISPR screens identify perturbations that de-repress or repress M_{TIL}. a, Overview of experimental design. Created with BioRender.com. **b**, Ovarian cancer cell (TYK-nu) differential fitness (MAGeCK[82]) under $CD8^+$ T cell and NK cell selection pressures. **c**, UMAP of scRNA-seq profiles from Perturb-seq screen. Each dot corresponds to an ovarian cancer cell (TYK-nu) with 1 of the 232 guides confidently detected, cultured in monoculture or co-culture with NK cells at a 1:1 or a 2.5:1 effector-to-target ratio. **d**, Differential expression of M_{TIL} genes (Fisher's combined test; Methods) when comparing ovarian cancer cells with the respective gene KO to those with NTC sgRNAs. **e**, Differential expression of M_{TIL}-up genes upon different gene KOs under different conditions, shown for genes identified as M_{TIL} repressors or activators. **f**–**h**, Gene KOs alter the cancer cell transcriptional response to NK cells. **f**, Differential expression of the gene KO signature in control ovarian cancer cells in monoculture versus co-culture (two-sided *t*-test). **g**, Gene KO signature expression in control ovarian cancer cells in monoculture versus co-culture; statistical significance per KO shown in **f**. **h**, UMAPs as in **c** with cells colored according to differential gene KO signature expression.

https://doi.org/10.1038/s41590-024-01943-5

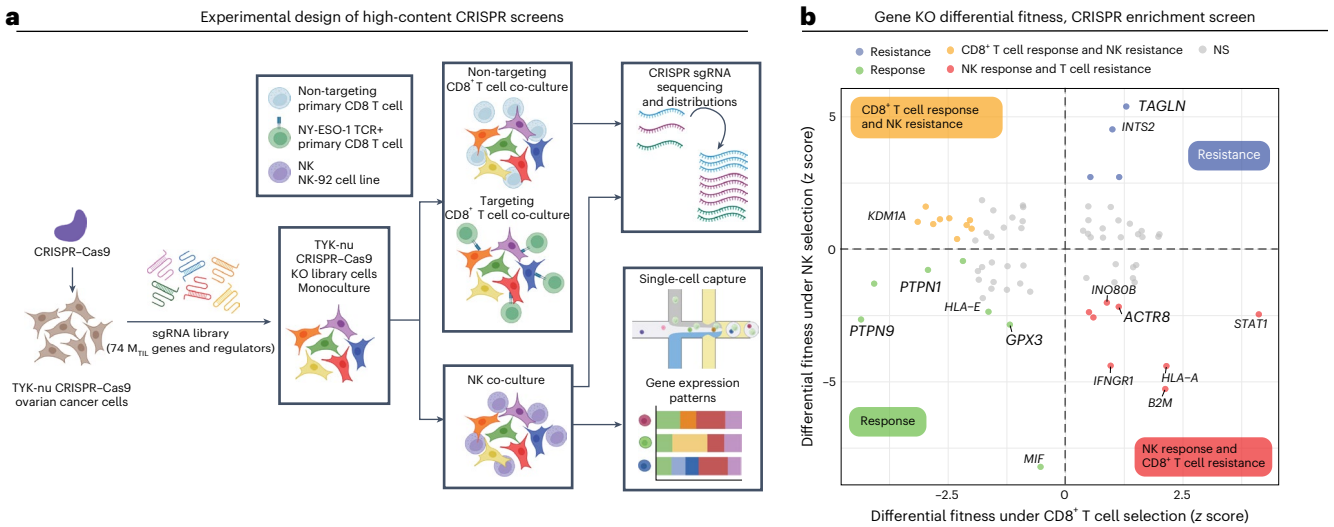

https://doi.org/10.1038/s41590-024-01943-5

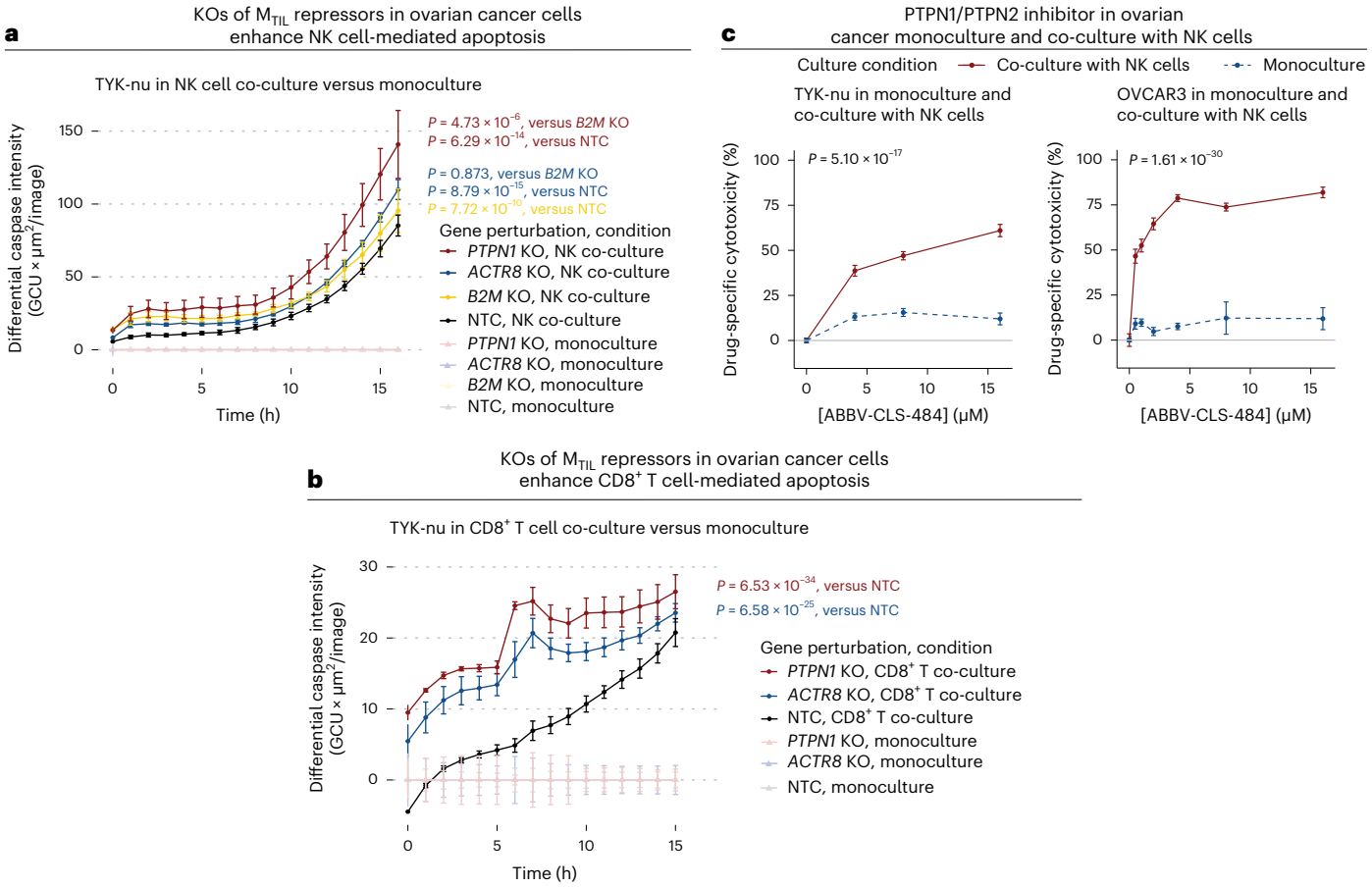

Fig. 8 | Inhibiting M$_{TIL}$ repressors sensitizes cancer cells to T/NK cell-mediated cytotoxicity. a, Fluorescent caspase-3/caspase-7 activity monitored in NTC and *PTPN1*, *ACTR8* and *B2M* KO syngeneic TYK-nu cell lines in monoculture and co-culture with NK-92 cells over 16 h. **b**, Fluorescent caspase-3/caspase-7 activity monitored in NTC, *PTPN1* and *ACTR8* KO syngeneic TYK-nu cell lines in monoculture and co-culture with TCR-specific CD8$^+$ T cells over 16 h. In **a** and **b**, *P* values were derived from Satterthwaite's ANOVA in time-controlled two-sided LMMs; $n = 3$ technical replicates per experimental condition. **c**, *PTPN1*/*PTPN2* inhibitor (ABBV-CLS-484) increased NK-mediated cytotoxicity in TYK-nu (left) and OVCAR3 (right) ovarian cancer cell lines in a dose-dependent manner. *P* values were derived from Satterthwaite's ANOVA in dose-controlled two-sided LMMs; $n = 3$ technical replicates per experimental condition. For **a**–**c**, all data shown represent the mean + s.e.m. GCU, global counting unit.

lymphocyte infiltration within these aggressive and genetically unstable tumors. Our study demonstrates the connection between somatic genetic aberrations, malignant transcriptional dysregulation and immune evasion at the cellular and tissue levels, providing a new perspective to the barriers preventing the antitumor immune response in patients with HGSC and new leads to de-repress HGSC cancer immunogenicity.

Our study puts forward new frameworks to delineate complex multicellular processes and phenotypes through the lens of spatial organization. These include linking cell states to genetic variation across individuals and using existing Perturb-seq datasets to identify latent regulators of spatial cell states. We show that our data-driven approach provides a framework to uncover cell-state regulators, even when the transcriptional level of the regulator is not linked to the cell state of interest in the unperturbed state (for example, *PTPN1*). As available Perturb-seq datasets are still limited in their scope and diversity (Supplementary Discussion), it is likely that we are still not fully scanning the search space of cell-state regulators. In the case of the M$_{TIL}$ program, additional M$_{TIL}$ regulators beyond those identified here probably exist, as further suggested by our CNA analyses. As more Perturb-seq datasets, as the one generated here, become available across a more diverse range of cell types and conditions, it will be possible to use Perturb-seq data more effectively to extrapolate from one context to another with increasing accuracy[70,71] and, in the case of malignant cell states, using CNA-to-RNA and CNA-to-cell-state associations to further guide Perturb-seq experimental design.

The key findings from our study provide new leads and resources to study HGSC immune evasion toward new diagnostic and intervention strategies.

ICB and other immunotherapies have shown modest effects in tumors with low TIL levels at baseline[3,15]. Our findings demonstrate that this may be not only due to immune exclusion per se, but also due to malignant cell-intrinsic differences between TIL-rich and TIL-deprived tumors that protect malignant cells even in the presence of targeting CTLs. Supporting this model, we show that CTLs have a substantial effect on the cancer cell transcriptome (Fig. 7c), such that perturbing malignant cells to prevent or enhance this malignant cell transcriptional response significantly impacts cancer cell susceptibility to CTL cytotoxicity, as we show in highly controlled co-cultures where spatial segregation is unlikely to have a major effect.

We show that stratifying patients based on such malignant cell-intrinsic features—whether through gene expression or CNAs—can help determine patient response to ICB and which aspects of the immune response are genetically dysregulated. Instead of a single immune evasion driver, we propose that immune evasion in HGSC is a result of the composite effects of multiple gene deletions and amplifications that dysregulate both well-established mechanisms (as interferon signaling and chemokine mediated recruitment) as well as specific

genes and processes proposed by our analyses and data (for example, *BMP7* and *RUNX1*). As ST data provide a single snapshot in time, we also note that M_{TIL}-high areas that are deprived of TILs may mark situations where the snapshot is not representative of TIL location in the past or the probability that these areas will be infiltrated in the future. This may explain the improved ability of M_{TIL} to predict clinical response to ICB compared to TIL levels in certain cohorts.

We anticipate that the detailed mapping of HGSC tumors provided here will help inform the design of new interventions including T/NK cell engineering strategies to enhance T/NK cell infiltration. Our findings demonstrate that the stroma differentially retains or sequesters certain subsets of T/NK cells, but not others, providing new leads to activate or inhibit chemokine receptors as CXCR6 and CXCR4 to mobilize endogenous or engineered T/NK cells into the tumor. Our findings also underscore the need to map T cell clonality as a function of location at the micro level to examine whether T cells that reside in the malignant and stromal compartments are part of the same or different TCR clones, and dynamically track tumor-reactive T/NK cells to examine if these can egress back to the stroma to avoid or reverse exhaustion[72].

Our data provide new leads to target HGSC resistance, including the inhibition of *ACTR8* and *PTPN1*. *PTPN1*'s protein product PTP1b is inactivated by oxidation[73], which may explain M_{TIL} activation under oxidative stress (as indicated by the upregulation of *GPX3* and *SOD2*). PTP1b posttranscriptional regulation may also explain why it could not have been identified as an M_{TIL} regulator with a standard approach of gene expression correlations. PTP1b is a negative regulator of insulin and leptin signaling[74] that has been an attractive drug target for treatment of type 2 diabetes and obesity[75–78]. *PTPN1* KO mice have been shown to be viable and resistant to the development of obesity and diabetes, with more recent work demonstrating that PTPN1/PTPN2 inhibition is enhancing antitumor immune response, primarily via activation of $CD8^+$ T cells[50,69,79]. Here we show that *PTPN1* KO in ovarian cancer cells as well as its inhibition via ABBV-CLS-484 selectively sensitized ovarian cancer cells to both T cell-mediated and NK cell-mediated killing, providing rationale to include patients with HGSC in the ongoing phase I clinical trials (NCT04777994 and NCT04417465)[80,81].

Taken together, this integrative study provides a blueprint to functionally map and probe the molecular landscape of multicellular interplay in complex biological tissues and reveals spatial, molecular and genetic aspects of immune escape in HGSC, opening new avenues to activate targeted immune responses.

Online content

Any methods, additional references, Nature Portfolio reporting summaries, source data, extended data, supplementary information, acknowledgements, peer review information; details of author contributions and competing interests; and statements of data and code availability are available at https://doi.org/10.1038/s41590-024-01943-5.

References

1. Galon, J. & Bruni, D. Tumor immunology and tumor evolution: intertwined histories. *Immunity* **52**, 55–81 (2020).
2. Biswas, S. et al. IgA transcytosis and antigen recognition govern ovarian cancer immunity. *Nature* **591**, 464–470 (2021).
3. Chen, D. S. & Mellman, I. Oncology meets immunology: the cancer–immunity cycle. *Immunity* **39**, 1–10 (2013).
4. Leach, D. R., Krummel, M. F. & Allison, J. P. Enhancement of antitumor immunity by CTLA-4 blockade. *Science* **271**, 1734–1736 (1996).
5. Chamoto, K., Yaguchi, T., Tajima, M. & Honjo, T. Insights from a 30-year journey: function, regulation and therapeutic modulation of PD1. *Nat. Rev. Immunol.* https://doi.org/10.1038/s41577-023-00867-9 (2023).
6. Anderson, A. C., Joller, N. & Kuchroo, V. K. Lag-3, Tim-3, and TIGIT: co-inhibitory receptors with specialized functions in immune regulation. *Immunity* **44**, 989–1004 (2016).
7. Hegde, P. S. & Chen, D. S. Top 10 challenges in cancer immunotherapy. *Immunity* **52**, 17–35 (2020).
8. Sharma, P., Hu-Lieskovan, S., Wargo, J. A. & Ribas, A. Primary, adaptive, and acquired resistance to cancer immunotherapy. *Cell* **168**, 707–723 (2017).
9. Ribas, A. & Wolchok, J. D. Cancer immunotherapy using checkpoint blockade. *Science* **359**, 1350–1355 (2018).
10. Torre, L. A. et al. Ovarian cancer statistics, 2018. *CA Cancer J. Clin.* **68**, 284–296 (2018).
11. Macintyre, G. et al. Copy number signatures and mutational processes in ovarian carcinoma. *Nat. Genet.* **50**, 1262–1270 (2018).
12. Bell, D. et al. Integrated genomic analyses of ovarian carcinoma. *Nature* **474**, 609–615 (2011).
13. Garsed, D. W. et al. The genomic and immune landscape of long-term survivors of high-grade serous ovarian cancer. *Nat. Genet.* **54**, 1853–1864 (2022).
14. Jiménez-Sánchez, A. et al. Unraveling tumor–immune heterogeneity in advanced ovarian cancer uncovers immunogenic effect of chemotherapy. *Nat. Genet.* **52**, 582–593 (2020).
15. Joyce, J. A. & Fearon, D. T. T cell exclusion, immune privilege, and the tumor microenvironment. *Science* **348**, 74–80 (2015).
16. Zhang, L. et al. Intratumoral T cells, recurrence, and survival in epithelial ovarian cancer. *N. Engl. J. Med.* **348**, 203–213 (2003).
17. Vázquez-García, I. et al. Ovarian cancer mutational processes drive site-specific immune evasion. *Nature* **612**, 778–786 (2022).
18. Zhang, A. W. et al. Interfaces of malignant and immunologic clonal dynamics in ovarian cancer. *Cell* **173**, 1755–1769 (2018).
19. Doo, D. W., Norian, L. A. & Arend, R. C. Checkpoint inhibitors in ovarian cancer: a review of preclinical data. *Gynecol. Oncol. Rep.* **29**, 48–54 (2019).
20. Kandalaft, L. E., Dangaj Laniti, D. & Coukos, G. Immunobiology of high-grade serous ovarian cancer: lessons for clinical translation. *Nat. Rev. Cancer* https://doi.org/10.1038/s41568-022-00503-z (2022).
21. He, S. et al. High-plex imaging of RNA and proteins at subcellular resolution in fixed tissue by spatial molecular imaging. *Nat. Biotechnol.* **40**, 1794–1806 (2022).
22. Ke, R. et al. In situ sequencing for RNA analysis in preserved tissue and cells. *Nat. Methods* **10**, 857–860 (2013).
23. Moffitt, J. R. & Zhuang, X. RNA imaging with multiplexed error-robust fluorescence in situ hybridization (MERFISH). *Methods Enzymol.* **572**, 1–49 (2016).
24. Shih, A. J. et al. Identification of grade and origin specific cell populations in serous epithelial ovarian cancer by single cell RNA-seq. *PLoS ONE* https://doi.org/10.1371/journal.pone.0206785 (2018).
25. Olalekan, S., Xie, B., Back, R., Eckart, H. & Basu, A. Characterizing the tumor microenvironment of metastatic ovarian cancer by single-cell transcriptomics. *Cell Rep.* **35**, 109165 (2021).
26. Regner, M. J. et al. A multi-omic single-cell landscape of human gynecologic malignancies. *Mol. Cell* **81**, 4924–4941 (2021).
27. Olbrecht, S. et al. High-grade serous tubo-ovarian cancer refined with single-cell RNA sequencing: specific cell subtypes influence survival and determine molecular subtype classification. *Genome Med.* **13**, 111 (2021).
28. Geistlinger, L. Multiomic analysis of subtype evolution and heterogeneity in high-grade serous ovarian carcinoma. *Cancer Res.* https://doi.org/10.1158/0008-5472.CAN-20-0521 (2020).
29. Qian, J. et al. A pan-cancer blueprint of the heterogeneous tumor microenvironment revealed by single-cell profiling. *Cell Res.* **30**, 745–762 (2020).

30. Zheng, L. et al. Pan-cancer single-cell landscape of tumor-infiltrating T cells. *Science* **374**, abe6474 (2021).
31. Sade-Feldman, M. et al. Defining T cell states associated with response to checkpoint immunotherapy in melanoma. *Cell* **175**, 998–1013 (2018).
32. Wu, V. H. et al. The GPCR–Gαs–PKA signaling axis promotes T cell dysfunction and cancer immunotherapy failure. *Nat. Immunol.* https://doi.org/10.1038/s41590-023-01529-7 (2023).
33. Di Pilato, M. et al. CXCR6 positions cytotoxic T cells to receive critical survival signals in the tumor microenvironment. *Cell* https://doi.org/10.1016/j.cell.2021.07.015 (2021).
34. Tooley, K. et al. Pan-cancer mapping of single CD8$^+$ T cell profiles reveals a TCF1:CXCR6 axis regulating CD28 co-stimulation and anti-tumor immunity. *Cell Rep. Med.* https://doi.org/10.1016/j.xcrm.2024.101640 (2024).
35. Zheng, C. et al. Landscape of infiltrating T cells in liver cancer revealed by single-cell sequencing. *Cell* **169**, 1342–1356 (2017).
36. Casey, L. & Singh, N. Ovarian high-grade serous carcinoma: assessing pathology for site of origin, staging and post-neoadjuvant chemotherapy changes. *Surg. Pathol. Clin.* **12**, 515–528 (2019).
37. Layton, T. B. et al. Cellular census of human fibrosis defines functionally distinct stromal cell types and states. *Nat. Commun.* **11**, 2768 (2020).
38. Plikus, M. V. et al. Fibroblasts: origins, definitions, and functions in health and disease. *Cell* **184**, 3852–3872 (2021).
39. Lendahl, U., Muhl, L. & Betsholtz, C. Identification, discrimination and heterogeneity of fibroblasts. *Nat. Commun.* https://doi.org/10.1038/s41467-022-30633-9 (2022).
40. Buechler, M. B. et al. Cross-tissue organization of the fibroblast lineage. *Nature* https://doi.org/10.1038/s41586-021-03549-5 (2021).
41. Guerrero-Juarez, C. F. et al. Single-cell analysis reveals fibroblast heterogeneity and myeloid-derived adipocyte progenitors in murine skin wounds. *Nat. Commun.* **10**, 650 (2019).
42. Foster, D. S. et al. Integrated spatial multiomics reveals fibroblast fate during tissue repair. *Proc. Natl Acad. Sci. USA* **118**, e2110025118 (2021).
43. Ramilowski, J. A. et al. A draft network of ligand–receptor-mediated multicellular signalling in human. *Nat. Commun.* **6**, 7866 (2015).
44. Efremova, M., Vento-Tormo, M., Teichmann, S. A. & Vento-Tormo, R. CellPhoneDB: inferring cell–cell communication from combined expression of multi-subunit ligand–receptor complexes. *Nat. Protoc.* **15**, 1484–1506 (2020).
45. Browaeys, R., Saelens, W. & Saeys, Y. NicheNet: modeling intercellular communication by linking ligands to target genes. *Nat. Methods* **17**, 159–162 (2020).
46. Zhao, X., Shan, Q. & Xue, H.-H. TCF1 in T cell immunity: a broadened frontier. *Nat. Rev. Immunol.* https://doi.org/10.1038/s41577-021-00563-6 (2021).
47. Hornburg, M. et al. Single-cell dissection of cellular components and interactions shaping the tumor immune phenotypes in ovarian cancer. *Cancer Cell* **39**, 928–944 (2021).
48. Lawson, K. A. et al. Functional genomic landscape of cancer-intrinsic evasion of killing by T cells. *Nature* **586**, 120–126 (2020).
49. Patel, S. J. et al. Identification of essential genes for cancer immunotherapy. *Nature* **548**, 537–542 (2017).
50. Manguso, R. T. et al. In vivo CRISPR screening identifies Ptpn2 as a cancer immunotherapy target. *Nature* **547**, 413–418 (2017).
51. Griffin, G. K. et al. Epigenetic silencing by SETDB1 suppresses tumour intrinsic immunogenicity. *Nature* **595**, 309–314 (2021).
52. Joung, J. et al. CRISPR activation screen identifies BCL-2 proteins and B3GNT2 as drivers of cancer resistance to T cell-mediated cytotoxicity. *Nat. Commun.* **13**, 1606 (2022).
53. Zaretsky, J. M. et al. Mutations associated with acquired resistance to PD-1 blockade in melanoma. *N. Engl. J. Med.* **375**, 819–829 (2016).
54. Hu, N., Zou, L., Wang, C. & Song, G. RUNX1T1 function in cell fate. *Stem Cell Res. Ther.* **13**, 369 (2022).
55. Rossetti, S. & Sacchi, N. RUNX1: a microRNA hub in normal and malignant hematopoiesis. *Int. J. Mol. Sci.* **14**, 1566–1588 (2013).
56. Liu, D. et al. Integrative molecular and clinical modeling of clinical outcomes to PD1 blockade in patients with metastatic melanoma. *Nat. Med.* **25**, 1916–1927 (2019).
57. Ravi, A. et al. Genomic and transcriptomic analysis of checkpoint blockade response in advanced non-small cell lung cancer. *Nat. Genet.* **55**, 807–819 (2023).
58. Pusztai, L. et al. Durvalumab with olaparib and paclitaxel for high-risk HER2-negative stage II/III breast cancer: results from the adaptively randomized I-SPY2 trial. *Cancer Cell* **39**, 989–998 (2021).
59. Wolf, D. M. et al. Redefining breast cancer subtypes to guide treatment prioritization and maximize response: predictive biomarkers across 10 cancer therapies. *Cancer Cell* **40**, 609–623 (2022).
60. Mariathasan, S. et al. TGFβ attenuates tumour response to PD-L1 blockade by contributing to exclusion of T cells. *Nature* **554**, 544–548 (2018).
61. Jhunjhunwala, S., Hammer, C. & Delamarre, L. Antigen presentation in cancer: insights into tumour immunogenicity and immune evasion. *Nat. Rev. Cancer* **21**, 298–312 (2021).
62. Zhang, H. et al. Blocking Wnt/β-catenin signal amplifies anti-PD-1 therapeutic efficacy by inhibiting tumor growth, migration, and promoting immune infiltration in glioblastomas. *Mol. Cancer Ther.* **20**, 1305–1315 (2021).
63. Spranger, S., Bao, R. & Gajewski, T. F. Melanoma-intrinsic β-catenin signalling prevents anti-tumour immunity. *Nature* **523**, 231–235 (2015).
64. Roulois, D. et al. DNA-demethylating agents target colorectal cancer cells by inducing viral mimicry by endogenous transcripts. *Cell* **162**, 961–973 (2015).
65. Norman, T. M. et al. Exploring genetic interaction manifolds constructed from rich single-cell phenotypes. *Science* **365**, 786–793 (2019).
66. Replogle, J. M. et al. Mapping information-rich genotype-phenotype landscapes with genome-scale Perturb-seq. *Cell* **185**, 2559–2575 (2022).
67. Frangieh, C. J. et al. Multimodal pooled Perturb-CITE-seq screens in patient models define mechanisms of cancer immune evasion. *Nat. Genet.* **53**, 332–341 (2021).
68. Sheng, W. et al. LSD1 ablation stimulates anti-tumor immunity and enables checkpoint blockade. *Cell* **174**, 549–563 (2018).
69. Baumgartner, C. K. et al. The PTPN2/PTPN1 inhibitor ABBV-CLS-484 unleashes potent anti-tumour immunity. *Nature* **622**, 850–862 (2023).
70. Ji, Y., Lotfollahi, M., Wolf, F. A. & Theis, F. J. Machine learning for perturbational single-cell omics. *Cell Syst.* **12**, 522–537 (2021).
71. Roohani, Y., Huang, K. & Leskovec, J. Predicting transcriptional outcomes of novel multigene perturbations with GEARS. *Nat. Biotechnol.* **42**, 927–935 (2024).
72. Weber, E. W. et al. Transient rest restores functionality in exhausted CAR-T cells through epigenetic remodeling. *Science* **372**, eaba1786 (2021).
73. Salmeen, A. et al. Redox regulation of protein tyrosine phosphatase 1B involves a sulphenyl-amide intermediate. *Nature* **423**, 769–773 (2003).
74. Myers, M. P. et al. TYK2 and JAK2 are substrates of protein-tyrosine phosphatase 1B. *J. Biol. Chem.* **276**, 47771–47774 (2001).

75. Johnson, T. O., Ermolieff, J. & Jirousek, M. R. Protein tyrosine phosphatase 1B inhibitors for diabetes. *Nat. Rev. Drug Discov.* **1**, 696–709 (2002).
76. Zhang, Z.-Y. Drugging the undruggable: therapeutic potential of targeting protein tyrosine phosphatases. *Acc. Chem. Res.* **50**, 122–129 (2017).
77. Greisman, J. B. et al. Discovery and validation of the binding poses of allosteric fragment hits to protein tyrosine phosphatase 1b: from molecular dynamics simulations to X-ray crystallography. *J. Chem. Inf. Model.* **63**, 2644–2650 (2023).
78. Sharma, B. et al. Recent advance on PTP1B inhibitors and their biomedical applications. *Eur. J. Med. Chem.* **199**, 112376 (2020).
79. Wiede, F. et al. PTP1B is an intracellular checkpoint that limits T-cell and CAR T-cell antitumor immunity. *Cancer Discov.* **12**, 752–773 (2022).
80. Iracheta-Vellve, A. et al. Abstract 606: targeting the immune checkpoint PTPN2 with ABBV-CLS-484 inflames the tumor microenvironment and unleashes potent $CD8^+$ T cell immunity. *Cancer Res.* **82**, 606 (2022).
81. LoRusso, P. M. et al. Abstract CT257: first-in-human phase 1 studies of PTPN2/1 inhibitors ABBV-CLS-484 and ABBV-CLS-579 in locally advanced or metastatic tumors. *Cancer Res.* **83**, CT257 (2023).
82. Li, W. et al. Quality control, modeling, and visualization of CRISPR screens with MAGeCK-VISPR. *Genome Biol.* **16**, 281 (2015).

Methods

Human tumor specimen collection

All ST data other than the Validation 2 dataset were obtained from archival clinical FFPE tumor tissues, retrospectively procured from archival storage under an Institutional Review Board (IRB)-approved protocol (number 44615). In patients with both adnexal and omental tumors available for study, tumor blocks from both sites were selected by an expert gynecologic pathologist (B.E.H.) using histopathologic review of the associated H&E slides. HGSC diagnosis was confirmed in all cases. Tumor content as well as tissue quality and preservation were assessed for inclusion in the study. The Validation 2 dataset was obtained from fresh HGSC tumors that were collected at the time of surgery by Stanford Tissue Procurement Shared Resource facility with the appropriate written informed consent and institutional IRB approval (number 11977). Samples were flash frozen and stored at −80 °C until requested for this study. Samples were embedded in optimal cutting temperature (OCT) compound. Sections were generated using a cryostat and stained with H&E, which were reviewed by an expert gynecologic pathologist (B.E.H.) to confirm the diagnosis, quality and tumor content. Summary statistics of tissue sections, tumors and patients profiled are available in Supplementary Table 1a. Annotations at the patient level and tissue level are provided in Fig. 1b and Supplementary Table 2a,b, respectively.

Primary $CD8^+$ T cells were isolated from de-identified blood samples received from the Stanford Blood Center (IRB number 13942).

Tumor tissue DNA sequencing

HGSC tumor sample selection for next-generation sequencing (NGS) was based on the assessment of overall tumor content by a board-certified expert pathologist (B.E.H). Solid tumor tissue was digested by proteinase K. Total nucleic acid was extracted from FFPE tissue sections using Chemagic 360 sample-specific extraction kits (PerkinElmer). Percentage tumor cellularity as a ratio of tumor to normal nuclei was verified against pathologist-derived assessment, with a minimum requirement of 20% tumor content. Macro-dissection was utilized as required to enrich specimens below the 20% threshold. Specimens that met the 20% threshold of tumor to normal nuclei were selected for DNA sequencing. DNA sequencing was subsequently performed via Tempus Labs according to the xT platform protocol[83]. Additional information about NGS data generation and processing is provided in Supplementary Information Section 1.9.

ST data collection via SMI

The Discovery and Test datasets were generated using the CosMx SMI instrument according to the company's protocols as described here and in greater detail in Supplementary Information Section 1.5. In brief, CosMx Universal Cell Characterization RNA 960-gene panel and the CosMx Human 6K Discovery Panel were used (Supplementary Table 1b), consisting of ISH probes. Each reporter set contains 16 readout rounds with four different fluorophores, creating a 64-bit barcode design with a Hamming distance of 4 (HD4) and a Hamming weight of 4 (HW4) to ensure low error rates. Probe fluorescence was detected at subcellular resolution via the CosMx SMI instrument, and the signal was aggregated to identify the specific RNA molecule measured in each location[21].

SMI tissue preparation and RNA assay were performed as follows. Five-micron tissue sections were cut from FFPE TMA tissue blocks and adhered onto VWR Superfrost Plus Micro Slides (VWR, 48311-703) or Leica BOND Plus slides (Leica Biosystems, S21.2113.A). After sectioning, the tissue sections were air-dried overnight at room temperature. Tissue preparation was performed as described in the CosMx SMI Manual Slide Preparation Manual (MAN-10184-02). Briefly, the tissues underwent deparaffinization, heat-induced epitope retrieval for 15 min at 100 °C, and enzymatic permeabilization with 3 μg ml^{-1} digestion buffer for 30 min at 40 °C. Subsequently, a 0.0005% working concentration of fiducials were applied to the tissue, followed by post-fixation and blocking using NHS-acetate. Finally, an overnight hybridization was performed using the CosMx Universal Cell Characterization 960 plex RNA Panel or the CosMx Human 6K Discovery Panel of probes. The next day, the tissues were subjected to stringent washes to eliminate any unbound probes. The tissues were stained with CosMx Nuclear Stain, CosMx Hs CD298/B2M, CosMx Hs PanCK/CD45 and CosMx Hs CD3 nuclear and segmentation markers before loading onto the instrument. The slide and coverslip constitute the flow cell, which was placed within a fluidic manifold on the SMI instrument for morphological imaging and in situ analyte readout. Analysis run on the instrument was set up using the 60 s FOV pre-bleaching profile and segmentation profile for human tissue.

ST data collection via Xenium

The Validation 1 dataset was generated via 10x Genomics' Xenium platform according to the company's protocols as described here and in greater detail in Supplementary Information Section 1.6. In brief, 10x Genomics' Xenium ISS technology was used with the Xenium Human Breast Panel for multiplexed measurement of 280 genes (Supplementary Table 1b). Xenium hybridization padlock probes were designed to contain two complementary sequences that hybridize to the target RNA[84]. Probes also contain a third sequence encoding for a gene-specific barcode such that once the paired ends of the probe bind to the target RNA and ligate, a circular DNA probe is generated for rolling circle amplification. Five-micron FFPE TMAs were sectioned onto a Xenium slide, deparaffinated, permeabilized and incubated with a Xenium probe for probe hybridization and barcode amplification, as described in detail in Supplementary Information Section 1.6. Following washing and background fluorescence quenching[84], slides were placed into an imaging cassette and loaded on the Xenium Analyzer instrument for morphological imaging and in situ analyte readout.

ST data collection via MERFISH

The Validation 2 dataset was generated via the Vizgen platform according to the company's protocols as described here and in greater detail in Supplementary Information Section 1.7. In brief, a custom 140-gene panel was designed with an additional set of 50 blank negative control barcodes based on the MERFISH design that incorporates combinatorial labeling with an error-robust encoding scheme to mitigate detection errors[85]. Four HGSC fresh-frozen tissue samples were preserved in OCT compound and stored at −80 °C before sectioning. Ten-micron tissue sections were cut from the fresh-frozen OCT tissue blocks and adhered onto MERSCOPE slides (Vizgen, 20400001). After sectioning, the tissue sections were fixed with 4% paraformaldehyde in 1× PBS for 15 min, washed three times with 1× PBS, and incubated overnight at 4 °C in 70% ethanol. As described in detail in Supplementary Information Section 1.7, following tissue sample preparation process samples were loaded onto the MERSCOPE instrument (Vizgen, 10000001) for analyte readout and morphological imaging.

Cell segmentation

Cell segmentation was performed using a deep-learning-based segmentation image processing algorithm, Mesmer[86], from the DeepCell platform on raw TIFF images. The cell segmentation algorithm was chosen after systematic comparisons with the Omnipose[87] algorithm as described in Supplementary Information Section 1.7 (Extended Data Fig. 1a–f). The inputs for whole-cell segmentation for SMI images included immunofluorescence (IF) images of DAPI and CD298/B2M for nuclear and cell membrane detection, respectively. MERFISH whole-cell image segmentation was performed with DAPI and cell membrane stains (Vizgen stain boundary kit, 10400009). Nuclear segmentation was performed for ISS images wherein the input includes DAPI IF stain.

ST data quantification and processing

Preprocessed RNA in situ data include RNA transcripts confidently identified for each gene and their spatial coordinates. Given these data, each RNA transcript was aligned to the cell segmentation outputs described above based on its spatial coordinates. Cell count matrices, C, were generated by counting the number of RNA transcripts detected within the segmentation boundaries of each cell j for each gene i to yield $c_{i,j}$ for entry of C in each ST dataset. Cell counts were converted to transcripts per million (TPM) according to equation (1):

$$\mathrm{TPM}_{i,j} = \left(\frac{c_{i,j}}{\sum_{i=1}^{G} c_{i,j}}\right) \times 10^6 \quad (1)$$

where G is the total number of genes in each ST dataset.

Expression levels were quantified as shown by equation (2):

$$E_{i,j} = \log_2\left(\frac{\mathrm{TPM}_{i,j}}{10} + 1\right) \quad (2)$$

Cells with fewer than 50, 20 and 5 genes detected in the SMI, Xenium and MERFISH data were excluded, as well as cells with exceptionally large volume (>441 μm^2).

Expression of a gene signature or set was computed by considering all the genes in the signature/set, with additional normalizations to filter technical variation, similarly to the procedure reported before[88] with some modifications as described in Supplementary Information Section 2.1. For gene programs, the expression of the upregulated set minus the expression of the downregulated set was computed as the program expression.

The location of each cell was defined based on the location of its centroid. The r-neighborhood of a cell was defined as all the cells that reside at a distance of at most r μm from the cell. Spatial frames were defined by binning the tissue section FOV to squares with a size of 60 μm × 60 μm (that is, 3,600 μm^2), with a median number of 53 cells per frame.

As described in detail in Supplementary Information Section 2.2, the cell-type annotation procedure was applied separately for each of the three spatial datasets via an initial cell-type assignment followed by an iterative subsampling procedure to obtain robust cell-type assignments with confidence levels. Cell-type signatures used for this purpose were derived from previous HGSC scRNA-seq datasets[26,27,29,89].

Co-embedding ST and scRNA-seq datasets

A reference single-cell atlas was generated to examine consistency across spatial and scRNA-seq cohorts and validate cell-type annotations. The atlas includes spatial datasets collected here and six scRNA-seq HGSC cohorts[17,24–29]. Preprocessed gene expression matrices were downloaded from Synapse (syn33521743)[17], the Gene Expression Omnibus (GEO; GSE118828, GSE173682, GSE147082 and GSE154600)[24,26,25,28] and https://lambrechtslab.sites.vib.be/en/data-access/[27,29]. Tumor samples derived from other anatomical sites, other than the adnexa or omentum, were removed to match the scope of this study. All nine datasets were co-embedded with reciprocal principal component analysis using the top 30 PCs fit on each dataset, using the Seurat R package version 5.1.0 implementation[90], and then visualized with two-dimensional UMAP[91]. A detailed description of the co-embedding pipeline is available in Supplementary Information Section 2.3.

Mixed-effects modeling

Mixed-effect models were used to capture codependencies and the hierarchical structure of the data, where covariates at different levels (for example, cell, spatial frame and sample) are sampled from different distributions. The lme4 (version 1.1-35.4)[92] and lmerTest (version 3.1–3) R packages[93] were used to fit the models using the standard restricted maximum-likelihood method, identify the latent variables that maximize the posterior probability and compute P values and sum of squares in type II ANOVA via the Satterthwaite degree of freedom method.

Identifying spatial gene expression programs

Immune infiltration programs (Supplementary Table 4a) were identified by analyzing the Discovery dataset with the LMMs described above using the frame-level abundance of malignant cells as a measure of the infiltration level. To prevent impact of ambient RNA, only genes that had significantly higher expression levels (pairwise one-sided t-test P value < 1×10^{-3}) in respective immune cell types were considered, using pairwise t-tests when comparing the respective immune cell type to all other cell types. CD8 TIP was extended based on scRNA-seq data[17] (Supplementary Table 4b). Analyzing the CD8$^+$ T cells from this scRNA-seq cohort, the top 50 genes that were significantly correlated (BH FDR < 1×10^{-10}, Spearman correlation) with CD8 TIP expression were identified (Supplementary Table 4b). The M_{TIL} program (Supplementary Table 6a) was identified in a similar manner in the Discovery dataset, defining the presence of T/NK cells as a binary covariate at the frame level. P values were corrected for multiple hypotheses testing using the BH test, and topmost genes with FDR < 0.05 were reported.

Mapping ST data to clinical and genetic features

Mixed-effect models were used to compute the association between the expression of each gene in the different cell types and the patient-matched CNA measurements obtained at the bulk tumor level. Of the 626 genes with CNA measurements, 159 were also included in the Discovery dataset (SMI) panel. For each cell type and each of these 159 genes the following model was fit: tpm ~ (1 | patient) + cna + nact + sites, where tpm denotes the expression of the gene in cells from cell type k, cna denotes the copy number of the same gene (CNA in *cis*), 'nact' denotes treatment status and 'sites' denote the anatomical site (Supplementary Fig. 4a). To derive associations of clinical covariates, treatment status, tumor genomics and anatomical site, a similar model was fit (tpm ~ (1 | patients) + age + stage + nact + sites) on all 960 genes in the Discovery dataset (Supplementary Fig. 4a). Here, 'age' denotes age at diagnosis (≤65 or >65 years), and 'stage' denotes disease stage (III or IV). Similarly, to examine the connection between CNAs and M_{TIL} expression, all 626 genes with CNA were tested with an LMM, considering only malignant cells from the samples with genomic profiling, with M_{TIL} expression as the dependent variable.

Spatial ligand–receptor network

A unified list of 2,678 unique ligand–receptor pairs was compiled based on three published ligand–receptor networks[43–45] (Supplementary Table 5c). A CD8$^+$ T cell-centered network (Supplementary Table 5d) was defined as follows. Ligand–receptor pairs are included in the malignant compartment of the network if they consist of a gene upregulated in the CD8 TIP and: (1) a gene upregulated in the TIP of another immune cell type, or (2) a gene upregulated in the M_{TIL} program. Likewise, ligand–receptor pairs are included in the stromal compartment of the network if they consist of a gene downregulated in the CD8 TIP and: (1) a gene downregulated in the TIP of another immune cell type, or (2) a gene that marks fibroblasts in T/NK cell high niches.

Survival analysis of the HGSC spatial cohort

Survival modeling and visualization was performed using the 'survival' (version 3.7-0) and 'survminer' (verion 0.4.9) R package[94,95]. The time-to-event 'overall survival' variable was constructed with the follow-up time (fu_time1; Supplementary Table 2a,b) defined as days between diagnosis and last follow-up, and the patient status (dead or alive) at last follow-up (event; Supplementary Table 2a,b). For all survival analyses of the HGSC spatial cohort, we combined the SMI TMA datasets from both Discovery and Test 1 datasets to sufficiently power

the analyses. Multivariate and univariate Cox proportional hazards regression models were fit with clinical and treatment features, tumor genomic features and spatiomolecular features in adnexal tumors, and *P* values were computed via the Wald statistic test. Kaplan–Meier curves were plotted to visualize the predictability of predefined discretization of M_{TIL} expression and T/NK cell density on patient overall survival, and *P* values were computed via the log-rank test. These analyses as well as additional confounding analyses are described in detail in Supplementary Information Sections 2.7 and 2.6, respectively.

Survival and ICB response predictors

Confounder-controlled Cox proportional hazards regression models were used to quantify the prognostic value of a given marker in predicting ICB PFS in the ICB melanoma[56] and NSCLC[57] cohorts and in predicting overall survival in the International Cancer Genome Consortium (ICGC) Australian Ovarian Cancer Study cohort. In the breast and urothelial ICB cohorts, PFS was not available and thus categorical clinical response annotations were used to examine if the marker was associated with and predictive of response based on student's two-sample *t*-tests and AUROCs. Further details on survival and ICB response predictions and comparison to other ICB response biomarkers are provided in Supplementary Information Section 2.8.

CNA analyses of TCGA data

TCGA data of array-based gene expression (EXP-A) and copy number somatic mutations were downloaded from the ICGC. The TIL levels of each sample were computed as the expression of a T cell signature. Amplifications and deletions were defined as a copy number log-transformed value ('segment_mean') above or below 0.5 and −0.5, respectively. A one-sided *t*-test was performed per M_{TIL} gene to examine if samples with deletion in M_{TIL}-up gene loci or amplifications in M_{TIL}-down gene loci have significantly lower TIL levels compared to samples without the respective amplification/deletion. Amplifications and deletions that were found to show a statistically significant association are reported in Supplementary Table 9a. SVM classifiers were generated to predict if a tumor has high (above median) TIL levels based on the CNA levels of all M_{TIL} genes, using the 'e1071' (version 1.7–14) R package.

Quantifying IFN-γ and TNF secretion

NK-92 cells were treated with increasing concentrations of recombinant human BMP7 (Neuromics, PR27026). After 24 h, the supernatant was collected, centrifuged at 277*g* for 10 min, transferred into a new 1.5 ml tube, and stored at −80 °C. The supernatants collected were diluted at a 1:100 ratio before the IFN-γ ELISA assay. The concentration of IFN-γ and TNF was determined using the ELISA MAX Deluxe Set Human IFN-γ (BioLegend, 430115) and ELISA MAX Deluxe Set Human TNF (BioLegend, 430215) according to the manufacturer's instructions and analyzed on a Varioskan LUX Multimode Plate Reader (Thermo Fisher). A standard curve was fitted using GraphPad Prism's nonlinear regression (curve fit) built-in analysis on a log–log axis. The analyte concentration was calculated based on the fitted line according to the manufacturer's instructions.

Lentivirus production

Lenti-X 293T cells were cultured in cOPTI-MEM (opti-MEM, Gibco, 31985088), 1× GlutaMAX (Gibco, 35050061), 1 mM sodium pyruvate (Corning, 25-000-Cl), 5% FBS (Gibco, A3840302) and 1× non-essential amino acid (Corning, 25-025-CI). At ~90% confluency, cells were incubated with TransIT-Lenti (MirusBio, 6603) transfection mixture at 37 °C with 5% CO_2. The transfection mixture included cOPTI-MEM supplemented with 14 µg of the respective transfer plasmid, 10 µg psPAX2 (Addgene, plasmid number 12260) and 4.33 µg pMD2.G (Addgene, plasmid number 12259). After 6 h of transfection, the medium was replaced with fresh cOPTI-MEM supplemented with 1× ViralBoost (Alstem Bio, VB100) and incubated for an additional 16 h. The supernatant was harvested 24 h and 48 h after transduction. Harvested viral supernatants were pooled and concentrated with Lenti-X Concentrator (Takara Bio, 631232) by centrifugation at 1,500*g* for 45 min. Viral pellets were resuspended in medium at a volume 100 times smaller than the original volume and stored at −80 °C until retrieved for experiments.

CRISPR gene activation in NK-92 cells

Lentivirus for NK-92 transduction was produced as described above with the following vectors: dcas9-vp64-gfp (Addgene, plasmid number 61422), LentiMPH V2 (Addgene, plasmid number 89308) and a guide RNA (gRNA) backbone (Addgene, plasmid number 112925) cloned with non-targeting (5′-GGTCCATGGGTGGAGTTACG-3′) or CXCR6 (5′-GGATCTGAAGGACGGGAGT-3′) protospacer sequences. sgRNA protospacer oligonucleotides were purchased from IDT, annealed, and cloned into gRNA backbone digested with FastDigest BamHI (Thermo Fisher, FD0054). Briefly, NK-92 cells were transduced with dcas9-vp64-gfp at a multiplicity of infection (MOI) < 0.3. The GFP-positive cells were sorted using a Sony Biotechnology SH800S Cell Sorter, transduced with the LentiMPH V2 vector at an MOI < 0.3, and selected with 500 µg ml^{-1} hygromyin. dCas9-MPH NK-92 cells were transduced with sgRNA at an MOI < 0.3 and selected with 1 µg ml^{-1} puromycin. Flow cytometry was used to assess CXCR6 protein expression. NK-92 cells transduced with the NTC or CXCR6 sgRNA and were stained with Human CXCR6 antibody (BioLegend, 35600525; 1:200 dilution) as described in the flow cytometry analysis of TYK-nu cells section. Cells were analyzed using a Sony Biotechnology SH800S Cell Sorter. All data were analyzed using FlowJo version 10.10.0.

Transwell migration assay

NK-92 cells were harvested, washed with serum-free RPMI media (Gibco, 72400-047) and resuspended in 1 ml of RPMI containing 1% FBS (Gibco, A3840102). Cell numbers were determined by Countess 3 Automated Cell Counter (Invitrogen, AMQAX2000) and 2×10^5 cells in 200 µl were placed in each transwell insert (Corning, 3428). Around 600 µl of RPMI containing 1% FBS with various concentrations of recombinant human CXCL16 (PeproTech, 300-55) and untreated control was added to the bottom of a 24-well plate and incubated at 37 °C with 5% CO_2. Four hours after incubation, top inserts were removed and the migrated cells at the bottom were collected and counted via flow cytometry (SH800S Cell Sorter) with cell counting beads (Precision Count Beads; BioLegend, 424902) for precise cell counts.

Perturb-seq meta-analyses and data-driven screen design

Publicly available Perturb-seq datasets[65,66] were used to identify M_{TIL} regulators. For each dataset, counts were converted to TPM values, and two-sided *t*-tests were performed to identify differentially expressed genes for each perturbation in each one of the screens, comparing the cells with the perturbation to those with control sgRNAs. M_{TIL} expression was computed, and a two-sided *t*-test was performed to examine if M_{TIL} expression was significantly higher or lower in the cells with the perturbation compared to the control cells (with control sgRNAs). For perturbations that showed a significant effect on the M_{TIL} expression (BH FDR < 0.05, *t*-test), hypergeometric tests were used to further confirm that the perturbation significantly represses or activates the M_{TIL} genes, having opposite effects on the M_{TIL}-up and M_{TIL}-down gene subsets.

CRISPR KO library of ovarian cancer cells

Guide sequences were selected from the Human CRISPR Knockout Pooled Library (GeCKO v2)[96]. The pooled sgRNA library was purchased from GenScript in a plasmid format utilizing the pLentiGuide-Puro vector. In total, the library includes 232 sgRNAs targeting 74 genes with three guides per gene and ten non-targeting controls (Supplementary Table 10b). Lentiviral stocks were obtained as described in 'Lentivirus

production' by transfecting lentiCas9-Blast and the custom sgRNA lentiviral library into Lenti-X 293T cells (Takara, 632180).

TYK-nu ovarian cancer cell line (JRCB Cell Bank, JCRB0234.0) was used for the CRISPR screens. To obtain stable Cas9 expression in the TYK-nu cell line (TYK-nu^{Cas9}), 100,000 wild-type TYK-nu cells were seeded in a 24-well plate (Corning, 3526) and incubated overnight. Cells were transduced with the lentiCas9-Blast lentivirus at an MOI of 0.2 with 8 μg ml^{-1} of polybrene (MilliporeSigma, TR-1003) and incubated overnight in 37 °C with 5% CO_2. Transduced TYK-nu cells were then washed with DPBS, and selected over 10 days with 10 μg ml^{-1} of blasticidin (Invivogen, ant-bl-05). Successful transduction of Cas9 was validated via western blot (Extended Data Fig. 8a,c) and flow cytometry analyses (Extended Data Fig. 8b,d). The resulting TYK-nu^{Cas9} cells were then transduced at an MOI of 0.15 with the sgRNA lentiviral library and selected over 5 days with 0.5 μg ml^{-1} of puromycin (Invivogen, ant-pr-1).

Knockout efficiency was quantified via pMCB306 plasmid. The plasmid contains puromycin-T2A-EGFP with EF-1 alpha promoter and an EGFP-targeting sgRNA driven by a mU6 promoter. Following cell transduction with the pMCB306 plasmid, loss of GFP fluorescence indicates functional Cas9 activity, as cleavage of GFP by Cas9 results in loss of fluorescence, whereas intact GFP retains fluorescence. TYK-nu^{Cas9} cells were transduced at an MOI of 0.15 with pMCB306 virus and 8 μg ml^{-1} of polybrene and incubated overnight at 37 °C with 5% CO_2. Transduced TYK-nu^{Cas9} cells were washed with DPBS, and selection was conducted over 5 days with 0.5 μg ml^{-1} of puromycin (Invivogen, ant-pr-1). Editing efficiency was validated via flow cytometry (Extended Data Fig. 8b).

Flow cytometry analysis

Flow cytometry analysis was conducted to sort and analyze TYK-nu$^{Cas9,B2M\text{-}KO}$ cells and a TYK-nu^{Cas9} GFP transduced cell line. TYK-nu$^{Cas9,B2M\text{-}KO}$ cells were washed in 1× PBS and stained with Alexa Fluor 700 anti-human B2M antibody (BioLegend, 395708; 1:20 dilution) for 20 min. Additional cells were set aside to use as unstained controls and to adjust gating. The cells were washed twice in PBS with 1.5% FBS after staining and were filtered through a 35-μm cell strainer before analysis on an LSR II instrument. TYK-nu^{Cas9} GFP cells were prepared in the same way without the staining and analyzed on a Sony Biotechnology SH800S Cell Sorter. All plots were generated with FlowJo version 10.8.1.

Cancer CD8$^+$ T cell co-cultures

TYK-nu$^{Cas9,NY\text{-}ESO\text{-}1+}$ cells were generated by transducing TYK-nu^{Cas9} cells to stably express the NY-ESO-1 antigen, as described in detail in Supplementary Information Section 3.1. Primary human CD8$^+$ T cells were isolated from human whole-blood buffy coat and transduced to express a NY-ESO-1 TCR (1G4) construct (generously provided by the laboratory of K. Wucherpfennig[97], DFCI), as described in detail Supplementary Information Section 3.2.

TYK-nu T cell co-cultures were performed in parallel with either NY-ESO-1 TCR$^+$ or wild-type CD8$^+$ T cells from the same donor as a control, as follows. TYK-nu$^{Cas9,NY\text{-}ESO\text{-}1+}$ cells were seeded into a clear-bottom, black-walled 96-well plate and incubated in 100 μl of T cell medium (Supplementary Information Section 3.2) per well overnight. CD8$^+$ T cells were activated with Dynabeads for 72 h. Following magnetic removal of the Dynadeads, T cells were added to the TYK-nu$^{Cas9,NY\text{-}ESO\text{-}1+}$ culture at varying effector-to-target (E:T) ratios to a total volume of 100 μl per well. The cells were co-cultured for 24 to 72 h.

TYK-nu cell viability and IFN-γ levels in the co-culture were measured to validate the cytotoxicity of the edited CD8$^+$ T cells. For ELISA readouts, supernatants were collected from the 96-well plate at the end of each co-culture period, spun down at 400*g* for 5 min and stored at −20 °C in single-use aliquots for subsequent ELISA assays (Extended Data Fig. 7h). The supernatants collected were diluted at a ratio of 1:1,000 before the IFN-γ ELISA assay (BioLegend, 430104). For cell viability readouts, each well was washed twice with 200 μl of DPBS to remove the T cells at the end of each co-culture period. PrestoBlue cell viability dye (Thermo Scientific, A13261) was added to each well and incubated for 30 min before fluorescence plate reader reading (Tecan Infinite, M1000).

Cancer NK cell co-cultures

TYK-nu ovarian cancer cells (JRCB Cell Bank, JCRB0234.0) were cultured in EMEM (American Type Culture Collection, 30-2003) with 10% heat-inactivated FBS (Life Technologies, A3840102). NK-92 cells (American Type Culture Collection, CRL-2407) were cultured in RPMI 1640 Medium, GlutaMAX Supplement, HEPES medium (Gibco, 72400-047) with 10% heat-inactivated FBS (Life Technologies, A3840102), 200 U ml^{-1} recombinant human IL-2 (PeproTech, 200-02), 1 mM non-essential amino acids (Cytiva, SH30238), 1 mM sodium pyruvate (Cytiva, SH3023901) and 1% penicillin–streptomycin 100× solution (Cytiva, SV30010). For co-culture experiments, TYK-nu cells were seeded in a black-walled, clear-bottom 96-well plate (Greiner, 655090) and incubated overnight. NK-92 cells were added in varying E:T ratios, and the cells were incubated for 24 to 72 h (Extended Data Fig. 8e). NK-92 cell line cytotoxicity was validated using PrestoBlue cell viability dye (Thermo Scientific, A13261) following the manufacturer's protocol.

To validate the specificity of NK cell cytotoxicity in the co-culture experiments, a TYK-nu$^{Cas9,B2M\text{-}KO}$ cell line was generated by transducing TYK-nu^{Cas9} cells with B2M sgRNA lentivirus at an MOI of 0.15. Successful transduction was validated via flow cytometry and western blot analyses (Extended Data Fig. 8c,d). All cell lines were routinely tested for mycoplasma using the Promokine PCR Mycoplasma Test Kit I/C (PromoKine, PK-CA91-1024).

CRISPR screen in cancer CD8$^+$ T cell co-culture

TYK-nu$^{Cas9,NY\text{-}ESO\text{-}1+}$ cells were transduced with the 232 sgRNA library at an MOI of 0.15 and selected with 0.5 μg ml^{-1} of puromycin over a period of 5 days. The resulting library cells were seeded in a 75-mm flask and allowed to adhere overnight to maintain >1,000× coverage. NY-ESO-1 TCR$^+$ CD8 T cells were added at a 5-to-1 E:T cell ratio. The TYK-nu library cells were grown in: (1) monoculture, (2) co-culture with wild-type CD8$^+$ T cells and (3) co-culture with NY-ESO-1 TCR$^+$ CD8 T cells. In all three conditions, TYK-nu cells were incubated for 72 h, in either monoculture or co-culture, before being washed twice in 1× DPBS to remove the CD8$^+$ T cells. TYK-nu library cells were snap frozen and stored at −80 °C before genomic DNA extraction and sgRNA amplification. As a second selection, 2 days after recovery, cells were grown under the same conditions again for 72 h and then allowed to recover again before collection and sequencing. All samples were sequenced on a MiSeq Micro V2 in a single-end run.

CRISPR and Perturb-seq screens in cancer NK co-culture

TYK-nu^{Cas9} cells were transduced with the sgRNA library at an MOI of 0.15 and selected with 0.5 μg ml^{-1} puromycin for 5 days. The first screen was performed for sgRNA and Perturb-seq readouts. TYK-nu library cells were seeded in a 75-mm dish (Corning, 353136) and allowed to adhere overnight. NK-92 cells were added at 1:1 and 2.5:1 E:T cell ratios. Perturb-seq readouts[67,98] were obtained from TYK-nu library cells grown for 48 h in monoculture and co-culture with NK-92 cells. After the completed growth timeline, TYK-nu library cells were washed twice with 10 ml 1× DPBS to remove the suspended NK-92 cells. Two replicates from each condition were put into a single-cell suspension according to the 10× 'Single Cell Suspensions from Cultured Cell Lines for Single Cell RNA Sequencing' protocol (10x Genomics, CG00054 Rev B). The libraries were prepared according to the Chromium Next GEM Single Cell 5′ Reagent Kits v2 (Dual Index) with Feature Barcode technology for CRISPR Screening protocol (10x Genomics, CG000510 Rev B). Equimolar amounts of indexed libraries were pooled and sequenced on a NextSeq 2000 P3 in a paired-end run. A subset of replicated TYK-nu library cells was allowed to recover for an additional day until confluency before being snap frozen and stored at −80 °C. Genomic DNA of

the snap-frozen cells was extracted using the Quick-DNA Midiprep Plus Kit (Zymo Research, D4075). sgRNA amplification was performed following a previously published protocol[52]. Equimolar amounts of indexed libraries were pooled and sequenced on a MiSeq Nano V2 in a single-end run.

A second screen was performed for sgRNA sequencing. TYK-nu library cells were seeded in a six-well dish (Cole-Parmer, 0192770) and were allowed to adhere overnight. NK-92 cells were added at 2.5:1, 5:1 and 7.5:1 E:T ratios for 48 h. Library cells were allowed to recover for 3 days before being snap frozen and prepared for genomic DNA extraction as described above. Each experimental condition was performed in triplicates with >1,000× cells per sgRNA, resulting in 6 and 12 sequencing samples from the first and second screen, respectively.

CRISPR screen and Perturb-seq data analyses

Raw fastq files were processed using the cellranger pipeline (10x Genomics Cell Ranger 7.1.0), and counts were converted to TPM values. For each condition (monoculture, 1:1 co-culture, and 2.5:1 co-culture), data were analyzed to remove nonmalignant cells. Seurat R package was used for *k*-nearest neighbor clustering, resulting in a distinct NK cluster in the co-culture conditions, with expression of *CD3E* and *NCAM1*. This cluster was removed, and only cancer cells with a detection of a single sgRNA were retained for downstream analyses. For each of the three conditions, differentially expressed genes were identified for each perturbation using a two-sided *t*-test comparing the cells with the perturbation to those with NTCs. Fisher's test was used to combine the three *P* values. Hypergeometric tests were performed to examine if the upregulated or downregulated genes identified for each perturbation were enriched with M_{TIL}-up or M_{TIL}-down genes, or vice versa, and the combined *P* values (Fisher's test) were reported as the final summary statistics.

MAGeCK algorithm (version 0.5.9.4)[82] was used to compute differential fitness effects in the cancer cells under the monoculture and co-culture conditions, either with the $CD8^+$ T cells or with the NK cells. In brief, the sgRNA counts of the different samples were first median normalized to adjust for the effect of library sizes and read count distributions. Second, the variance of read counts was estimated by sharing information across the different sgRNAs, allowing to fit a negative binomial model to test whether sgRNA abundance differs significantly between treatments (that is, co-culture) and controls (that is, monoculture or co-culture with nonspecific T cells). Third, sgRNAs were ranked based on *P* values calculated from the negative binomial model, and an α-robust ranking aggregation algorithm was used to identify positively or negatively selected genes. The pairwise tests across the different screens were combined with Fisher's statistic *P* values as the summary statistics.

Single-hit CRISPR knockout validation

PTPN1 and *ACTR8* sgRNA sequences were taken from the library used in the CRISPR screen (Supplementary Table 10b). Lentivirus production and transduction of *PTPN1* and *ACTR8* knockouts were generated as described in the lentiviral production section. TYK-$nu^{Cas9,NY\text{-}ESO\text{-}1+}$ cells were transduced at an MOI < 0.5 and selected with puromycin for 5 days. Knockout efficiency was validated with Sanger sequencing using the Synthego ICE analysis tool (Synthego Performance Analysis, ICE Analysis. 2019. V3.0. Synthego (April 2024); Extended Data Fig. 10a,b).

Apoptosis assay

TYK-nu cells (TYK-$nu^{PTPN1KO}$, TYK-$nu^{ACTR8KO}$, TYK-nu^{NTC}) were seeded at a density of 80,000 cells per ml in a 24-well dish and incubated overnight. The next day, TYK-nu cells were pretreated with NucView 488 caspase-3 substrate (Biotium, 10403) at a concentration of 1 µM for 30 min. NK-92 cells or NY-ESO-1 TCR^+ $CD8^+$T cells were added at a 4:1 or 1:1 E:T ratio, respectively. The plates were then placed into a Sartorious Incucyte S3 and imaged every hour for 16 h. Sixteen images were taken per well for each time point using a ×10 objective. Incucyte analysis software was used to compute integrated intensity of green fluorescence signal (global counting units × μm^2/image).

PTPN1/PTPN2 inhibition

Wild-type TYK-nu cells were seeded at a density of 80,000 cells per ml in a 24-well dish and incubated overnight. The next day, NK-92 cells were added at a 2.5:1 E:T ratio and PTPN1/PTPN2 inhibitor ABBV-CLS-484 (MedChemExpress, HY-145923) was added at varying concentrations (4 µM, 8 µM and 16 µM). After a 48-h incubation, NK-92 cells were washed away, and cytotoxicity was measured using the PrestoBlue cell viability dye according to the manufacturer's instructions. The same procedure was conducted in parallel with TYK-nu monoculture. Similarly, wild-type OVCAR3 cells were seeded at a density of 200,000 cells per ml. NK-92 cells were added at a 1.5-to-1 E:T ratio, and ABBV-CLS-484 was added at varying concentrations (0.5 µM, 1 µM, 2 µM, 4 µM, 8 µM and 16 µM). After a 24-h incubation, NK-92 cells were washed away, and cytotoxicity was measured using the PrestoBlue cell viability dye. The same procedure was conducted in parallel with OVCAR3 monoculture.

Reporting summary

Further information on research design is available in the Nature Portfolio Reporting Summary linked to this article.

Data availability

ST data, targeted genomics, de-identified clinical meta data and single-cell Perturb-seq data have been deposited in Zenodo via https://doi.org/10.5281/zenodo.12613839 (ref. 99) and the Single Cell Portal (SCP2640, SCP2641, SCP2650, SCP2644, SCP2646 and SCP2707). Additional data and code to reproduce the figures are provided in the Zenodo repository. Data deposited in the SCP are also available for interactive web visualization. scRNA-seq studies with HGSC tumor samples were accessed from Synapse (syn33521743), the GEO (GSE118828, GSE173682, GSE147082, GSE154600 and GSE146026) and https://lambrechtslab.sites.vib.be/en/data-access/. An additional external validation dataset hosted on the European Genome-Phenome Archive (EGAD00001006973 and EGAD00001006974) was made available for this study through a Data Access Agreement with Genentech. Ovarian cancer 'Sequencing-based Gene Expression' data and accompanying overall survival and clinical annotations of the Australian Ovarian Cancer Study cohort (OV-AU) were downloaded from the ICGC (https://docs.icgc-argo.org/docs/data-access/data-download/). TCGA data of 'array-based gene expression' (EXP-A) and 'copy number somatic mutations' were also downloaded from the ICGC (https://docs.icgc-argo.org/docs/data-access/data-download/). Processed gene expression and clinical data of ICB-treated patients with cancer were downloaded from Supplementary Tables in Liu et al.[56], Zenodo via https://doi.org/10.5281/zenodo.7625516 (ref. 57), http://research-pub.gene.com/IMvigor210CoreBiologies/ and the GEO (GSE173839 and GSE194040). Perturb-seq datasets used for the meta-analysis were downloaded from https://gwps.wi.mit.edu/ and the GEO (GSE133344). Source data are provided with this paper.

Code availability

Code to reproduce results and figures presented in this study is provided as a GitHub repository (https://github.com/Jerby-Lab/HGSC_SpatialPerturbational).

References

83. Beaubier, N. et al. Clinical validation of the tempus xT next-generation targeted oncology sequencing assay. *Oncotarget* **10**, 2384–2396 (2019).
84. Janesick, A. et al. High resolution mapping of the tumor microenvironment using integrated single-cell, spatial and in situ analysis. *Nat. Commun.* **14**, 8353 (2023).

85. Chen, K. H., Boettiger, A. N., Moffitt, J. R., Wang, S. & Zhuang, X. Spatially resolved, highly multiplexed RNA profiling in single cells. *Science* **348**, aaa6090 (2015).
86. Greenwald, N. F. et al. Whole-cell segmentation of tissue images with human-level performance using large-scale data annotation and deep learning. *Nat. Biotechnol.* **40**, 555–565 (2022).
87. Cutler, K. J. et al. Omnipose: a high-precision morphology-independent solution for bacterial cell segmentation. *Nat. Methods* **19**, 1438–1448 (2022).
88. Jerby-Arnon, L. et al. A cancer cell program promotes t cell exclusion and resistance to checkpoint blockade. *Cell* **175**, 984–997 (2018).
89. Izar, B. et al. A single-cell landscape of high-grade serous ovarian cancer. *Nat. Med.* **26**, 1271–1279 (2020).
90. Stuart, T. et al. Comprehensive integration of single-cell data. *Cell* **177**, 1888–1902 (2019).
91. McInnes, L., Healy, J., Saul, N. & Großberger, L. UMAP: uniform manifold approximation and projection. *J. Open Source Softw.* **3**, 861 (2018).
92. Bates, D., Mächler, M., Bolker, B. & Walker, S. Fitting linear mixed-effects models using lme4. *J. Stat. Softw.* **67**, 1–48 (2015).
93. Kuznetsova, A., Brockhoff, P. B. & Christensen, R. H. B. lmerTest package: tests in linear mixed effects models. *J. Stat. Softw.* https://doi.org/10.18637/jss.v082.i13 (2017).
94. Therneau, T. M. survival: survival analysis. R package version 3.5-5; https://CRAN.R-project.org/package=survival (2023).
95. Therneau, T. M. & Grambsch, P. M. *Modeling Survival Data: Extending the Cox Model* (Springer, 2000).
96. Sanjana, N. E., Shalem, O. & Zhang, F. Improved vectors and genome-wide libraries for CRISPR screening. *Nat. Methods* **11**, 783–784 (2014).
97. Mathewson, N. D. et al. Inhibitory CD161 receptor identified in glioma-infiltrating T cells by single-cell analysis. *Cell* **184**, 1281–1298 (2021).
98. Dixit, A. et al. Perturb-seq: dissecting molecular circuits with scalable single-cell RNA profiling of pooled genetic screens. *Cell* **167**, 1853–1866 (2016).
99. Yeh, C. Y. et al. Mapping spatial organization and genetic cell state regulators to target immune evasion in ovarian cancer (version 3). *Zenodo* https://doi.org/10.5281/zenodo.12613839 (2024).

Acknowledgements

We thank R. Villarin Akana, G. Schmitt, G. Allard and K. Spees for help with setting up assays and models related to this work; L. McGuire for help with artwork; K. Wucherpfennig (Dana-Farber Cancer Institute) for generously providing NY-ESO-1 constructs; Stanford Genomics Service Center (SFGF), N. Neff and the rest of the Stanford Chan Zuckerberg Biohub Center team for ongoing support. L.J. is a Chan Zuckerberg Biohub Investigator and an Allen Distinguished Investigator. L.J. holds a Career Award at the Scientific Interface from the Burroughs Wellcome Fund (BWF) and a Liz Tilberis Early Career Award from the Ovarian Cancer Research Alliance (OCRA). This study was supported by the BWF (1019508.01; to L.J.), National Human Genome Research Institute (NHGRI; U01HG012069; to L.J.), OCRA (889076; to L.J), Under One Umbrella, Stanford Women's Cancer Center, Stanford Cancer Institute, a National Cancer Institute (NCI)-designated Comprehensive Cancer Center (251217; to B.E.H. and L.J.) and an NCI Center Support Grant (P30CA124435; to B.E.H.), as well as funds from the Departments of Pathology (to B.E.H.) and Genetics (to L.J.) at Stanford University and from the Chan Zuckerberg Biohub (to L.J.). The content is solely the responsibility of the authors and does not necessarily represent the official views of the NCI.

Author contributions

C.Y.Y., K.A., O.L., B.E.H. and L.J. designed the study. C.Y.Y., K.A., O.L., B.E.H. and L.J. conducted the research and interpreted the results. K.A., O.L., S.K. and Y.-M.K. performed the experiments with L.J. supervision. A.W., B.L., X.Z., L.M.H. and B.E.H. collected, annotated and provided archival tissue samples for profiling. C.Y.Y. and L.J. performed the computational and statistical analyses. R.V., M.C.B. and S.K.P. provided additional support on data interpretation. M.P.S. supported spatial data collection. C.Y.Y., K.A., O.L., B.E.H. and L.J. wrote the paper. B.E.H. and L.J. obtained funding. L.J. supervised the study. All authors reviewed and approved the paper.

Competing interests

M.P.S. is a cofounder and scientific advisor of Personalis, SensOmics, Qbio, January AI, Fodsel, Filtricine, Protos, RTHM, Iollo, Marble Therapeutics and Mirvie. M.P.S. is a scientific advisor of Yuvan, Jupiter, Neuvivo, Swaza and Mitrix. M.C.B has outside interest in DEM Biopharma. The other authors declare no competing interests.

Additional information

Extended data is available for this paper at https://doi.org/10.1038/s41590-024-01943-5.

Supplementary information The online version contains supplementary material available at https://doi.org/10.1038/s41590-024-01943-5.

Correspondence and requests for materials should be addressed to Brooke E. Howitt or Livnat Jerby.

Peer review information *Nature Immunology* thanks Denarda Dangaj Laniti, Jason Moffat and the other, anonymous, reviewer(s) for their contribution to the peer review of this work. Primary Handling Editor: Nick Bernard, in collaboration with the *Nature Immunology* team.

https://doi.org/10.1038/s41590-024-01943-5

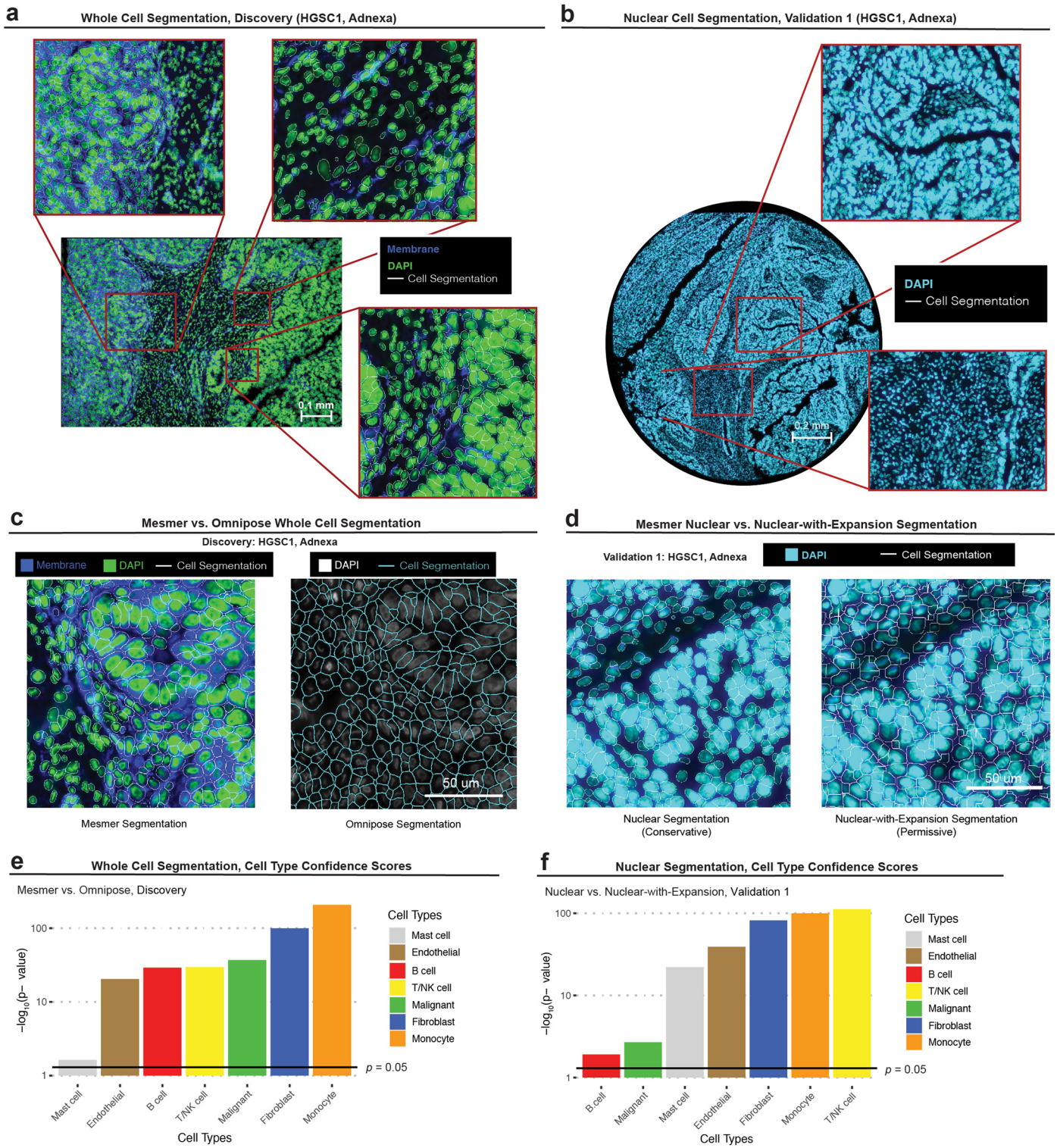

Extended Data Fig. 1 | Cell segmentation. (a) Representative whole-cell segmentation performed for the Discovery dataset. Input data includes DAPI immunofluorescent (IF) and cell membrane stain. Cell boundaries represented as white contours. This is a single representative sample out of 100. Similar results were obtained for all 100 other samples. **(b)** Representative nuclear segmentation performed for Validation 1 dataset. Input data includes DAPI IF stain. Cell boundaries represented as white contours. This is a single representative sample out of 32 samples. Similar results were obtained for all other samples. **(c)** Representative comparison of Mesmer vs. Omnipose cell segmentation in a tissue profile (1 of 100) from the Discovery dataset. **(d)** Representative comparison of Mesmer Nuclear (left) and Mesmer Nuclear-with-Expansion (right) segmentation in a tissue profile (1 of 32) from Validation 1 dataset. **(e)** P values denoting if cell type confidence scores are significantly higher (one-sided Wilcoxon sum rank test) for whole cells segmented by Mesmer vs. Omnipose for each cell type in the Discovery dataset. **(f)** P values denoting if cell type confidence scores are significantly higher (one-sided Wilcoxon sum rank test) in cells segmented by Mesmer Nuclear vs. Mesmer Nuclear-with-Expansion for each cell type in Validation 1 dataset.

https://doi.org/10.1038/s41590-024-01943-5

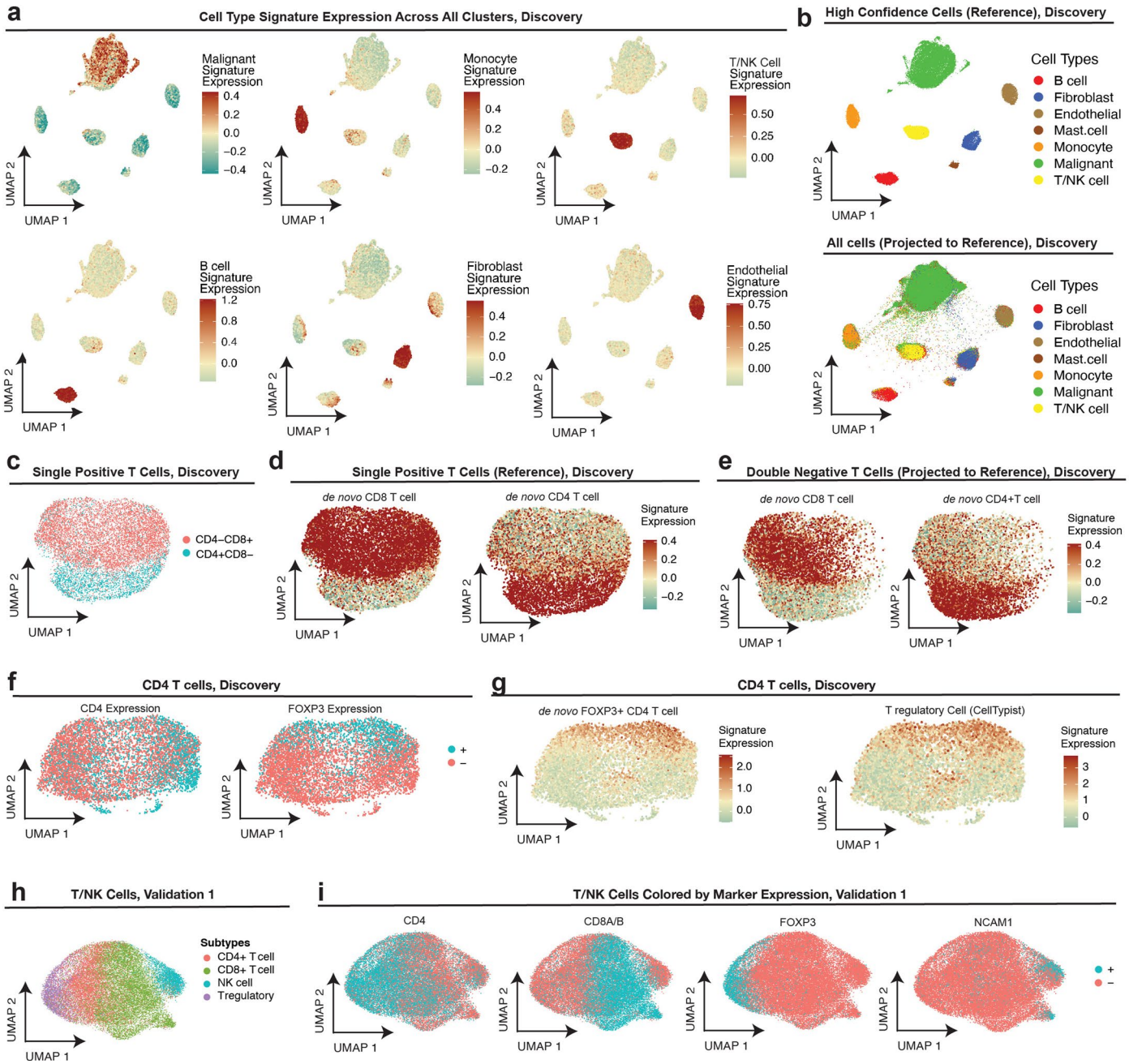

Extended Data Fig. 2 | Cell type annotations of spatial transcriptomics. **(a)** UMAP projection (matches (b) and Fig. 1c) of high confidence (Supplementary Methods) spatial single cell transcriptomes (Discovery dataset); cells colored by overall expression of pre-defined cell type signatures (Supplementary Table 3,a, Methods). **(b)** UMAP projection of high confidence (top panel, matches (a) and Fig. 1c) spatial single cell transcriptomes (Discovery dataset) to yield a reference map. UMAP projection of all cells in the Discovery dataset (bottom panel) onto the high confidence reference map. **(c-d)** UMAP embedding of single positive (that is, $CD4^+$ or $CD8^+$) T cell transcriptomes (Discovery dataset), cells colored by **(c)** CD8 and CD4 expression, and **(d)** expression of *de novo* CD8 (left) and CD4 (right) T cell expression signatures. **(e)** Projection of double negative T/NK cell transcriptomes (Discovery) onto CD8/CD4 T cell reference map in (b), with cells colored by overall expression of the *de novo* CD8 (left) and CD4 (right) T cell gene signatures (Supplementary Table 3,b). **(f)** UMAP embedding of CD4 T cell transcriptomes (Discovery dataset), cells colored by CD4 expression (left) and *FOXP3* expression (right). **(g)** UMAP as in (f), with cells (Discovery dataset) colored based on *de novo* $FOXP3^+CD4$ T cell gene signature expression (left) and pre-defined regulatory T cell (Treg) signature expression (Methods; Supplementary Table 3,a). **(h-i)** UMAP embedding T/NK single cell transcriptomes in Validation 1 dataset, cells colored by **(h)** final T/NK cell subtype annotations, **(i)** detection of (from left to right): *CD4*, *CD8A/B*, *FOXP3* (regulatory T cell marker), and *NCAM1* (NK cell marker).

https://doi.org/10.1038/s41590-024-01943-5

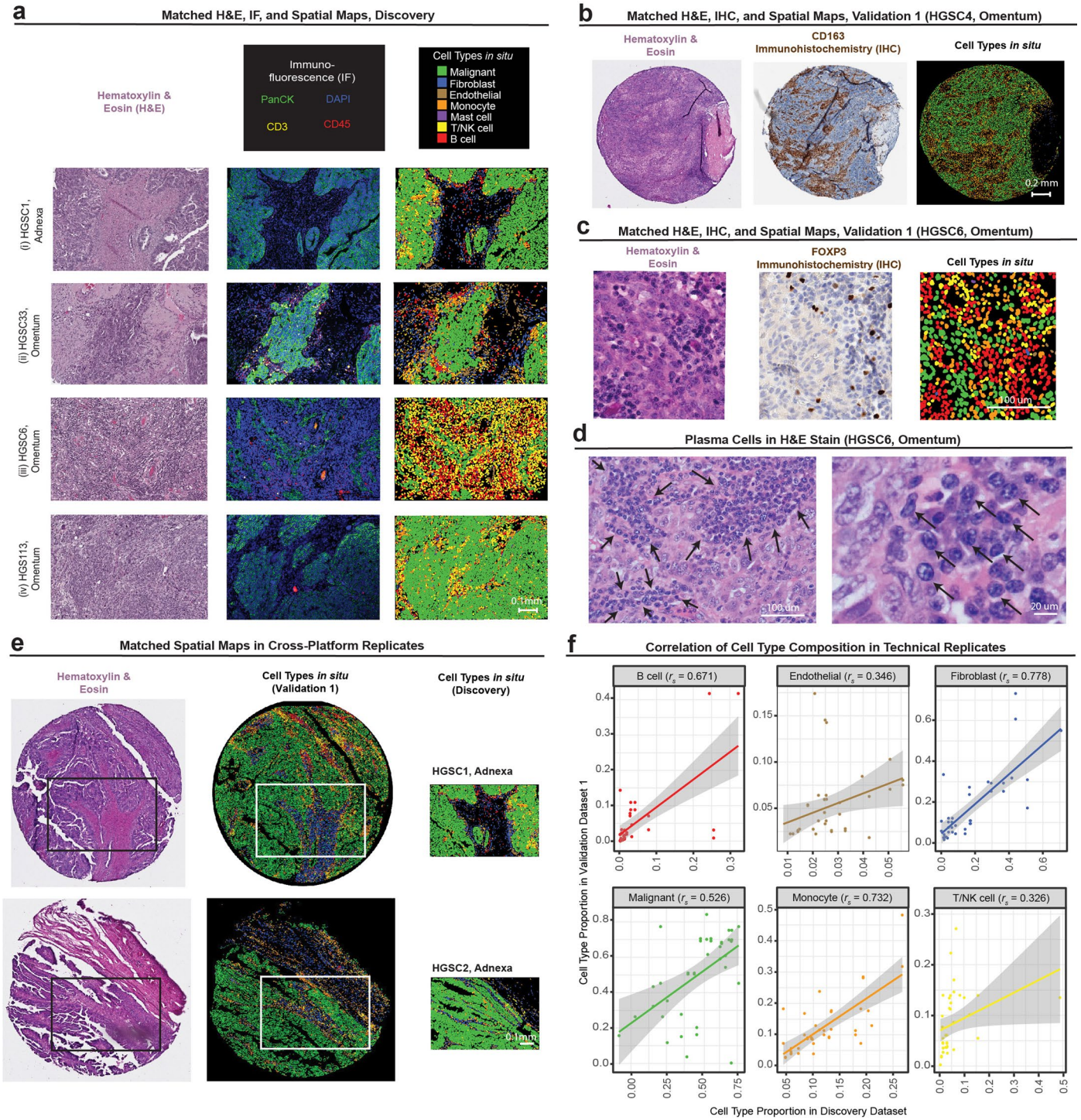

Extended Data Fig. 3 | Cross-platform ST data validations. (a) Hematoxylin & Eosin (H&E) staining (left), Immunofluorescence (middle) of *in situ* cell type annotations in the Discovery dataset (right) for four representative tissue FOV (4 of 100). **(b-c,e-f)** cells colored according to cell type legend in (a). **(b)** H&E staining (left), Immunohistochemistry (IHC) stain for CD163 (middle; monocyte marker) with corresponding *in situ* cell type annotations (right) in a representative tissue core (1 of 32) in Validation 1 dataset. **(c)** H&E (left), IHC stain for FOXP3 (middle, Treg marker), and corresponding *in situ* cell type annotations (right) in a representative tissue (1 of 32) FOV from Validation 1 dataset. **(d)** H&E stains of HGSC6 omentum tumor tissue (1 of 100) resolving morphology of plasma cells (black arrows) identified based on the Discovery tissue profile shown in panel (a)(iii). **(e)** H&E (left), *in situ* cell type annotations from Validation 1 dataset (middle), and Discovery dataset (right) from technical replicate pairs (2 of 39). Each dataset was processed and annotated separately. White box denotes region of tissue profiled by ISS via Xenium in the Validation 1 dataset that corresponds an adjacent region profiled by SMI in the Discovery dataset (same row). **(f)** Cell type proportion in technical replicates profiled both in the Discovery and Validation 1 datasets. Straight lines correspond to the linear regression fit; grey ribbons correspond to 95% confidence interval; r_s denotes the Spearman correlation coefficient.

https://doi.org/10.1038/s41590-024-01943-5

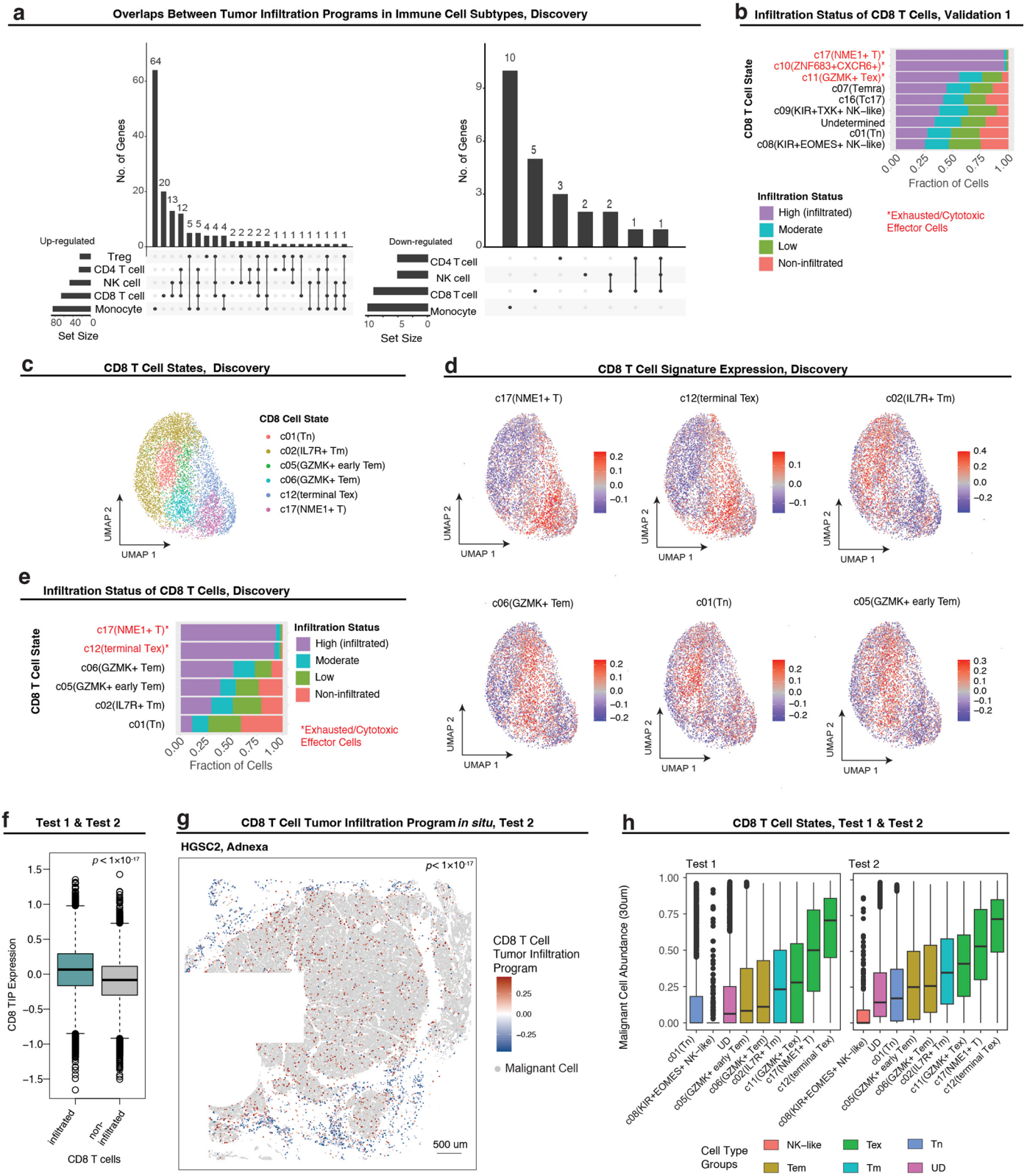

Extended Data Fig. 4 | CD8 T cell states reflect CD8 T cell tumor infiltration levels. (a) Size and overlap between the tumor infiltration programs (TIPs) identified in the Discovery dataset for the five different immune cell subsets, shown for the up-regulated (left) and down-regulated (right) subsets. **(b)** Stratification CD8 T cell subsets based on tumor infiltration status (Validation 1 dataset). **(c-d)** UMAP embedding of CD8 T cells (Discovery dataset) from gene expression only; cells colored by CD8 T cell states[30] (c), overall expression of predefined CD8 T cell signatures[30]. (d). **(e)** Stratification CD8 T cell subsets based on tumor infiltration status (Discovery dataset). **(f)** Expression of CD8 TIP in infiltrating vs. non-infiltrating CD8 T cells (Test 1 and Test 2 datasets); *p*-value derived from one-sided student's *t*-test. **(g)** CD8 TIP expression marks infiltrating CD8 T cells in the Test datasets, shown in situ for a representative whole tissue section (HGSC2, Adnexa, 1 of 4); *p*-value derived from one-sided student's *t*-test. **(h)** Abundance of malignant cells in a 30um radius of CD8 T cells in Test datasets, stratified by CD8 T cell subset.

https://doi.org/10.1038/s41590-024-01943-5

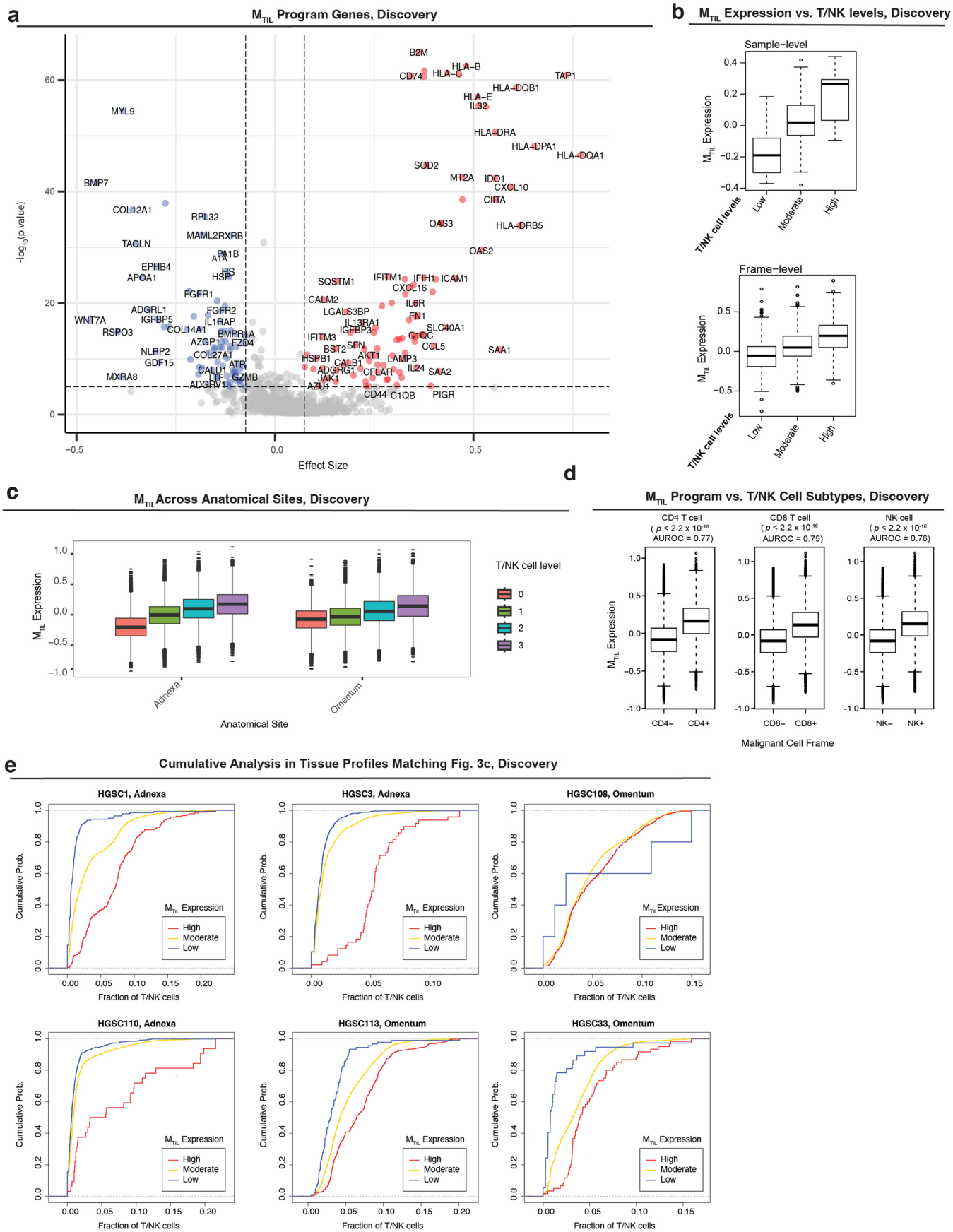

Extended Data Fig. 5 | See next page for caption.

https://doi.org/10.1038/s41590-024-01943-5

Extended Data Fig. 5 | M_{TIL} marks T/NK infiltration at micro- and macro-scales. (a) Statistical significance and effect size showing the association of each gene's expression in malignant cells with T/NK cell levels, quantified via mixed effect models (two-sided) applied to the Discovery dataset (Methods). **(b-d)** In the Discovery dataset: M_{TIL} expression in malignant cells as a function of **(b)** discretized T/NK cell levels across tissue profiles (n = 99 profiles, top) and spatial frames (n = 6699 frames, bottom), **(c)** T/NK cell levels in spatial frames (n = 6699 frames) across anatomical sites, **(d)** presence of T/NK cell subtypes in spatial frames (n = 6699 frames): CD4 T cells (left), CD8 T cells (middle), and NK cells (right); p-values derived from one-sided student's t-test. **(e)** Cumulative probability analysis of fraction of T/NK cells in spatial frames stratified by M_{TIL} expression in 6 representative tissue profiles (Discovery dataset) shown in Fig. 3c. In **(b-d)** Boxplots middle line: median; box edges: 25th and 75th percentiles; whiskers: most extreme points that do not exceed ± IQR x 1.5; further outliers are marked individually with circles (minima/maxima).

https://doi.org/10.1038/s41590-024-01943-5

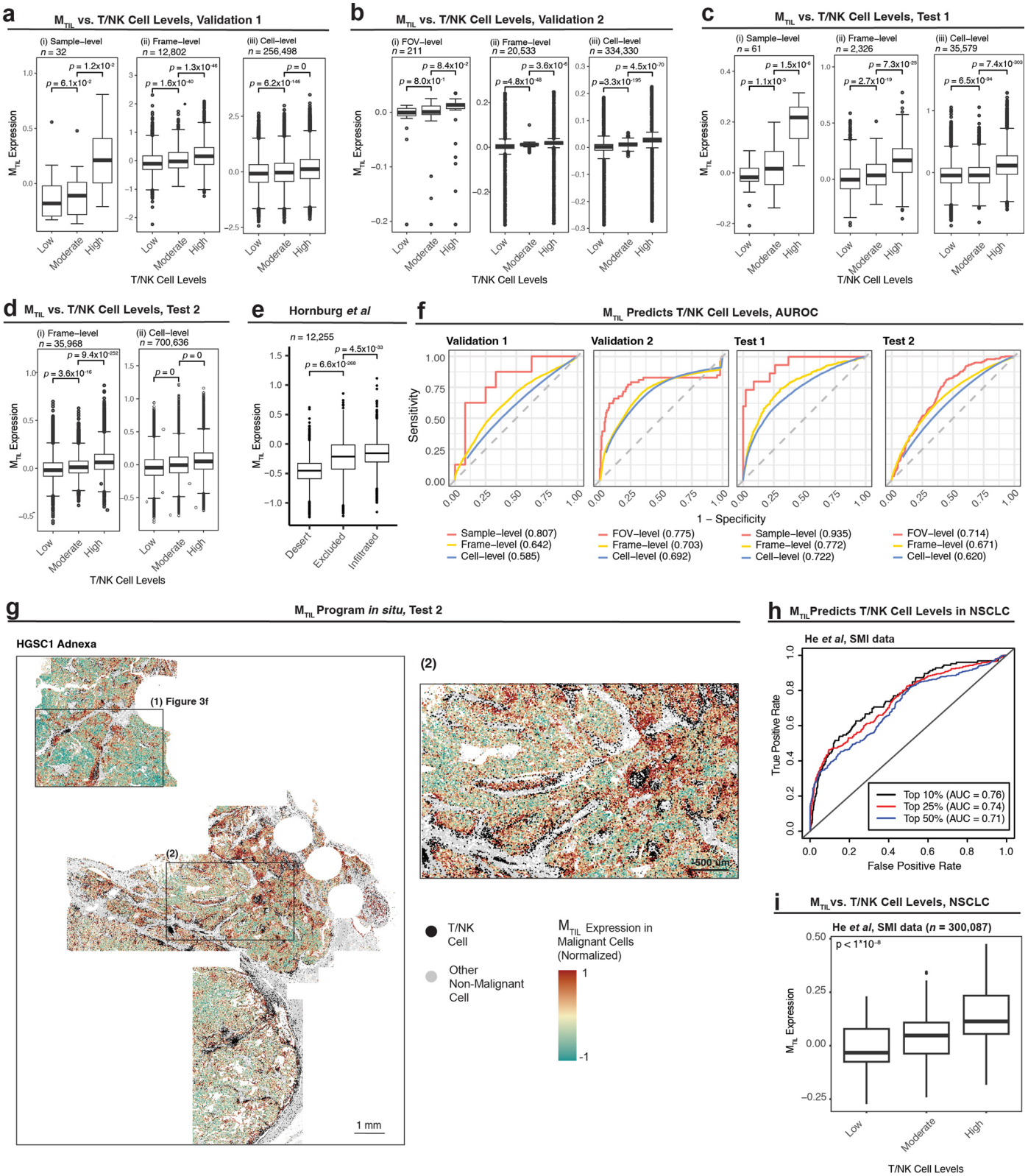

Extended Data Fig. 6 | See next page for caption.

https://doi.org/10.1038/s41590-024-01943-5

Extended Data Fig. 6 | M_{TIL} is predictive of T/NK infiltration. **(a-d)** M_{TIL} expression in malignant cells, stratified by discretized TIL levels in a malignant cell's niche in **(a)** Validation 1 dataset, **(b)** Validation 2 dataset, **(c)** Test 1 dataset, and **(d)** Test 2 dataset. **(e)** M_{TIL} expression in malignant cells, stratified by tissue immune subtyping in Hornburg et al scRNA-seq study[47]. In (a-e) *p*-value derived from one-sided *t*-tests. **(f)** M_{TIL} expression in malignant cells as a predictor of T/NK cell levels. Predictive performances are quantified and visualized via the receiver operating characteristic (ROC) curves shown per ST dataset. Area under the ROC (AUROC) curve is reported in parentheses. **(g)** *In situ* M_{TIL} expression marks T/NK cell levels shown in a representative whole tissue section (HGSC1, Adnexa, Test 2 dataset; M_{TIL} expression is higher in TIL-high versus TIL-low niches, $p = 2.87 \times 10^{-107}$, one-sided Wilcoxon rank sum test). A magnified version of region **(1)** is shown in Fig. 3f, region **(2)** is magnified in the right image. **(h-i)** M_{TIL} predicts T/NK cell levels at the microenvironment level in an independent ST SMI data from NSCLC[21]. **(h)** ROCs depicting prediction performances in NSCLC when predicting the top 10%, 25%, and 50% most T/NK cell rich frames based on the M_{TIL} expression in malignant cells. **(i)** M_{TIL} expression in NSCLC malignant cells stratified by the level of T/NK cells in their vicinity ('high' and 'low' depict the top and bottom quartiles, respectively, and 'moderate' otherwise). *p*-value derived from one-sided mixed effect tests. In **(a-e, i)** boxplots middle line: median; box edges: 25^{th} and 75^{th} percentiles; whiskers: most extreme points that do not exceed ± IQR x 1.5; further outliers are marked individually with circles (minima/maxima).

https://doi.org/10.1038/s41590-024-01943-5

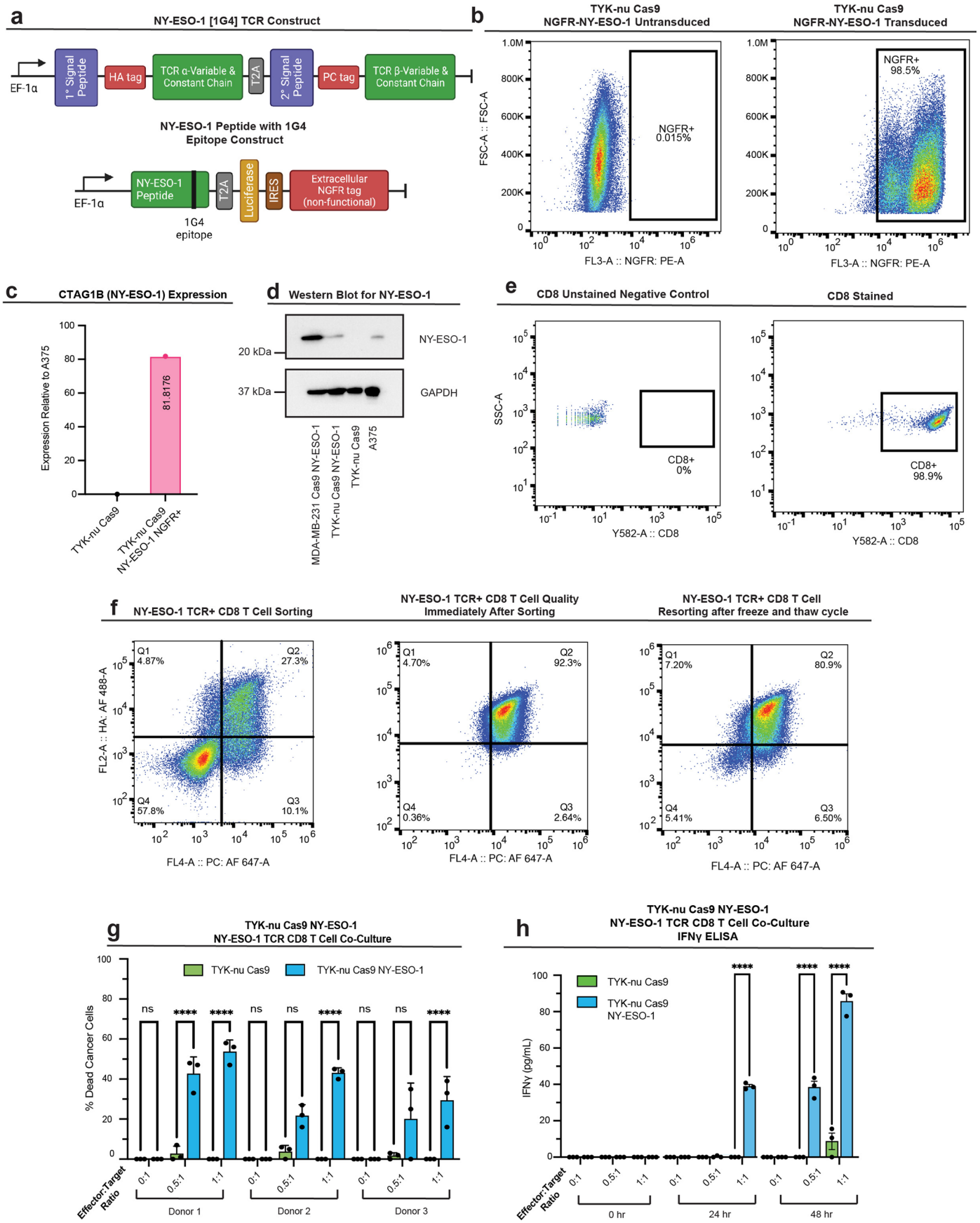

Extended Data Fig. 7 | See next page for caption.

https://doi.org/10.1038/s41590-024-01943-5

Extended Data Fig. 7 | Establishing an ex vivo model of TCR-dependent T cell cytotoxicity. (a) Top: NY-ESO-1 [1G4] TCR lentiviral construct used to engineer primary human CD8 T cells. Bottom: NY-ESO-1 peptide with 1G4 epitope lentiviral construct used to edit TYK-nu Cas9 cells to express the 1G4 NY-ESO-1 antigen. A non-functional, extracellular domain of human growth factor receptor (NGFR) was used to detect and isolate NY-ESO-1 expressing cancer cells. Created with BioRender.com. **(b)** Representative flow cytometric analysis gated on the expression of the non-functional NGFR tag to quantify TYK-nu Cas9 cells transduced to express NY-ESO-1 antigen (TYK-nu$^{Cas9,NY\text{-}ESO\text{-}1+}$). **(c)** qPCR quantification of *CTAG1B* mRNA expression in TYK-nu$^{Cas9,NY\text{-}ESO\text{-}1+}$ cells relative to A375 melanoma cell line with endogenous *CTAG1B* expression. **(d)** Western blot of NY-ESO-1 expression from NY-ESO-1 transduced MDA-MB-231 Cas9, TYK-nu$^{Cas9,NY\text{-}ESO\text{-}1+}$, TYK-nu^{Cas9}, and A375 whole cell lysates. GAPDH was used as a loading control. Data shown in **(d)** is one representative experiment repeated three times with similar results. **(e)** Representative flow cytometric analysis of CD8$^+$ T cells isolated from PBMC. **(f)** Representative flow cytometric analysis of NY-ESO-1 TCR transduced CD8 T cells. HA (α chain) and PC (β chain) double-positive CD8$^+$ T cells were sorted (left). Cells were re-analyzed immediately after sorting to determine sorting quality (middle). Sorted HA$^+$PC$^+$ CD8$^+$ T cells that were frozen and thawed were re-sorted to determine population purity over time (right). **(g)** TCR-dependent cytotoxicity: NY-ESO-1 TCR expressing primary CD8 T cells were co-cultured with TYK-nu^{Cas9} cells or TYK-nu$^{Cas9,NY\text{-}ESO\text{-}1+}$ cells at variable effector to target cell ratios (E:T). The percentage of dead cancer cells was calculated by normalizing to cancer cell monoculture conditions. **(h)** ELISA quantification of IFNγ secreted in the co-culture supernatant (1:1000). In (g) and (h): co-cultures were performed using $n = 3$ technical replicates per condition and $n = 3$ different T cell donors; comparisons are indicated with brackets; p-values $^{****}p < 1 \times 10^{-4}$ (two-way analysis of variance (ANOVA) with multiple comparisons for (g) and (h)); 'ns' denote non-significant ($p > 0.05$) comparisons. Exact p-values and raw blot images are provided with the Source Data. Data shown for (g) represent mean ± standard deviation and (h) mean ± s.e.m.

https://doi.org/10.1038/s41590-024-01943-5

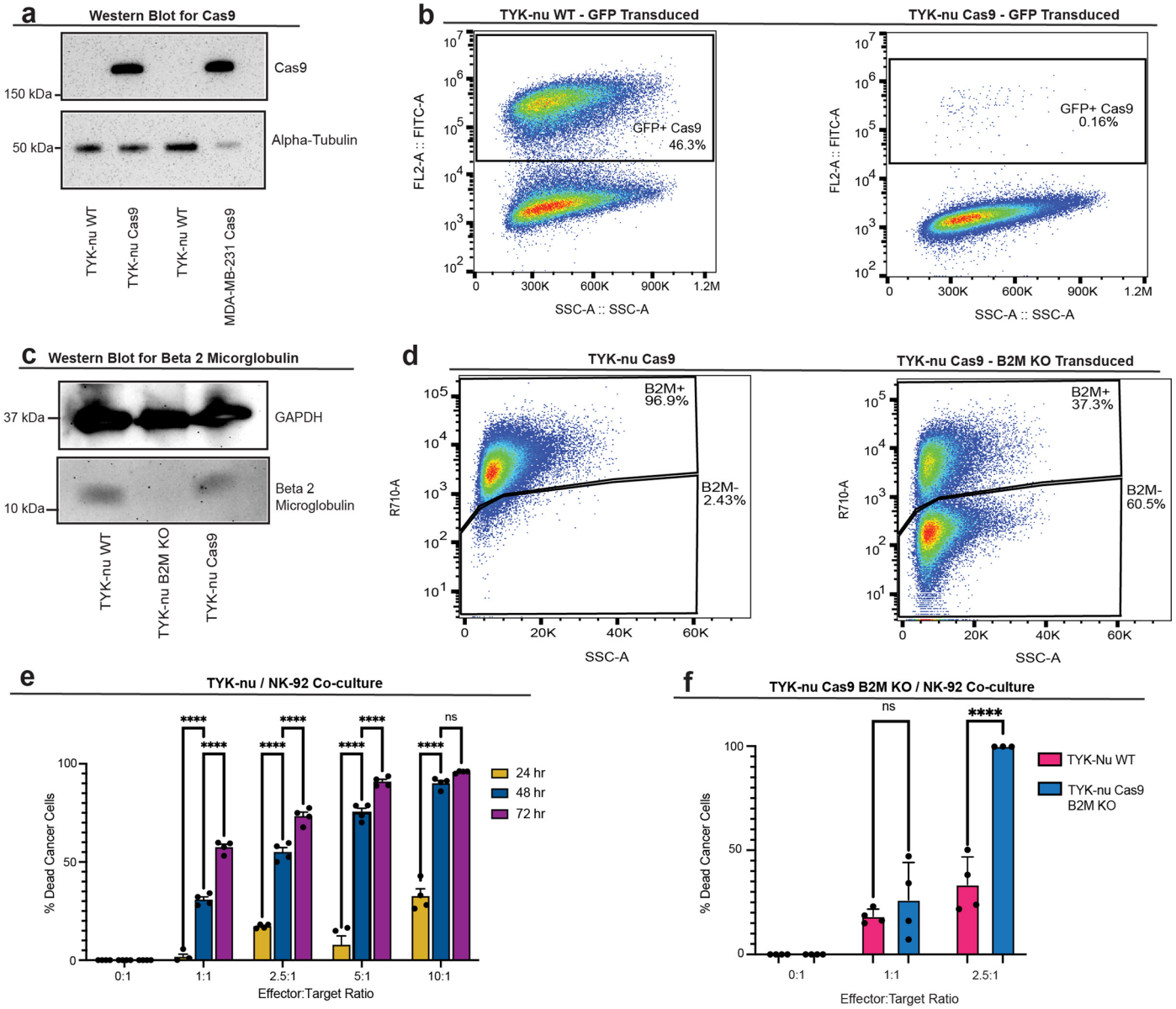

Extended Data Fig. 8 | Establishing an in vitro cancer-NK model for CRISPR screens. (a) Western blot of Cas9 protein from WT and Cas9 transduced whole cell lysates. Alpha tubulin measured as a loading control. **(b)** Representative flow cytometric analysis gated on GFP expression to measure Cas9 efficiency using pMCB306 plasmid. Loss of GFP denotes Cas9 activity (Methods). **(c)** Western blot of beta-2-microglobulin (B2M) from whole cell lysates of WT, Cas9, and $B2M^{KO}$ TYK-nu. GAPDH measured as a loading control. **(d)** B2M surface expression by flow cytometry in $B2M^{wt}$ and $B2M^{KO}$ Cas9 TYK-nu cells. **(e)** 24-to-72-hour time course cell viability in co-cultures of TYK-nu^{Cas9} and NK-92 cells at variable effector to target cell ratios. Percent killing was calculated by normalizing to monoculture conditions. Co-cultures were performed in 4 replicates per condition as shown. **(f)** 48-hour cell viability of $B2M^{KO}$ and $B2M^{WT}$ TYK-nu cell lines in co-culture with NK-92 cells. Percent killing was calculated by normalizing to the respective monoculture conditions. Data shown in **(a)** and **(c)** are one representative experiment repeated two or more times with similar results. In **(e)** and **(f)**, co-culture data is represented by mean ± s.e.m. for (e) and mean ± standard deviation for (f) with each experiment performed in n = 4 technical replicates; *p*-values **** represent $p < 1 \times 10^{-4}$ and * $p < 0.05$ (two-way analysis of variance (ANOVA) with multiple comparisons); 'ns' shown denote non-significant ($p > 0.05$) comparisons. Exact *p*-values and raw blot images are provided with the Source Data. All statistical tests were conducted on GraphPad Prism version 10.2.3.

https://doi.org/10.1038/s41590-024-01943-5

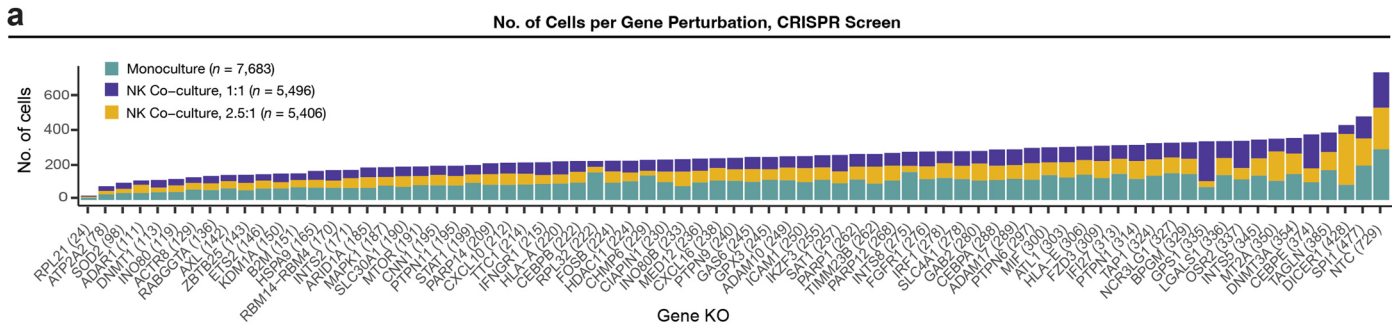

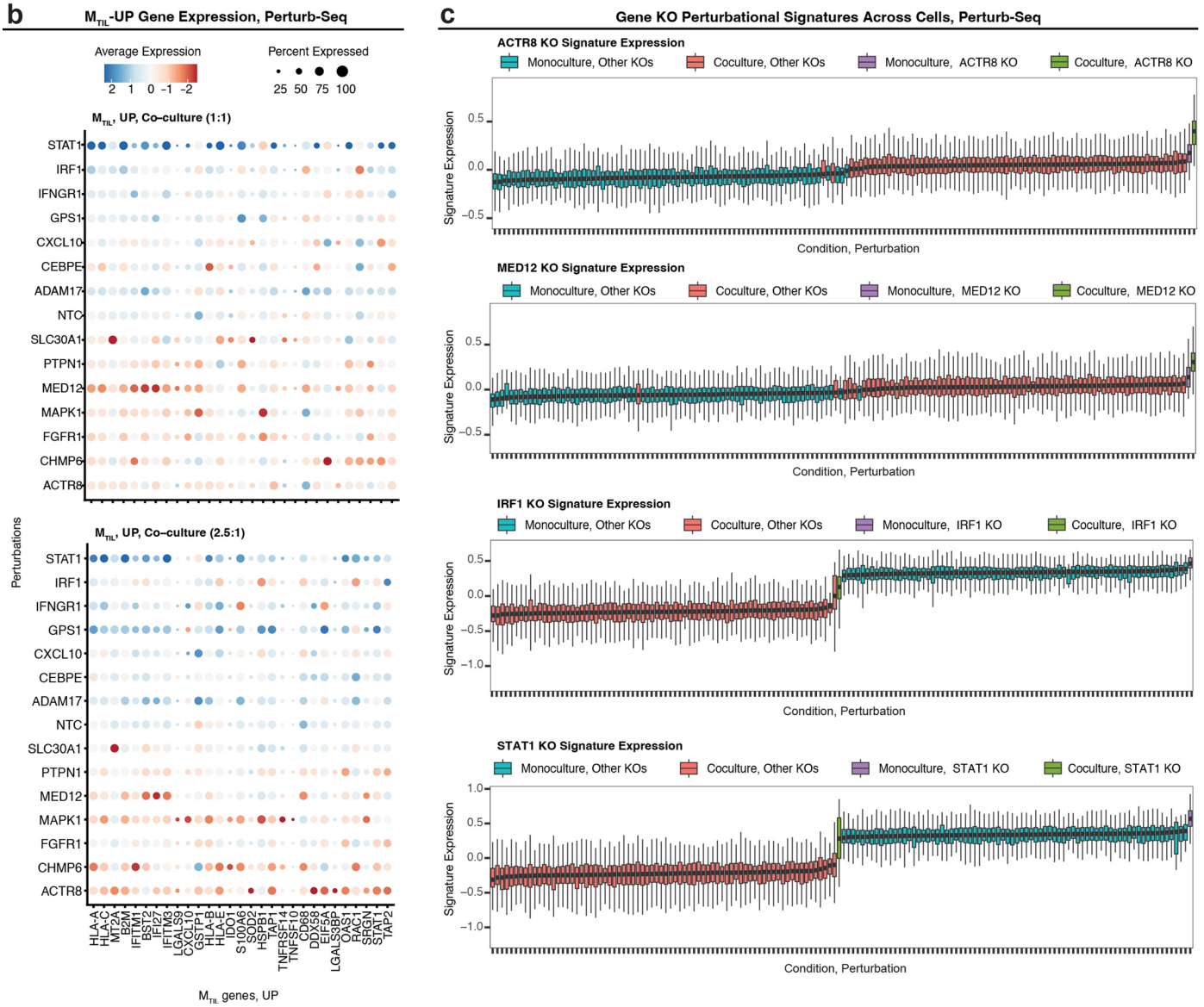

Extended Data Fig. 9 | Perturb-seq screen in ovarian cancer identifies immune response regulators. (a) Number of cells detected with sgRNAs targeting each gene in the CRISPR knockout (KO) library. **(b)** Gene expression of M_{TIL}-up genes under different gene KOs. **(c)** Gene KOs mimic (top and second tows) and repress (third and bottom rows) transcriptional response to NK cells: Expression of KO gene signatures (*ACTR8*, *MED12*, *IRF1*, and *STAT1*) across ovarian cancer cells (n = 18,585 cells in each row) stratified based on culture condition and gene KO combination. Boxplots middle line: median; box edges: 25th and 75th percentiles; whiskers: most extreme points that do not exceed ± IQR x 1.5; minima and maxima are depicted by extreme ends of whiskers.

https://doi.org/10.1038/s41590-024-01943-5

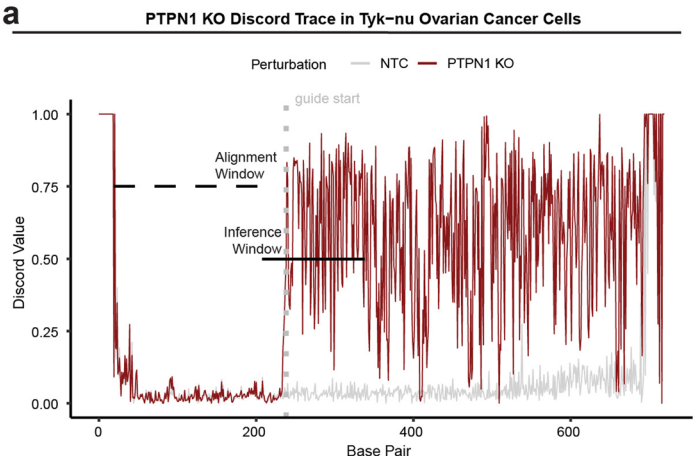

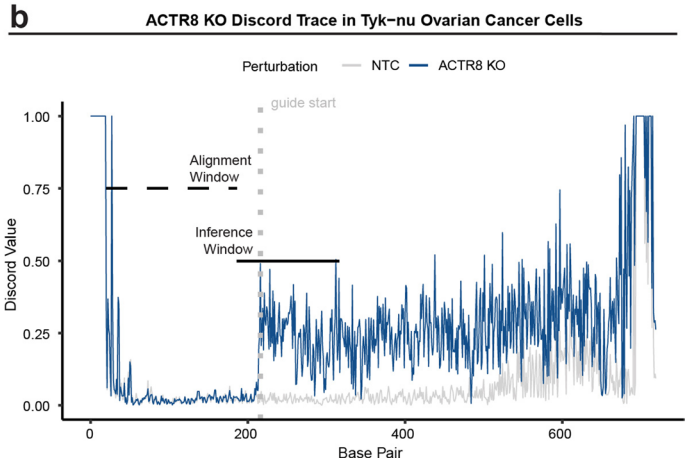

Extended Data Fig. 10 | Validation of *PTPN1* KO and *ACTR8* KO in ovarian cancer cells. (a-b) Discordance of base pairs corresponding to KO target genes **(a)** *PTPN1* and **(b)** *ACTR8* generated from Sanger sequencing using Synthego ICE Analysis tool (v3). Non-targeting control (NTC) depicted in grey. Alignment window for sequences depicted with dashed black bar; interference window for sequences depicted with solid black bar; start of guide sequence is depicted as a grey dotted line.

nature portfolio

Corresponding author(s): Livnat Jerby

Last updated by author(s): 07/01/2024

Reporting Summary

Nature Portfolio wishes to improve the reproducibility of the work that we publish. This form provides structure for consistency and transparency in reporting. For further information on Nature Portfolio policies, see our Editorial Policies and the Editorial Policy Checklist.

Statistics

For all statistical analyses, confirm that the following items are present in the figure legend, table legend, main text, or Methods section.

n/a	Confirmed	
☐	☒	The exact sample size (*n*) for each experimental group/condition, given as a discrete number and unit of measurement
☐	☒	A statement on whether measurements were taken from distinct samples or whether the same sample was measured repeatedly
☐	☒	The statistical test(s) used AND whether they are one- or two-sided *Only common tests should be described solely by name; describe more complex techniques in the Methods section.*
☐	☒	A description of all covariates tested
☐	☒	A description of any assumptions or corrections, such as tests of normality and adjustment for multiple comparisons
☐	☒	A full description of the statistical parameters including central tendency (e.g. means) or other basic estimates (e.g. regression coefficient) AND variation (e.g. standard deviation) or associated estimates of uncertainty (e.g. confidence intervals)
☐	☒	For null hypothesis testing, the test statistic (e.g. *F*, *t*, *r*) with confidence intervals, effect sizes, degrees of freedom and *P* value noted *Give P values as exact values whenever suitable.*
☒	☐	For Bayesian analysis, information on the choice of priors and Markov chain Monte Carlo settings
☐	☒	For hierarchical and complex designs, identification of the appropriate level for tests and full reporting of outcomes
☐	☒	Estimates of effect sizes (e.g. Cohen's *d*, Pearson's *r*), indicating how they were calculated

Our web collection on statistics for biologists contains articles on many of the points above.

Software and code

Policy information about availability of computer code

Data collection	Spatial data collection was preformed via: Xenium Analyzer, Vizgen Inc. platform, and Nanostring CosMx Spatial Molecular Imaging (SMI). Single cell RNA-Seq and Perturb-Seq data were collected via 10x Chromium Controller. Flow cytometry analysis was performed via Sony Biotechnology SH800S Cell Sorter and LSRII instrument (BD Biosciences). Sequencing was performed via MiSeq Micro V2 and NextSeq2000 P3.
Data analysis	The following software, packages, and open-source code were used to analyze the data for the following categories Experimental data visualization • FlowJo (version 10.8.1 and 10.10.0) • FACSDiva software (version 8.0.1) BD BioScience • ImageLab (version 6.1.0) Bio-Rad • QuPath (version 0.4.0) Queen's University, Belfast, Northern Ireland • CFX Manager Software (version 3.1) Bio-Rad Spatial transcriptomics (ST) cell segmentation • Mesmer (https://github.com/vanvalenlab/publication-figures/tree/master/2021-Greenwald_Miller_et_al-Mesmer) • Omnipose (https://github.com/kevinjohncutler/omnipose) Graphing and Plotting • GraphPad PRISM GraphPad Software (version 10.2.3) • ggplot2 (version 3.4.2) • RColorBrewer (version 1.1-3)

• ggpubr (version 0.6.0)
• pheatmap (v1.0.12)
• UpSetR (version 1.4.0)
• heatmap3 (version 1.1.9)
• EnhancedVolcano (version 1.16.0)
• ggrepel (version 0.9.5)
• gplots (version 3.1.3.1)
• ROCR (version 1.0-11)
• cowplot (version 1.1.3)
• beanplot (version 1.3.1)
• patchwork (version 1.2.0)
• forestplot (version 3.1.3)
• Python (version 3.9)
• CoMut (https://github.com/vanallenlab/comut)

Basic data/environment handling and statistical Analysis in R
• R (version 4.3.2)
• lmerTest (version 3.1-3)
• pROC (version 1.18.5)
• tidyr (version 1.3.1)
• ranger (version 0.15.1)
• RStudio (version 2023.12.1)
• argparse (version 2.2.2)
• stringr (version 1.5.1)
• dplyr (version 1.1.4)
• openxlsx (version 4.2.5.2)
• e1071 (version 1.7-14)
• devtools (version 2.4.5)
• usethis (version 2.2.2)
• Matrix (version 1.6-5)
• plotrix (v3.8-4)
• reshape2 (version 1.4.4)
• plyr (version 1.8.9)
• ppcor (version 1.1)
• nnet (version 7.3-19)
• MASS (version 7.3-60)
• mixtools (version 2.0.0)
• rms (version 6.8-1)
• Hmisc (version 5.1-3)
• tibble (version 3.2.1)
• abind (version 1.4-5)
• checkmate (version 2.3.1)
• lme4 (version 1.1-35.4)
• tictoc (version 1.2.1)
• clusterProfiler (version 4.10.1)

High Performance Computing
• Slurm Workload Manager SchedMD https://slurm.schedmd.com/

ST and scRNA-seq Analysis
• 10x Genomics Cell Ranger (version 7.1.0)
• Seurat (version 5.1.0)
• sp (version 2.1-4)
• SeuratObject (version 5.0.2)
• rgeos (version 0.6-4)
• EBImage (version 4.44.0)
• gprofiler2 (version 0.2.2)
• MageCK (version 0.5.9.4; https://github.com/liulab-dfci/MAGeCK)

Survival analysis
• survival (version 3.7-0)
• survminer (version 0.4.9)

Data processing and analysis code is deposited at the GitHub repository (https://github.com/Jerby-Lab/HGSC_SpatialPerturbational), which is now publicly available. The GitHub repository includes documented code for reproducing the main findings in this study.

For manuscripts utilizing custom algorithms or software that are central to the research but not yet described in published literature, software must be made available to editors and reviewers. We strongly encourage code deposition in a community repository (e.g. GitHub). See the Nature Portfolio guidelines for submitting code & software for further information.

Data

Policy information about availability of data

All manuscripts must include a data availability statement. This statement should provide the following information, where applicable:

- Accession codes, unique identifiers, or web links for publicly available datasets
- A description of any restrictions on data availability
- For clinical datasets or third party data, please ensure that the statement adheres to our policy

The data collected in this study, including ST data, targeted genomics, deidentified clinical meta-data, and single-cell Perturb-seq data are publicly accessible through Zenodo (https://doi.org/10.5281/zenodo.12613839), and the Single Cell Portal (SCP2640, SCP2641, SCP2650, SCP2644, SCP2646, SCP2707). Source Data for Figs. 5, 8 and Extended Data Figs. 7, 8 is provided here. Additional data and code to reproduce the figures is provided the Zenodo repository. Data deposited on the Single Cell Portal is also available for interactive web visualization.

Processed gene expression matrices with cell type annotations from 6 scRNA-seq studies with HGSC tumor samples were downloaded from publicly available repositories specified in their respective publications. Specifically, preprocessed gene expression and metadata matrixes of HGSC scRNA-seq data were downloaded from Synapse (syn33521743), GEO (GSE118828, GSE173682, GSE147082, GSE154600, GSE146026), and https://lambrechtslab.sites.vib.be/en/data-access. An additional external validation dataset hosted on the European Genome-Phenome Archive (EGAD00001006973, EGAD00001006974) was made available for this study through a Data Access Agreement with Genentech, Inc.

Ovarian cancer "Sequencing-based Gene Expression" data and accompanying overall survival and clinical annotations of the Australian Ovarian Cancer Study cohort (OV-AU) were downloaded from the ICGC (https://docs.icgc-argo.org/docs/data-access/data-download). The Cancer Genome Atlas (TCGA) data of "Array-based Gene Expression" (EXP-A) and "Copy Number Somatic Mutations" (CNSM) were also downloaded from ICGC (https://docs.icgc-argo.org/docs/data-access/data-download).

Research involving human participants, their data, or biological material

Policy information about studies with human participants or human data. See also policy information about sex, gender (identity/presentation), and sexual orientation and race, ethnicity and racism.

Reporting on sex and gender	The study focuses on high grade serous carcinoma - the most common form of ovarian cancer. The disease occurs only in females and thus the entire study includes only data derived from females patients and cancer cells.
Reporting on race, ethnicity, or other socially relevant groupings	Socially constructed or socially relevant information was not available for this cohort of patients.
Population characteristics	Summary statistics of tissue sections, tumors, and patients profiled are available in Supplementary Table 1a. Annotations at the patient level and tissue level are provided in Fig. 1b and Supplementary Table 2, including patient age, clinical outcomes, sample anatomical site, prior treatments. Samples were allocated as described below.
Recruitment	For the discovery, test 1, test 2 (SMI), and validation 1 (ISS) spatial cohorts, all tumor tissues were archival clinical formalin fixed paraffin embedded (FFPE) tumor tissues, retrospectively procured from archival storage under Institutional Review Board (IRB) approved protocol (#44615). In patients with both adnexal and omental tumors available for study, tumor blocks from both sites were selected by an expert gynecologic pathologist (B.E.H) using histopathologic review of the associated H&E slides. HGSC diagnosis was confirmed in all cases. Tumor content as well as tissue quality and preservation were assessed for inclusion in the study. For the validation 2 (MERFISH) dataset, fresh HGSC tumors were collected at the time of surgery by Stanford Tissue Procurement Shared Resource facility with the appropriate written informed consent and institutional IRB approval (#11977). H&E sections were reviewed by an expert gynecologic pathologist (B.E.H.) to confirm the diagnosis, quality, and tumor content. Primary CD8 T cells were isolated from deidentified blood samples received from the Stanford Blood Center (IRB #13942).
Ethics oversight	The study protocols (#44615 and #11977) were reviewed by Institutional Review Board (IRB) at Stanford University.

Note that full information on the approval of the study protocol must also be provided in the manuscript.

Field-specific reporting

Please select the one below that is the best fit for your research. If you are not sure, read the appropriate sections before making your selection.

☒ Life sciences ☐ Behavioural & social sciences ☐ Ecological, evolutionary & environmental sciences

For a reference copy of the document with all sections, see nature.com/documents/nr-reporting-summary-flat.pdf

Life sciences study design

All studies must disclose on these points even when the disclosure is negative.

Sample size	Single cell spatial transcriptomics data was collected for 94 patients, profiling 130 tumors, generating 202 unique tissue profiles including technical and biological replicates, totaling ~2.6 million cells. The cohort sample size of this study exceeds those reported in previous publications with spatial transcriptomics data. To ensure the sample size was sufficiently large for the analyses and results reported in the manuscript: • Mixed-effect models were used to account for the hierarchical structure of the data and ensure the findings are generalizabile across patients. Only results that were found to be statistically significant ($p < 0.05$) following multiple hypotheses correction were reported. • Out of sample data was used to examine reproducibility within the Discovery dataset. • The data was collected and analyzed in three rounds: 1. Discovery data was used for discovery. 2. Validation data was used to validate the findings from the Discovery data with a different ST technology. 3. Two Test datasets which were collected after the completion of the discovery phase and were used only for testing on unseen patients (Test 1) and on whole tissue sections (Test 2). All experiments were performed in triplicates. CRISPR screens were conducted with an average of >1,000 cells per guide and a Gini index < 0.1 in the baseline cell population. A total of 3 gRNAs were used per knockout to control for different knockout efficiencies and potential off-target effects. All the results reported throughout the study were tested for statistical significance with the appropriate statistical model. In addition to the experiment's sample size, generalizability of key findings was examined by using two ovarian cancer cell lines (TYK-nu and OVCAR3), using both NK-92 and CD8+ T cells, and using different methods for PTPN1 inhibition (i.e., knockout and pharmacological inhibition).
Data exclusions	Single cell gene expression profiles were processed in a fully automated manner via a new pipeline that incorporates multi-sampling to avoid over-fitting and sampling bias. Predefined cutoffs were used to remove data points (i.e., single cell profiles) with low quality, as described in detail in the Method section.
Replication	Spatial transcriptomics data was collected with three different platforms, allowing rigorous cross-platform comparisons. Technical and biological replicates were collected in this study as defined in the Methods. Results from comparisons between biological and technical replicates are described in the study. Cross validation procedures with out-of-sample data were conducted to ensure reproducibility in all spatiomolecular discoveries made in this study. Unseen data from other cohorts, spanning dozens to hundreds of patients were used to confirm the findings generalize to larger unseen patient populations and other data types. All experiments were performed in triplicates. All in vitro cancer cell lines were derived from the same parental cell line and only differ by the sequence of the sgRNA. All NK-92 cells were derived from the same parental cell line. Single cell experiments (i.e., perturb-seq) provide a robust design to ensure reproducibility and directly measure both effect size and variation in the cell population upon perturbations. The findings were reproducible, and all replication attempts are aligned with the results reported.
Randomization	Allocation to experimental groups was random.
Blinding	The spatial data collection was performed without any grouping of patients and thus there was no need to blind authors to group allocation. The follow up high content CRISPR screens were "blind" as the investigators did not control which cells were subject to different perturbation in this pooled setting. Follow up experiments were done so that experimental design (e.g., location on a 96 plate) was predefined prior to observing which cells were randomly allocated to each well. Data analyses were done in a fully automated programmatic manner.

Reporting for specific materials, systems and methods

We require information from authors about some types of materials, experimental systems and methods used in many studies. Here, indicate whether each material, system or method listed is relevant to your study. If you are not sure if a list item applies to your research, read the appropriate section before selecting a response.

Materials & experimental systems

n/a	Involved in the study
☐	☒ Antibodies
☐	☒ Eukaryotic cell lines
☒	☐ Palaeontology and archaeology
☒	☐ Animals and other organisms
☒	☐ Clinical data
☒	☐ Dual use research of concern
☒	☐ Plants

Methods

n/a	Involved in the study
☒	☐ ChIP-seq
☐	☒ Flow cytometry
☒	☐ MRI-based neuroimaging

Antibodies

Antibodies used

The following antibodies were used:
• CD163 (MRQ-26) (Ventana/Cell Marque Cat#163M-1)
• Recombinant anti-FOXP3 (263A/E7) (Abcam Cat#ab96048)
• Cell Boundary Staining Mix (Vizgen Cat#20300010)
• Beta 2 microglobulin (BBM.1) HRP (Santa Cruz Biotechnology, Cat# sc13565 HRP, Lot #L2619)
• Cas9 (S. pyogenes) (7A9-3A3) Mouse mAb (Cell Signaling Technology, Cat#14697S, Lot 6)
• Alpha tubulin Antibody (Cell Signaling Technology, Cat#2144S, Lot 7)
• GAPDH (14C10) Rabbit mAb (Cell Signaling Technology, Cat#2118S, Lot 14)
• Anti-rabbit IgG, HRP-linked Antibody (Cell Signaling Technology, Cat#7074S, Lot 30)
• Anti-mouse IgG HRP-linked Antibody (Cell Signaling Technology, Cat#7076S, Lot 36)
• Alexa Fluor 700 anti-human Beta 2 microglobulin Antibody (BioLegend, Cat#395708, Lot B324548)
• CD8 Antibody, anti-human (PE conjugate) (Miltenyi Biotec, #130-113-158)
• HPC4-tag Antibody (Cell Signaling Technology, Cat#68083S, Lot 1)
• HA-tag (6E2) Mouse Ab (Cell Signaling Technology, Cat#2367S, Lot 5)
• Anti-rabbit IgG (H+L), F(ab')2 fragment (Alexa Fluor 647 conjugate) (Cell Signaling Technology, Cat#4414S, Lot 24)
• Anti-mouse IgG (H+L), F(ab')2 fragment (Alexa Fluor 488 conjugate) (Cell Signaling Technology, Cat#4408S, Lot 22)
• PE anti-human CD271 (NGFR) (ME20.4) (BioLegend, Cat#345106, Lot B360532)
• NY-ESO-1 Antibody (E978) (Santa Cruz Biotechnology, Cat#sc-53869, Lot H0621)
• APC anti-human CD186 (CXCR6) Antibody (BioLegend, Cat# 356006, Lot #B363191)

Validation

All antibodies were validated by the manufacturer and no additional in house validation was performed. Please see the links for additional validation information:

• CD163 (MRQ-26) (Ventana/Cell Marque Cat#163M-1) https://www.cellmarque.com/antibodies/CM/2010/CD163_MRQ-26
• Recombinant anti-FOXP3 (263A/E7) (Abcam Cat#ab96048) https://www.abcam.com/products/primary-antibodies/foxp3-antibody-236ae7-bsa-and-azide-free-ab96048.html
• Cell Boundary Staining Mix (Vizgen Cat#20300010)
• Beta 2 microglobulin (BBM.1) HRP (Santa Cruz Biotechnology, Cat# sc13565, Lot #L2619) https://www.scbt.com/p/beta-2-microglobulin-antibody-bbm-1
• Cas9 (S. pyogenes) (7A9-3A3) Mouse mAb (Cell Signaling Technology, Cat#14697S, Lot 6) https://www.cellsignal.com/products/primary-antibodies/cas9-s-pyogenes-7a9-3a3-mouse-mab/14697
• Alpha tubulin Antibody (Cell Signaling Technology, Cat#2144S, Lot 7) https://www.cellsignal.com/products/primary-antibodies/a-tubulin-antibody/2144
• GAPDH (14C10) Rabbit mAb (Cell Signaling Technology, Cat#2118S, Lot 14) https://www.cellsignal.com/products/primary-antibodies/gapdh-14c10-rabbit-mab/2118
• Anti-rabbit IgG, HRP-linked Antibody (Cell Signaling Technology, Cat#7074S, Lot 30) https://www.cellsignal.com/products/secondary-antibodies/anti-rabbit-igg-hrp-linked-antibody/7074
• Anti-mouse IgG HRP-linked Antibody (Cell Signaling Technology, Cat#7076S, Lot 36) https://www.cellsignal.com/products/secondary-antibodies/anti-rabbit-igg-hrp-linked-antibody/7074
• Alexa Fluor 700 anti-human Beta 2 microglobulin Antibody (BioLegend, Cat#395708, Lot B324548) https://www.biolegend.com/en-us/products/alexa-fluor-700-anti-human-beta2-microglobulin-antibody-17247
• CD8 Antibody, anti-human (PE conjugate) (Miltenyi Biotec, #130-113-158) https://www.miltenyibiotec.com/US-en/products/cd8-antibody-anti-human-bw135-80.html#conjugate=pe:size=100-tests-in-200-ul
• HPC4-Tag Antibody (Cell Signaling Technology, Cat#68083S, Lot 1) https://www.cellsignal.com/products/primary-antibodies/hpc4-tag-antibody/68083
• HA-tag (6E2) Mouse mAb (Cell Signaling Technology, Cat#2367S, Lot 5) https://www.cellsignal.com/products/primary-antibodies/ha-tag-6e2-mouse-mab/2367
• Anti-rabbit IgG (H+L), F(ab')2 fragment (Alexa Fluor 647 conjugate) (Cell Signaling Technology, Cat#4414S, Lot 24) https://www.cellsignal.com/products/secondary-antibodies/anti-rabbit-igg-h-l-f-ab-2-fragment-alexa-fluor-647-conjugate/4414
• Anti-mouse IgG (H+L), F(ab')2 fragment (Alexa Fluor 488 conjugate) (Cell Signaling Technology, Cat#4408S, Lot 22) https://www.cellsignal.com/products/secondary-antibodies/anti-mouse-igg-h-l-f-ab-2-fragment-alexa-fluor-488-conjugate/4408
• PE anti-human CD271 (NGFR) (ME20.4) (BioLegend, Cat#345106, Lot B360532) https://www.biolegend.com/en-us/products/pe-anti-human-cd271-ngfr-antibody-6428
• NY-ESO-1 Antibody (E978) (Santa Cruz Biotechnology, Cat#sc-53869, Lot H0621) https://www.scbt.com/p/ny-eso-1-antibody-e978
• APC anti-human CD186 (CXCR6) Antibody (BioLegend, Cat# 356006, Lot #B363191) https://www.biolegend.com/en-us/products/apc-anti-human-cd186-cxcr6-antibody-8622

Eukaryotic cell lines

Policy information about cell lines and Sex and Gender in Research

Cell line source(s)

The cell lines used in this study are: TYK-nu (JCRB Cell Bank Cat#JCRB0234.0), NK-92 (ATCC, CRL-2407), LentiX 293T (Takara Bio, 632180), OVCAR3 (ATCC, HTB-161), A375 (ATCC, CRL-1619), and MDA-MB-231 Cas9 (GeneCopoeia, SL515) . In addition, primary CD8+ T cells were derived from PBMCs and confirmed via flow cytometry and cytotoxicity co-culture assays to be functional CD8+ T cells.

Authentication

All cell lines were authenticated using ATCC's Human Cell Authentication Service utilizing short tandem repeat (STR) profiling.

Mycoplasma contamination

All cell lines were confirmed negative for mycoplasma by PCR throughout the duration of this study.

Commonly misidentified lines (See ICLAC register)	No commonly misidentified cell lines were used.

Plants

Seed stocks	NA
Novel plant genotypes	NA
Authentication	NA

Flow Cytometry

Plots

Confirm that:

☒ The axis labels state the marker and fluorochrome used (e.g. CD4-FITC).

☒ The axis scales are clearly visible. Include numbers along axes only for bottom left plot of group (a 'group' is an analysis of identical markers).

☒ All plots are contour plots with outliers or pseudocolor plots.

☒ A numerical value for number of cells or percentage (with statistics) is provided.

Methodology

Sample preparation	For sorting using a single antibody, cells were collected and made into a single cell suspension, washed with DPBS, and stained with the primary anti-human antibody for 20 minutes on ice. The cells were then washed twice with DPBS and 1.5% FBS, filtered through a 35uM strainer, and analyzed. When sorting the TYK-nu Cas9 GFP transduced cells, the cells were collected, washed twice with DPBS and 1.5% FBS, and filtered using a 35uM strainer before being analyzed. When staining for multiple antibodies, the cells were collected and made into a single cell suspension, washed with DPBS, incubated with primary antibodies on ice for 1 hour. The cells were then washed by centrifugation, incubated with a secondary antibody for 30 minutes on ice, washed with DPBS and 1.5% FBS, filtered using a 35uM strainer, and analyzed.
Instrument	Flow cytometry for the B2M analysis was performed using the LSRII instrument (BD Biosciences). Flow cytometry for CD8 analysis was performed using the FACSAria II (BD Biosciences). All other flow cytometry analyses were performed using the Sony Biotechnology SH800S cell sorter.
Software	BD FACSDiva was used to perform flow cytometry when using the LSRII and FACSAria II instruments. All analyses were conducted using FlowJo.
Cell population abundance	Representative plots showing the abundance of the different cell populations are provided in Extended Data Figs. 7b,e,f, 8b,d. Flow cytometry was used to quantify cell populations and to validate in vitro and ex vivo experimental models. Cell sorting was performed to sort out TCR specific T cells, as shown in Extended Data Fig. 7f.
Gating strategy	For all experiments, cells were initially gated by FSC/SSC to exclude debris and were further gated to isolate singlets. For single antibody staining, cell populations were further gated based on their cell surface marker. NY-ESO-1 TCR+ CD8 T Cells were initially gated based on FSC/SSC to exclude debris and further gated to isolate singlets. NY-ESO-1 TCR+ CD8 T cells were then further gated as double positive for HA (α chain) and PC (β chain) to ensure complete expression of NY-ESO-1 TCR.

☒ Tick this box to confirm that a figure exemplifying the gating strategy is provided in the Supplementary Information.